

INFLOW PROFILING AND PRODUCTION OPTIMIZATION IN
SMART WELLS USING DISTRIBUTED ACOUSTIC AND
TEMPERATURE MEASUREMENTS

A DISSERTATION
SUBMITTED TO THE DEPARTMENT OF
ENERGY RESOURCES ENGINEERING
AND THE COMMITTEE ON GRADUATE STUDIES
OF STANFORD UNIVERSITY
IN PARTIAL FULFILLMENT OF THE REQUIREMENTS
FOR THE DEGREE OF
DOCTOR OF PHILOSOPHY

Ahmed Yasin Abukhamsin

June 2017

© Copyright by Ahmed Yasin Abukhamsin 2017
All Rights Reserved

I certify that I have read this dissertation and that, in my opinion, it is fully adequate in scope and quality as a dissertation for the degree of Doctor of Philosophy.

(Roland Horne) Principal Adviser

I certify that I have read this dissertation and that, in my opinion, it is fully adequate in scope and quality as a dissertation for the degree of Doctor of Philosophy.

(Khalid Aziz)

I certify that I have read this dissertation and that, in my opinion, it is fully adequate in scope and quality as a dissertation for the degree of Doctor of Philosophy.

(Tapan Mukerji)

Approved for the Stanford University Committee on Graduate Studies

Abstract

Current advances in the well completion technology have allowed for more complex smart well instrumentation with marginal additional cost. As an example, optical fibers can be run along horizontal wells to provide acoustic and temperature data that are distributed both in time and space. With such data at our disposal, an immediate evaluation of the well response is possible as changes occur in reservoir or well conditions. The combination of this continuous monitoring capability and down-hole controls in smart wells, facilitates the implementation of efficient well production optimization. Most current work in distributed measurements looks at Distributed Acoustic Sensing (DAS) or Distributed Temperature Sensing (DTS) data individually, which limits inferences about the multiphase flow problem. The objective of this work was to look at the two sets of data together in the multiphase inflow profiling problem. By doing so, we examined what improvements could be achieved and what limitations persist compared to the conventional methods of looking at each inflow profiling method alone. The last research component focused on integrating several optimization procedures that take advantage of such smart completions.

The study began by evaluating the performance of DAS in analyzing two-phase flow. This process begins by extracting the speed of sound within the fluid medium from the acoustic signal. Then, the phase fraction combination that corresponds to this speed of sound reading can be estimated. Another procedure was used to obtain similar results from DTS measurements. In this case, the in-situ phase fractions are correlated to the Joule-Thomson effect as reservoir fluids enter the wellbore. As both these procedures are limited to one- and two-phase flow applications, the theoretical

background for solutions in three-phase flow problems was established by combining information from DAS and DTS.

The flow profiling procedure was applied to several smart well production data sets that included real wells as well as synthetic models. For real single-phase flow examples, flow rates from different segments of the well were calculated and results were in close agreement with a surface flow meter for most sections of the well. For oil-water production examples, we were able to estimate the phase fractions along the well. However, accuracy of DAS results was dependent on the flow regime in the wellbore. In cases where both DAS and DTS were not available for the same well, a commercial compositional and thermal reservoir simulator was used to generate synthetic data for analysis. By applying the developed procedure, we found that cointerpretation of DAS and DTS data improves the profiling performance in two-phase flow and yields fair accuracy for in-situ three-phase fractions for all ranges of water cuts and gas volume fractions. In comparison, analyzing DAS or DTS individually is usually not sufficient to fully determine a three-phase flow problem.

When the developed optimization procedure was applied for synthetic models completed with a typical smart well design, results showed that significant value could be realized by incorporating downhole flow rate measurements. For example, continuous downhole flow monitoring provides asset managers with more accurate allocation of their wells. Moreover, more accurate history matching of reservoir models is possible by using in-situ phase flows to calibrate existing models. With more accurate models, evaluating different flow scenarios is possible before applying them in the field. Finally, quick decisions to change the controls of the well are easier with the described optimization method as simple proxy models are trained after collecting more production rate samples. By comparison, full reservoir simulation model optimization takes too long a time to make their use practical in everyday applications.

Acknowledgments

I start my acknowledgment by thanking Professor Roland Horne for being the perfect research adviser during my PhD. His wise supervision style brought a lot of relief to a very stressful and demanding task. His help was not limited to guiding this research as he set a great example to be followed both on the personal and professional level. Special thanks go to Professor Khalid Aziz. It was a privilege to gain my first research experience under such a knowledgeable person. Thanks are also extended to my other committee members: Professor Tapan Mukerji, Professor Louis Durlofsky, and Professor Steven Gorelick for their valuable feedback on my work.

I am very grateful to all other professors of the Department in Energy Resources Engineering. In particular, my involvement in the SUPRI-D and Smart Fields research programs have enlightened me with a lot of ideas along the way. Many thanks go to the staff and students of the department for providing a very productive and challenging learning environment.

The completion of this work would not have been possible without the technical contribution of many individuals. Of special mention, I thank Dr. Jinjiang Xiao at Saudi Aramco, Dr. Mahmoud Farhadiroushan at Silixa, and Dr. Mahdy Shirdel at Chevron. Thanks to several colleagues for their help in different parts of the work including Dr. Obiajulu Isebor, Dr. Hai Vo, Sumeet Trehan, and Dr. Zhe Wang.

My time at Stanford has been enriched with many new experiences and friendships. In particular, I appreciate all members of the Saudi community for making me feel at home. I also thank my office mates: Dr. Maytham Al Ismail, Dr. Mohammad

Bazargan, Moataz Abu AlSaud, and Julio Mendes for all the memories.

I am indebted to my amazing family who supported me despite the long distance separating us. Mostly, I would like to thank my parents Yasin and Wajiha. They have sacrificed a lot to provide us the best life and education they could afford. I also want to express my gratitude to my parents-in-law, Mohammed and Fatima, for treating me like their own son and for always keeping me in their prayers. My thanks also go to my great siblings: Dr. Nader (أَدب), Amina (أَدبية), Fatima (أَدوب), Amal (أَدب), Eman (إيداب), and the not so great one: Abdullah (أديب) ;). Each of you holds a special place in my heart. I cannot forget to thank my colleague and cousin Ali (الزميل وولد خالتيه), who did not let a day pass by without asking about me. Last but not least, my deepest appreciation goes to the love of my life, Eman. It is not an overstatement that I think her efforts during this journey were not less than mine. Oh, and one last thanks go to my slightly annoying but precious angels, Mahdi and Moayad (Figure 1). Their presence brought unlimited joy to my life.



Figure 1: Little cuties with big dreams.

Thank you God for giving me strength and guidance; I am forever your servant.

Contents

Abstract	v
Acknowledgments	vii
1 Introduction	1
1.1 Technology Description	2
1.1.1 Smart Wells	3
1.1.2 Fiber Optical Distributed Sensors	7
1.2 Literature Review	10
1.2.1 Using Acoustics in Fluid Flow Metering	10
1.2.2 Using Temperature to Measure and Model Flow	12
1.2.3 Smart Completion Optimization	14
1.3 Research Objectives	18
1.4 Dissertation Outline	22
2 Inflow Profiling With Distributed Acoustic Sensing	23
2.1 Raw Acoustic Data Preprocessing	24
2.2 Transforming Acoustic Data to the f - k Domain	28

2.3	The Speed of Sound in Pipe Flow	30
2.3.1	Mechanism of Acoustic Wave Propagation in Pipe Flow	30
2.3.2	Measuring the Speed of Sound from the f - k Domain	32
2.3.3	Fluid Mixing Model for Phase Fraction Calculation	37
2.3.4	Factors Affecting Single-Phase Speed of Sound Values	41
2.4	Flow Velocity Calculation from the Doppler Effect	45
2.5	Results and Discussion	46
2.5.1	Analysis of Experimental Acoustic Data in Ambient Air	46
2.5.2	Analysis of DAS Data in Single-Phase Oil Producer	49
2.5.3	Analysis of DAS Data in an Oil Producer with High Water Cut	61
2.6	Concluding Remarks	66
3	Inflow Profiling With Distributed Temperature Sensing	69
3.1	The Joule-Thomson Coefficient	71
3.1.1	Joule-Thomson Coefficient for Mixtures	72
3.1.2	Well Completion Design to Capture the Joule-Thomson Coefficient	75
3.2	Practical Application for Inflow Profiling Using DTS	78
3.2.1	Solution for Single-Phase Flow	79
3.2.2	Example in an Oil-Gas Producer	81
3.3	Integrating DTS with DAS and Applications in Three-Phase Flow	84
3.3.1	Lumping Oil and Water as One Liquid Phase	86
3.3.2	Solving the System of Nonlinear Equations with Least Squares	88
3.4	Concluding Remarks	93

4	Application in History Matching and Production Optimization	95
4.1	The Main Optimization Engine	96
4.2	Modeling Inflow Control Devices	100
4.3	Production Optimization in Smart Wells	101
4.3.1	True Optimum Search Test	102
4.3.2	Maximizing Oil Recovery in Two-Phase Flow	106
4.4	Application in History Matching	111
4.4.1	Describing the Kalman Filter	111
4.4.2	History Matching Results	114
4.5	Improving Optimization with Downhole Measurements	118
4.5.1	Method 1: Using Artificial Neural Networks	121
4.5.2	Method 2: History Matching a Reduced-Physics Model	126
4.6	Concluding Remarks	136
5	Conclusions and Recommendations for Future Work	137
5.1	Conclusions	138
5.2	Future Work	140
A	The Integral Image Value Algorithm	143
B	Coupled Reservoir/Wellbore Thermal Model	147
	Nomenclature	151
	Bibliography	157

List of Tables

2.1	Fluid properties used to solve the two-phase fraction model.	39
2.2	Calibration coefficients used to find the crude oil and process water properties.	42
2.3	Interval Control Valve properties for Well-A.	49
2.4	Comparing flow rate results from DAS analysis with surface measurements for all flow scenarios. Flow rates corresponding to fully-open ICVs within a case are underlined while those representing fully-closed ICVs are between parentheses. Unformatted flow rates refer to ICVs that are 50% open.	60
2.5	Approximate production contribution percentage from each interval for the different flow scenarios. Fully-open ICVs in the case are underlined while fully-closed are between parentheses.	60
2.6	Well-B ICV details and results summary.	61
3.1	Fluid thermal properties used to solve the correlation between phase fraction and Joule-Thomson coefficient	75
3.2	Properties used to solve three-phase flow.	87
4.1	Reservoir and fluid parameters for the well control optimization example.	103
4.2	ICV setting of each zone as the optimization run progressed.	106

4.3	Summarizing results of the tested optimization cases. In the Base Case, all valves all open throughout productions. Case 1 finds the optimal initial valve settings, while Case 2 finds optimal settings at three different time steps (1 : initial setting, 2 : at 480 days, and 3 : at 720 days).	107
4.4	Reservoir and fluid parameters for the SPE 9 Model.	119
4.5	Upper and lower search bounds to construct absolute permeability and relative permeability curves for the coarse model. Listed optimum values correspond to solutions for fitting with ten ICV setting samples.	130
4.6	Economic parameters used to calculate the NPV for this example. . .	133
4.7	Optimum valve settings from the true model compared to solutions provided by the reduced-physics models. Results for the base upscaled model are shown in addition to results for matching using surface and downhole measurements. Bold valve setting values signify exact match with the true model and underlined values indicate a difference of one position compared with the true optimum.	134

List of Figures

1.1	A sketch of the main components of smart wells and how the completion can be used for selective production from multilayered reservoir. From Bhattacharya and Rao (2011).	5
1.2	The use of ICV valves in a multilateral well. From Mubarak et al. (2009).	6
1.3	Plan and design for MRC well Shaybah-220. From Saleri et al. (2003).	6
1.4	Acquiring backscattered light data of an acoustic field through a DAS system. From Johannessen et al. (2012).	9
1.5	Laser pulse path from the surface unit into the well and vice versa.	9
1.6	Analyzing the different spectral parts of scattered light.	10
1.7	Closed-loop approach to achieve continuous flow measurement, control and optimization.	19
1.8	Flowchart for the overall integrated procedure.	21
2.1	Procedure of calculating flow velocity and phase fractions using DAS data.	25
2.2	Example of raw acoustic data collected from a multilateral well. High noise levels are observed against the ICVs, which are represented by red lines at the right end of the figure. The original high-resolution image contains 12 gigapixels. This image was constructed by extracting five seconds of data at a time (800 MB).	27

2.3	Parsing the raw data into different blocks for processing. Each subsequent block includes half the spatial samples from the previous block to increase spatial resolution of the results. Each processed block results in a velocity and phase fraction reading at that location in that instance of time.	28
2.4	A sensor array picking up noises from the eddies as they arrive to the sensor location. Top sketch from Gysling and Loose (2004)	31
2.5	Mechanism of generating acoustic waves as the production fluid passes through an ICV.	32
2.6	A frequency-wavenumber plot shows two distinct lines representing the upgoing (positive slope) and downgoing (negative slope) speed of sounds. Note that we are plotting the wavenumber not the angular wavenumber.	33
2.7	Image integral values for a range of possible slopes for the downgoing (left) and upgoing (right) speed of sounds. The most probable value is shown in red.	35
2.8	Comparing the integral value behavior when the speed of sound line is clear in the image (left) with a case where the speed of sound (in ft/s) is not clear (right). This is reflected in the lower plots with narrow confidence interval in the left plot and a wide one for the right plot.	36
2.9	Speed of sound as a function of the heavier phase volume fraction for three different fluid mixtures. The black dotted line corresponds to a speed of sound measurement of 400 m/s.	40
2.10	The speed of sound in (a) water and (b) air as a function of temperature along isobars. The bold lines represent values on the saturated liquid and vapor curves. Vertical isobars in the top plot represent the region of liquid-vapor phase separations where the thermodynamic speed of sound is not defined for the two-phase system. From Levy et al. (2001).	43

2.11	Speed of sound in an oil-water mixture with varying oil phase fraction at different temperatures. These solutions were found using Chaudhuri et al. (2012) empirical correlations.	44
2.12	Effect of the Doppler shift on frequency observed by two sensors along the flow direction.	46
2.13	Experimental setup with the sensors at the bottom and the speakers at top. The red box encloses sensors that were used for this analysis. From Weinstein et al. (2016)	47
2.14	Speed of sound line-fitting in the f - k domain for experimental acoustic data in ambient air.	48
2.15	Completion sketch for a tri-lateral oil producer with three production segments. From Al-Arnaout et al. (2008).	50
2.16	Root mean square values averaged over the test interval for four investigated flow scenarios.	52
2.17	Frequency spectrogram for the four cases plotted against main bore distance.	53
2.18	Upgoing (middle) and downgoing (right) speed of sound results after feeding the data to the signal processing algorithm. The plot to the left shows well completion details.	54
2.19	Speed of sound confidence interval for the second flow case. Green circles represent the most likely value and green bars represent the uncertainty range.	56
2.20	Speed of sound confidence interval for the first flow scenario. Green circles represent the most likely value and green lines represent the uncertainty range. Most calculated values have high uncertainty or are outside the expected range.	57

2.21	Flow rates calculated from DAS data compared with surface flow meter flow rates. ICV settings for the three cases are annotated below the red lines.	59
2.22	Well completion details for Well-B.	62
2.23	Upgoing and downgoing speed of sound calculated in ft/s at different time and well distances. Horizontal lines mark the ICV locations and the slope line in the left plot follows movement of the oil phase in the third production zone.	63
2.24	Typical $f-k$ plot for Well-B shows low SNR in the downgoing speed of sound (left), whereas the upgoing speed of sound line is easily detectable (right).	64
2.25	Close-up of the smart completion unit in Well-B highlights expected cocurrent and countercurrent fluid movement behind the pipe.	65
2.26	Calculation of the oil phase fraction as a function of well distance provides an insight of the oil contribution from each production zone.	66
3.1	DTS data example recorded in °C as a function of depth and time . . .	70
3.2	Joule-Thomson effect as a function of the heavier phase volume fraction for three different fluid mixtures.	74
3.3	Difference between mixing temperature, T_m ; entry temperature, T_e ; and geothermal temperature. From Wang (2012).	76
3.4	Suggested completion configuration to capture all needed values for the Joule-Thomson coefficient calculation.	77
3.5	Radial reservoir simulation model used to replicate DTS in providing reservoir and wellbore temperature data.	79
3.6	Single-phase reservoir and wellbore simulation data for (a) gas and (b) water. Cooling/heating effects associated with thermal expansion of the two fluids is apparent in the plots.	81

3.7	Temperature as a function of distance from the wellbore for single-phase water production. Approximate locations of the tubing, the annulus, and the casing are indicated in gray.	82
3.8	Comparison of the Joule-Thomson coefficient from the simulator and from EoS equations for single-phase (a) gas and (b) water.	82
3.9	(a) Temperature and (b) pressure data as reported at the sandface (T_{sf}) and wellbore (T_{well}) by the simulator for an oil-gas flow.	83
3.10	(a) Gas holdup solution from the simulation and from our developed C_{JT} equation. (b) Errors from the equation are within $\pm 5\%$ from simulation results.	84
3.11	Three-phase fluid fractions based on speed of sound in the mixture and fluid density. DAS alone cannot resolve the system requiring an additional reading of water cut, gas holdup, or density.	85
3.12	(a) Gas and (b) oil holdup absolute errors when the oil and water are represented as one liquid phase (Lumping 1). The same results are presented in (c) and (d) for Lumping 2.	90
3.13	(a) Gas and (b) oil holdup absolute errors when solving the nonlinear system of equations using a least squared optimization problem. (c) and (d) show improvement in results when an informed initial solution is specified.	91
3.14	Minimum absolute error in calculated (a) gas and (b) oil phase fraction from three proposed solution methods. Lower plots show the most accurate method to get (a) gas and (b) oil holdup.	92
4.1	The interface between the optimization algorithm and the reservoir simulator.	96
4.2	Reproduction procedure in GAs.	97
4.3	Flowchart of the overall optimization procedure using GAs.	99

4.4	Representation of the different nodes in the multi-segment network model.	100
4.5	Permeability of the reservoir model used for the well control optimization example.	103
4.6	Progression of the objective function fitness for three different optimization runs. On average, the true optimum was found after 18 iterations.	104
4.7	The well flow profile for the optimum solution. Production from each zone (incremental total production rate) is proportional to the zone's permeability.	105
4.8	(a) Permeability and well locations for the reservoir model. The oil saturation map for the optimum valve setting at the end of simulation for the Base Case, Case 1, and Case 2 are shown in (b), (c), and (d), respectively.	108
4.9	Oil production rate (left) and water cut (right) for the Base Case and optimum solution from the two cases.	109
4.10	Flow contributions from each production zone for Case 1 at three different time steps, (a) the first time step, (b) after 480 days, and (c) after 720 days. The same is shown for Case 2 in (d), (e), and (f). . .	110
4.11	Illustrating the effect applying the Kalman update after each simulation step. The ensemble results are brought closer to true observations after each update.	113
4.12	(a) The true model permeability logarithm. The prior mean of permeability logarithm is shown in (b). The final history-matched permeability field for the three methods are shown in (c), (d), and (e). . . .	116

4.13	Oil (a through d) and water (e through h) production rates for all realizations for the prior models and the three history matching cases. The true production rate is shown in red, while the average production rate from each case is plotted in green.	117
4.14	The root mean square error in oil and water production rate after history matching using three different types of measurements.	118
4.15	The multilateral well configuration shown with (a) the initial oil saturation and (b) the permeability distribution.	120
4.16	Steps of constructing a proxy model based on true model data.	121
4.17	Artificial neural network structure. n , m , and p refer to the number of inputs, outputs and hidden nodes, respectively. Indexed x , y , z 's refer to a specific node in the input, output or the hidden layer. h represent weights between the input and the hidden layers, while g represent weights between the hidden the output layers.	122
4.18	Root mean square error after fitting the neural network with downhole (blue) and surface (red) measurements using different ICV control samples.	124
4.19	ANN regression results comparing the fit when surface measurements (left) are used opposed to downhole measurements (right). Plots to the bottom show the effect of increasing the number of ICV combination samples.	125
4.20	Cash flow results when the ANN proxy is used for optimization. The ANN trained with Downhole measurements (blue) generally show a better result than that trained with surface measurements (red).	127
4.21	Permeability distribution of the fine and coarse model.	128
4.22	Oil and water relative permeability curves. Solid lines represent the fine model and dashed lines are relative permeability curves in the upscaled model that achieved the best match with the fine model.	130

4.23	Root mean square error after updating the coarse model with downhole (blue) and surface (red) measurements using different ICV control samples.	132
4.24	NPV of the three optimization cases on the upscaled model as compared to optimum NPV results of the true model.	135
4.25	Total field oil (left) and water (right) production rates for the true model and the three optimization cases.	135
5.1	Procedure of real-time model update and valve setting optimization with the help of distributed downhole measurements.	142
A.1	Example of a frequency-wavenumber grid and the resulting intersection points when a slope line is drawn on the image. The integral value method calculates the slope line length in each cell by determining the intersection points.	145
B.1	Schematic of a deviated wellbore with fluid influx upstream of the current producing perforation.	149

Chapter 1

Introduction

Over the past few decades, oil and gas wells evolved from being simple vertical wells to slightly deviated wells until horizontal wells eventually became the industry standard in many areas of the world. The advancement in drilling has triggered a similar boom in completions, where many new devices were implemented in these expensive wells for better monitoring and control. This eventually led to the development of increasingly more complex well architectures with more control and monitoring capabilities. Although the need for such advanced wells originated as a facilitator to meet the growing energy demand worldwide, there is still wide application for them in the current low oil price market. This is because multilateral smart wells provide better reservoir management and ultimate recovery factors from mature fields. In addition, efficient reservoir compartmentalization provided by advanced wells makes them an ideal option for hydraulic fracturing applications in unconventional gas targets (Molenaar et al., 2011).

The term “smart well” is commonly defined as a well having remotely operated control devices with some form of data measurement in the completion string (Turner, 2012). These monitoring and control capabilities come in different forms. Inflow Controls Valves (ICVs) and fiber optical distributed measurements are two prominent tools that achieve this. The combination of both tools provides an opportunity to adjust well production by choking valves based on observations made in real-time to

hinder production of unfavorable fluids. Changing downhole conditions provides new production data and this management loop can be closed with an effective production optimization algorithm. Engineering intuition and conventional data measurements are often insufficient to obtain the optimal well completion design due to the geological complexity and the nonlinear nature of the problem. The incremental value of nonconventional wells might be diminished if wells are not operated optimally. Currently, the settings of many ICV completions are not adjusted regularly. Even if they are adjusted, it is often performed by a trial-and-error approach. The standard practice to test multiple completion scenarios is very time-consuming and would rarely succeed to reach an optimal point due to the multidimensional solution space and the large number of parameters.

The main objective of this research was to investigate optimization for smart well completions by modifying their controls based on interpretation of distributed downhole measurements. We began the work by investigating how information about the fluid flow rate and phase fractions could be inferred by analyzing acoustic and temperature distributed measurements. Then, we investigated how such information could play an essential part in improving the productivity of a smart well by building an optimization algorithm around this scheme.

1.1 Technology Description

To provide a clear picture about the nature of measurements and to understand the limitation of the tools, a description of the technology and some background about the theory behind it is presented in this section. ICVs and distributed sensors are types of advanced completion. While the first tool is the part of smart wells that allows us to control different intervals of the well, the latter provides engineers with the data required to make an informed decision when a control adjustment is intended.

1.1.1 Smart Wells

Smart or intelligent wells are considered superior to conventional wells due to two distinctive aspects. First, they are completed with monitoring and control capabilities, that allows for well compartmentalization. The monitoring and control instrument within each compartment is referred to as a smart completion unit. Each unit is run in the well as part of the tubing below the main production packer. As depicted in Figure 1.1, a smart production zone consists of several components. Swell packers are set above and below the zone of interest to isolate it from other zones. A pressure/temperature dual gauge is connected to an electrical line to provide continuous measurements to the surface. The last component is the ICV, which is usually equipped with a sliding sleeve and several ports to allow fluid flow from the annulus to the tubing. If choking is desired, pressure is applied to a hydraulic line that is attached to the ICV and runs all the way to surface. Once pressure increases in the hydraulic line, the sleeve starts to slide to isolate a portion of the ports to restrict or completely shut-off production from some zones (gas intervals, for example) according to the choke setting. In early versions, ICVs had discrete number of settings but current valves can be adjusted at infinitely continuous positions (Turner, 2012).

The second unique aspect of smart wells is their architectural complexity driven by extended reservoir contact lengths. This complexity ranges from a long horizontal well with multiple compartments to multilateral wells with control capability within each lateral. In a smart multilateral well, a main bore is drilled first and several laterals kick off from the main bore. When the completion is run, ICVs are installed opposite of each lateral such that flow from a particular lateral can be isolated easily if it starts producing water or gas at high rates (Figure 1.2). Further design enhancement is ongoing to overcome the difficulty of running the ICVs inside laterals (Mubarak et al., 2009). Maximum Reservoir Contact (MRC) wells, which have several laterals emanating from the well's main bore, represent a distinctive example in this category. For instance, the well Shaybah-220 (Figure 1.3), which was completed in south eastern Saudi Arabia by the end of 2002, had eight laterals and a total length of 40,384 feet. This huge reservoir contact area is equivalent to several standard horizontal wells.

Economic studies on the well showed a four-fold reduction in unit development cost and production testing indicated a five-fold increase in productivity index compared to horizontal wells completed in similar facies (Saleri et al., 2003). Several other studies showed that the performance of nonconventional wells is superior in other areas as well compared to conventional wells. Horn et al. (1998), Taylor and Russell (1997), and Temizel et al. (2015) summarize these advantages as:

- Extending reservoir contact length and drainage area
- Increasing net worth of the drilling investment to exploit the asset
- Improving zonal monitoring and allocation
- Minimizing operating cost and the need for intervention
- Reducing operational drawdown pressure
- Controlling the producing gas-oil ratio

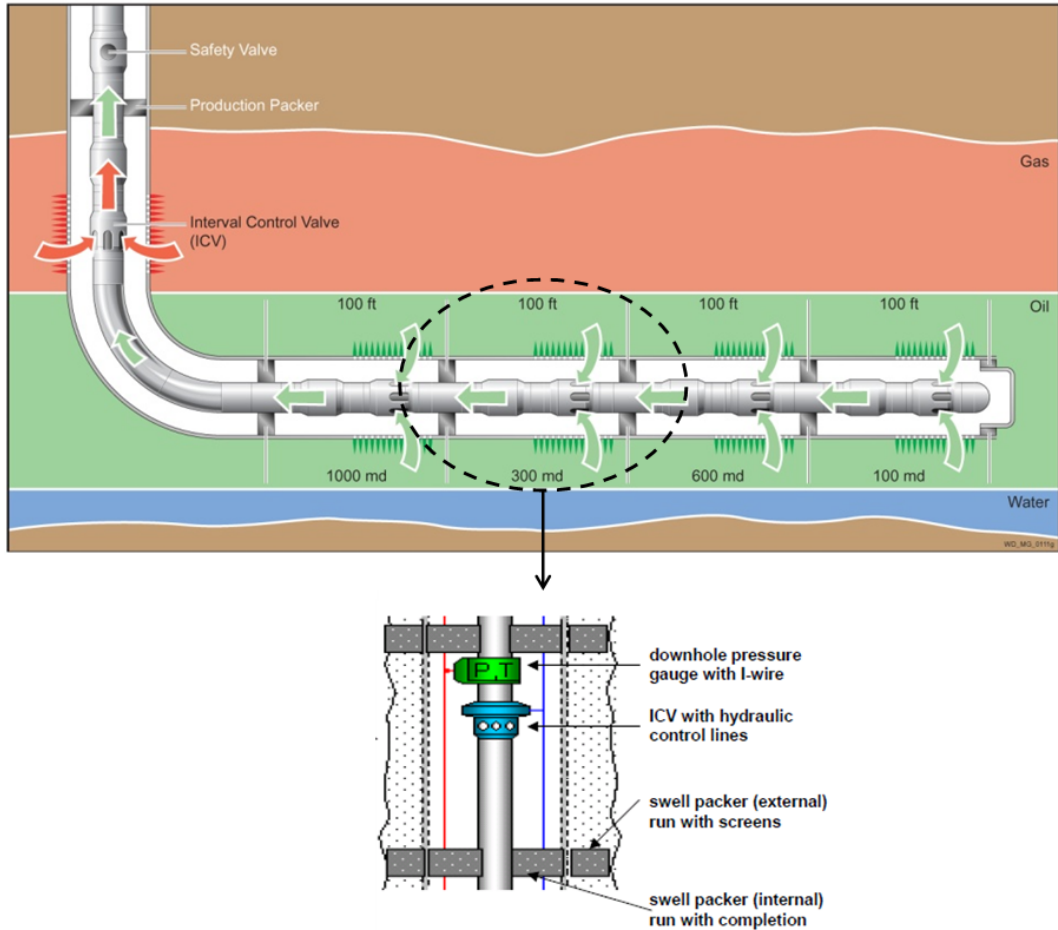


Figure 1.1: A sketch of the main components of smart wells and how the completion can be used for selective production from multilayered reservoir. From Bhattacharya and Rao (2011).

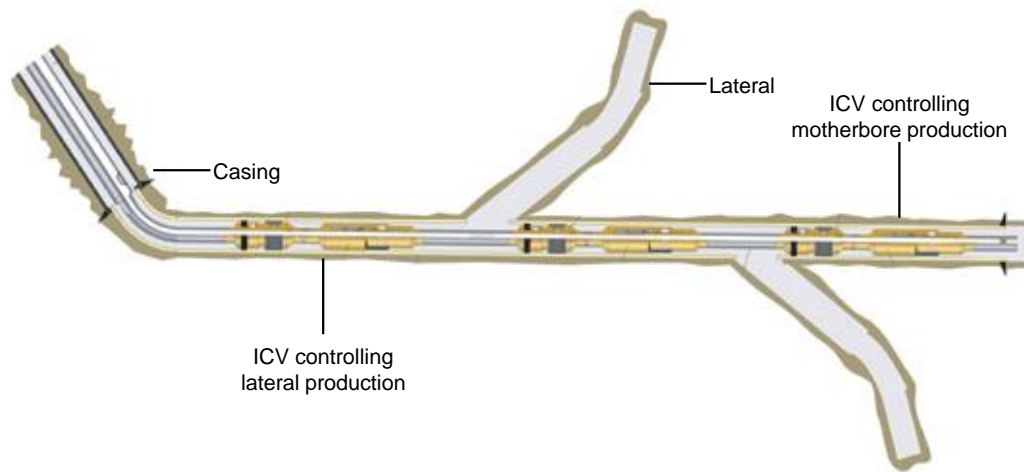


Figure 1.2: The use of ICV valves in a multilateral well. From Mubarak et al. (2009).

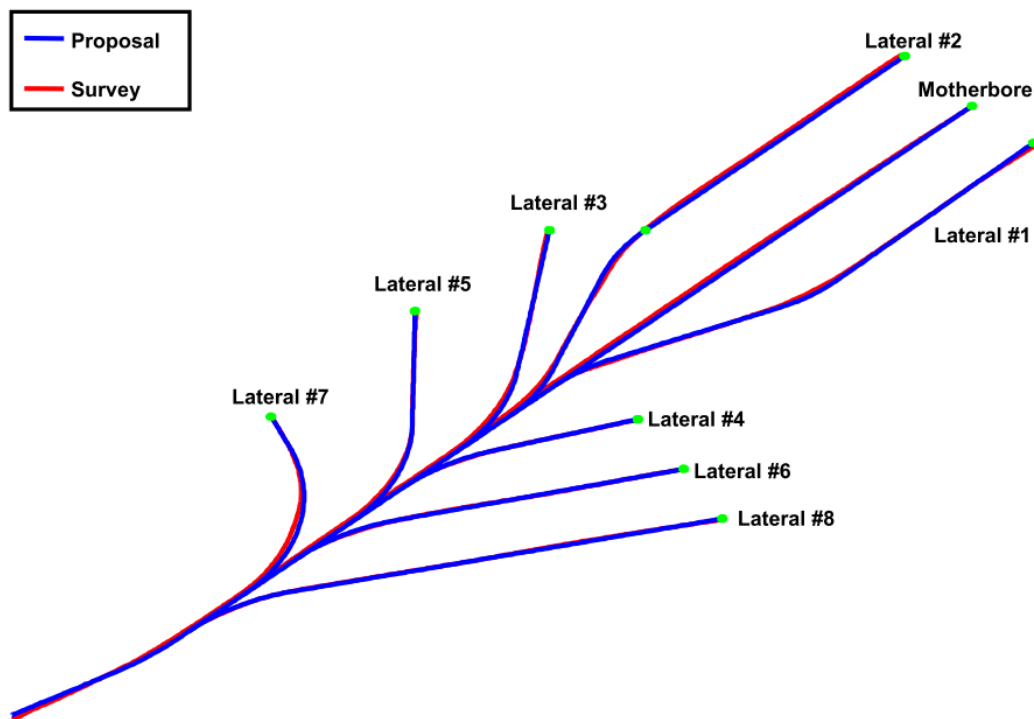


Figure 1.3: Plan and design for MRC well Shaybah-220. From Saleri et al. (2003).

1.1.2 Fiber Optical Distributed Sensors

One of the challenges in smart wells is that sensory devices are currently limited to the main bore of the well because they are packaged with the ICVs, which cannot be installed inside the lateral. Running smart wells with fiber optical sensors presents an opportunity to overcome this limitation by collecting data from the laterals. Currently, fiber optical sensors provide temperature and acoustic data that are distributed in time and space along the wellbore.

The process of acquiring distributed measurements begins by sending a laser pulse into a fiber optic line. Optical fibers are thin flexible cables consisting of glass (silica) threads that are capable of transmitting light waves. The traveling light within the fiber undergoes backscattering as it encounters minute changes caused by flow acoustic waves when traveling through the line (Figure 1.4). The backscattered laser light goes through an Optical Time-Domain Reflectometer (OTDR) that is connected to the end of the fiber optic line at the surface (Figure 1.5). The OTDR interrogation process detects the spectral wavelengths of the backscattered light, which contains three different spectral bands: Rayleigh, Brillouin, and Raman scattering (Figure 1.6). Chandrasekhara Raman (Raman, 1928) was the first to identify the dependency of laser backscattering and temperature. The local temperature of the optical fiber is derived from the ratio of the anti-Stokes and Stokes parts of Raman light intensities (Bohning et al., 1998). Current Distributed Temperature Sensing (DTS) installation can measure temperature with precision up to 0.1 °C, which can be significant in analyzing temperature changes in horizontal wells (Johannessen et al., 2012).

Similarly, acoustic amplitude can be computed from the Rayleigh scatter. The length of an interval that corresponds to an analyzed backscattered light depends of the duration of the light pulse, which follows from the OTDR interrogation process (time to wavelength processing). Currently, the finest spatial resolution achieved is 0.5 m with varying temporal sample frequency (MacPhail et al., 2012).

With the introduction of complicated well architecture and trajectories, well intervention for data collection became very challenging. Installation of fiber optic

lines along these wells provided an ideal solution to minimize well intervention (Pinzon et al., 2007). In addition to using Distributed Acoustic Sensing (DAS) for flow profiling, it has been used in several other applications such as:

- Hydraulic fracture propagation monitoring (Bakku et al., 2014; Boone et al., 2015; Denney, 2012; MacPhail et al., 2012; Martinez et al., 2014; Molenaar et al., 2012).
- Vertical Seismic Profiling (VSP) and detecting microseismic activity (Mateeva et al., 2012; Mestayer et al., 2011; Nizkous et al., 2015; Poletto et al., 2014; Ugueto et al., 2014; Webster et al., 2013; Zhan et al., 2015).
- Electrical submersible pump performance surveillance (Allanic et al., 2013).
- Tubular and pipeline leak detection (Boone et al., 2014; Siebenaler et al., 2015; Thodi et al., 2014).
- High pressure/temperature and geothermal applications (Becker et al., 2016; Paulsson et al., 2014)
- Gas-lift and wax deposition monitoring (In't Panhuis et al., 2014).

The optical fibers can be installed either inside the tubing string to measure mixing properties or behind the casing to measure properties at the sand-face depending on the application and the operator's preference.

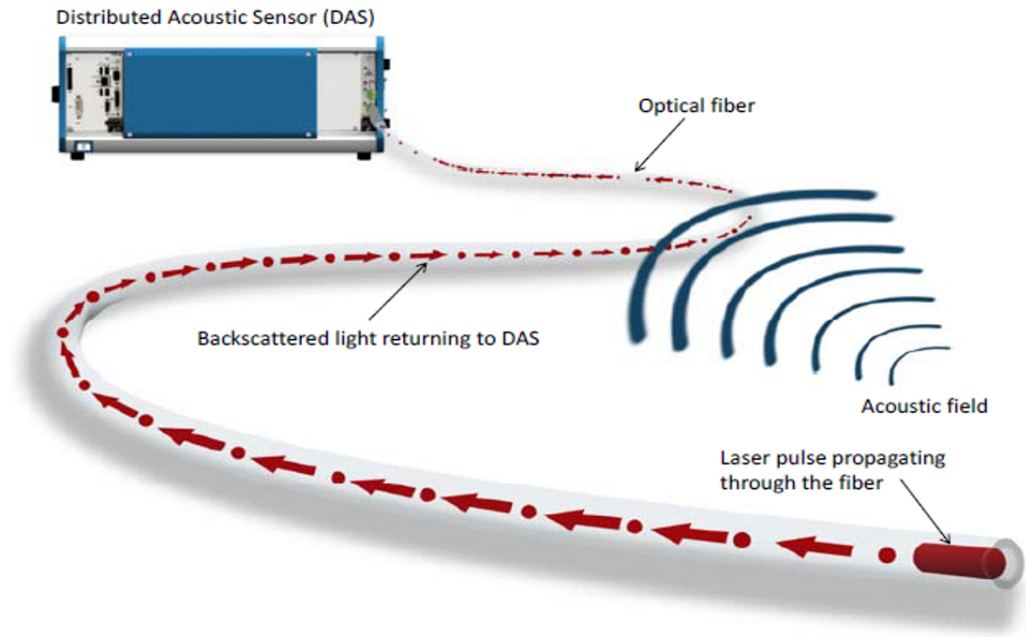


Figure 1.4: Acquiring backscattered light data of an acoustic field through a DAS system. From Johannessen et al. (2012).

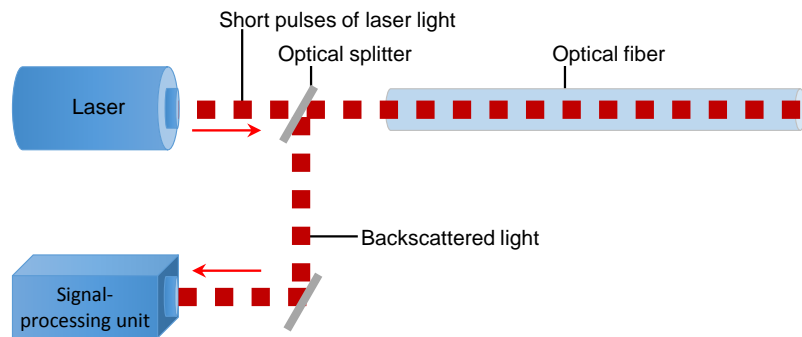


Figure 1.5: Laser pulse path from the surface unit into the well and vice versa.

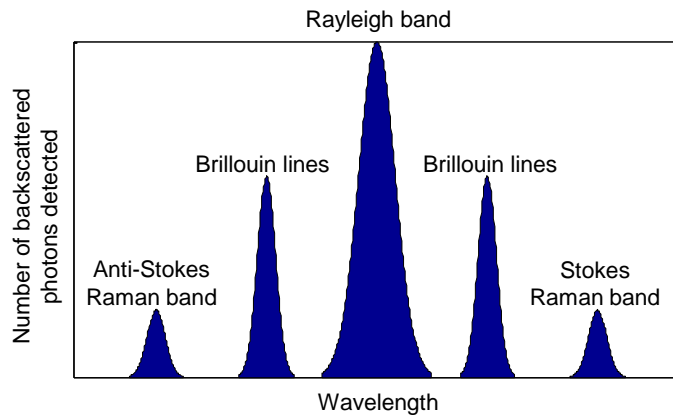


Figure 1.6: Analyzing the different spectral parts of scattered light.

1.2 Literature Review

In this section, we present a survey of previous work related to using DAS and DTS in fluid flow monitoring and to well control production optimization.

1.2.1 Using Acoustics in Fluid Flow Metering

The idea of logging noise to identify downhole fluid movements is quite old and was first suggested by Enright (1955). He suggested lowering a listening device downhole and correlating the leak point with the peak recorded noise. The concept did not become successful until McKinley et al. (1972) utilized the noise log as a spectrograph of relative amplitude against frequency. Leaks were associated with maximum noise amplitudes and high pressure gradient levels. These methods were, however, limited to tracking slow fluid movements as equipment capabilities only recorded low frequency ranges.

The first real attempts to develop a downhole flow meter based on measuring flow noises began at the turn of the millennium with the emergence of Sound Navigation and Ranging (SONAR) technology to measure volumetric flow rate. Current commercially available flow meters based on this technology use an array of sensors to

track spatially coherent structures (eddies) that are traveling with the flow. The signals from each sensor are then processed to deconvolve its frequency and wavelength, which are then used to calculate the convection velocity of the eddies and the speed of sound within the fluid. Testing has shown that the technology is only suitable for relatively high rate wells (Silva et al., 2012).

Ünalimis et al. (2010) described another downhole flow meter that was tested in a smart well in Saudi Arabia based on acoustic measurement to calculate the speed of sound. Results showed accurate measurements for two-phase oil and water applications. In the presence of gas, results were only acceptable qualitatively. The flow meter consists of an outer pipe with a fiber coil wrapped around the outer surface of it. As flow goes through the pipe, acoustic waves cause local changes in the radial strain of the pipe wall. This strain is captured by the optical sensors and the fluctuating pressure (and hence the flow velocity) is calculated by relating the strain to the pipe radius and pipe thickness. Ünalimis and Trehan (2013) later extended this work for three-phase flow problems by installing a pressure drop sensor to estimate frictional losses based on a modified Chen (1979) correlation. From that, they estimated the Reynold's number and the mixture density. In theory, the fraction of all three phases can be determined with the calculated mixture density and speed of sound. The meter was tested on a horizontal flow-loop and results were within 5% of reference flow rates based on an electromagnetic flow meter. However, it required accurate estimation of the pipe roughness prior to the test.

DAS represents an evolution over the aforementioned flow meters because it provides distributed measurements not only in time but also in the space domain. Although flow metering was not the initial purpose of its installation, the premise of DAS provides a powerful approach to calculate in-situ phase fractions. Johannessen et al. (2012) applied a number of fast signal processing techniques to DAS measurements to characterize the flow along the wellbore. As a result of this process, the propagation of acoustic energy along the wellbore can be analyzed in the space-frequency domain, which enables the calculation of speed of sound. The speed of sound within a fluid mixture was used to find the in-situ phase fractions as a function of the mixture

density and compressibility using Wood's (1941) correlations (derivation shown in Section 2.3.3). Johannessen et al. also calculated the flow velocity using the Doppler shift observed between downgoing and upgoing speed of sounds.

Chaudhuri et al. (2012) extended this approach for fluid flow in pipes and conducted a set of flow-loop experiments to test the algorithm. Results of a two-phase oil-water mixture were within 1% compared to a Coriolis meter within this controlled environment. More recently, additional work has been conducted to test this methodology on real fields. For example, Paleja et al. (2015) showed that it is possible to detect gas or water breakthrough in an oil producer by tracking spatial and temporal speed of sound changes. Their work also demonstrated the use of DAS data to monitor the height of liquid column in the annulus in a smart gas-lifted oil producer. Xiao et al. (2014) conducted a number of tests on water injection and oil production wells with varying success. Most notably, they were able to allocate water injection into two compartments for seven different choke settings. When compared to results from a Production Logging Tool (PLT), the highest error was about 20%. In oil-water production wells, results were inconsistent; accurate flow velocity and phase fraction measurement were only obtained in well sections where the acoustic energy propagation is strong and continuous. Xiao et al. (2015) improved results by increasing spatial resolution, inducing seismic shots during the test, and stacking data to improve signal-to-noise ratio.

1.2.2 Using Temperature to Measure and Model Flow

Temperature modeling in reservoir engineering has been studied for the past 50 years with Ramey (1962) proposing one of the earliest approaches. As more understanding of the heat transfer phenomena was developed, Kabir et al. (1996) derived a detailed wellbore model that accounts for tubular heat absorption and thermal storage effects. The model is based on mass, momentum and energy balance. However, this model assumed that the well entry temperature is equal to the geothermal temperature at that depth. Shortly after that, several field observations started to report

temperature variations along horizontal wells, which indicated that wellbore entry temperature is not only a function of geothermal temperature. Because the different temperatures were associated with sections of the well that operate under different drawdown pressure (but at the same depth), this temperature variation was attributed to the Joule-Thomson effect (Carnegie et al., 1998; Chace et al., 2000; Foucault et al., 2004).

Here, emphasis is placed on studies that involved DTS or ICVs. As DTS installations increased during the past two decades, many reservoir temperature models (Hasan et al., 2009; Muradov and Davies, 2012; Tabatabaei et al., 2011) have been developed to interpret DTS data for vertical and horizontal wells. Those models have incorporated subtle thermal changes in the reservoir to account for multiphase flow under the assumption that the arriving temperature is equal to the geothermal temperature plus the Joule-Thomson effect. Average drawdown pressure is used to estimate the Joule-Thomson effect.

Prior to that, Ouyang and Belanger (2006) presented an inverse model to solve for flow rate using DTS data. They concluded that the method can only be used properly to estimate flow rate in deviated well with an angle less than 75° (from vertical) due to weakened hydrostatic and geothermal temperature variation effects in highly deviated wells. Previously discussed model studies did not present sufficient evidence in real wells to refute their claim. Wang et al. (2008) used tight gas production data to validate Hasan's model. The model run was successful except for sections of the well where temperature oscillation was greater than 5°F . Another run was performed after recalibrating the fiber and smoothing the DTS data, which achieved an almost perfect match with PLT production data. They did not test horizontal or multiphase flow wells.

Yoshioka (2007) developed a reservoir model that was discretized to finite segments, where single-phase flow is present over each segment and temperature is assumed to be constant over time. Analytical solutions to describe the relationship between flow, pressure, and temperature were used by solving the mass, momentum,

and energy balance equations. Yoshioka used the total flow rate and distributed temperature data as observations and inverted for inflow distribution using the Levenberg-Marquardt (LM) Algorithm. The method was applied successfully to a synthetic case with vertical and horizontal well in both single-phase and pseudomultiphase flow (the model was divided into a finite number of segments with single-phase, steady-state flow through each segment). Li and Zhu (2010) used Yoshioka's forward model and a Markov Chain Monte Carlo method for inversion, applying the method to a real data set with satisfactory results.

Wang (2012) used a similar scheme but enhanced the model to account for multicomponent systems. A least-square and a linear inversion method were applied to infer flow rates from DTS data, which was tested on synthetic and real flow scenarios. While both approaches worked in single-phase flow, the least-square method required knowledge of flow entry interval to converge in most cases. For multiphase flow, however, Wang concluded that temperature data alone are not sufficient and additional data are required to estimate the flow rate profile successfully.

While most of this work assumed steady-state models, Duru and Horne (2008) and Sui et al. (2008) developed thermal models that capture transient behavior of both the wellbore and reservoir models. The wellbore model was developed for vertical wells, and radial flow was used in the reservoir model. Duru used temperature and flow rate data to invert for porosity and permeability using Ensemble Kalman filters (EnKF). The practice showed improved results over inversion using flow rate data alone. Sui's work showed that the transient well model can be reduced to a steady-state condition if the observed time is long.

1.2.3 Smart Completion Optimization

Copious and diverse research related to smart well optimization has been discussed in the literature. This section is dedicated to surveying current and past developments in smart well controls optimization using reservoir simulation and/or well measurements. To begin, we shed some light on work that applied general optimization studies on

smart well controls. Isebor (2009) compared the performance of several gradient-free methods like the Genetic Algorithm (GA), direct-search methods, and combinations of the two. He used these algorithms to optimize smart well control variables with multiple nonlinear constraints on a channelized synthetic two-dimensional model. He also applied penalty functions to account for constraint violations. He concluded that, for problems considered, General Pattern Search (GPS) with penalty functions perform the best followed by the combined GA and GPS algorithm.

Yeten (2003) applied a GA with binary coding to optimize well type, location, and trajectory for nonconventional wells. Along with that, he developed an optimization tool based on a nonlinear conjugate gradient algorithm to optimize smart well controls using both reactive and defensive control strategies. The algorithm was applied to vertical wells in a layer-cake reservoir and to multilateral wells in a complex channelized reservoir. The use of optimized settings for ICVs showed an improvement up to 65% over the uninstrumented base case.

Several researchers used the model developed by Yeten to conduct further studies and to enhance its capabilities. Notably, Rigot (2003) extended the optimization engine by implementing an iterative approach to improve the efficiency of multilateral well placement optimization. The method divided the original problem into several single well optimizations to speed-up the process and improve results. He also applied a proxy to avoid running numerical simulation if the expected productivity of a certain well was within the range of validity of the proxy. Alghareeb et al. (2009) applied a similar algorithm to optimize ICV settings in a trilateral well in a synthetic model representing a fluvial channel reservoir as well as a real field in the Middle East. Results for the real field optimization showed that water breakthrough was delayed by two years when compared to the current setting. They also studied the effects of a near-well fracture on the optimum results. This study concluded that fractures only affected optimization results if it was far away from a water flood-front.

Aitokhuehi (2004) combined the smart valve setting optimization algorithm from Yeten (2003) with a history matching module. As production measurements were obtained from a reference model, geologic realizations were updated as the simulation

progressed. This procedure revealed that using a single history-matched model did not improve optimal results in some cases due to the nonuniqueness of history matching solutions. Using multiple realizations to history match, and then, to optimize improved results as model uncertainty was reduced. Optimal solutions on the history matched models were between about 80% and 90% of the known geology optimum.

To reduce computational cost associated with running thousands of simulations for optimization, other work concentrated in designing proxies to the reservoir simulator. Pan and Horne (1998) used multivariate interpolation methods such as Least Squares and Kriging as proxies for reservoir simulation. The purpose of the first algorithm is to construct a function that has a simple known form to approximate some objective function. The behavior of this objective function is first observed through a number of simulations. Then, a function is constructed such that it minimizes the sum of the squared residual between data and the function values. To begin the study, several well locations were selected for numerical simulation as a sample to train the proxy. Then, Net Present Value (NPV) surface maps were generated using the two proxies. These maps were subsequently used to estimate objective function values at new points. They observed that the Kriging method provides more accurate means to estimate the objective function than the Least Squares interpolation in the tested examples.

Along the same lines, Onwunalu (2006) implemented a statistical proxy based on cluster analysis to reduce the excessive computational requirements when optimizing under geological uncertainty. Additionally, his work looked at performing optimization of multiple nonconventional wells opened at different times. When simple wells were optimized the proxy provided a close match to the full optimization by simulation only 10% of the cases. This percentage increased to 50% when multiple nonconventional wells were optimized. Other works which addressed optimization under uncertainty include that of Shirangi and Durlofsky (2015). They presented a closed-loop optimization methodology with sample validation. The optimization was conducted using a hybrid particle swarm optimization and local pattern-search algorithm to optimize well controls and locations under uncertainty. It was concluded

that the use of too few realizations can result in lower true-model NPVs, whereas optimization with sample validation provides a systematic approach for determining the proper number of realizations.

Other researchers have approached the same problem from a statistical aspect. Su and Oliver (2010) developed an ensemble-based optimization by generating statistical information created by random perturbations of control variables to estimate the cross variance between the objective function and the control variable. The method was used to optimize controls of two horizontal wells drilled parallel to the water boundary edge. Optimal ICV settings showed a 50% reduction in cumulative water production over one decade. The method was also tested to minimize water production from ten multilateral wells. A reactive control strategy worked better than a defensive strategy (using pressure drop across the ICV as control variable) for this case. Optimum ICV solutions reduced water production by 18% and 5%, for the reactive and defensive approach, respectively.

Other studies have elected to take a more practical approach by modifying optimum control settings based on well responses. Alyan et al. (2014) presented a field case study where the flow rate of a trilateral well, each lateral completed with an ICV and a downhole flow meter, was optimized. The study entailed varying the choke setting of each valve between fully open and fully closed. A total of 18 combinations between the three valves were tested. Results from downhole flow meters were in close agreement to the surface flow meter in 95% of the cases for this two-phase flow well. The ICV combination with the highest oil flow and lowest water flow was declared as optimal and was set for the well.

While all previous studies used production rates as input for the optimization algorithm, others sought alternative measurements for the problem. For example, Li (2010) used early time distributed temperature feedback data to estimate permeability. With the assumption that a user does not have access to a geologic model, he proceeded by choking ICVs that show higher temperature than neighboring valves until a uniform temperature profile (which implies a more uniform flow) is achieved. The procedure was implemented manually with no optimization algorithm. Although

such an approach does not necessarily maximize production, it achieved higher long-term recovery in most studied cases. He also applied the method on a smart well and proposed to modify ICV settings based on temperature feedback. In another study, Ijioma and Jackson (2014) used self-potential measurements to optimize well production. Self-potential measurements can be correlated to waterfront encroachment that is hundreds of meters away from the well of interest. The methodology present an advantage in defensive water production minimization approaches.

1.3 Research Objectives

The literature review shows apparent gaps in a number of areas. For example, the performance of most flow profiling studies was not adequate in three-phase flow cases. One proposed method is to use a pressure differential measurement across the zone of interest (choke) to address this issue. However, this would introduce a flow obstruction in the wellbore and cannot be obtained in a distributed manner along a horizontal wellbore given the current state of the technology (Ünalmiş and Trehan, 2013). Moreover, all studies have analyzed either acoustic or temperature measurements individually although the same fiber line is capable of obtaining both measurement types simultaneously by installing additional surface equipment (Johannessen et al., 2012). Cointerpretation of temperature and acoustic measurements presents an opportunity for the three-phase flow problem.

Another application that is lacking in the literature is translating the information from downhole measurements into palpable production gains. Rather, it is common to use the measurements for planning and allocation purposes only. If a well is completed with ICVs and DTS/DAS, a huge amount of data is at our disposal. A great advantage of such completions is that an immediate feedback about the action we take is available to us. When sensory and control capabilities are available, there is also a need for an analysis engine that takes input from the sensors, assists in decision making, and outputs flow changes to be made using the valves. By doing so, we are closing the advanced completion loop of flow control, measurement, and

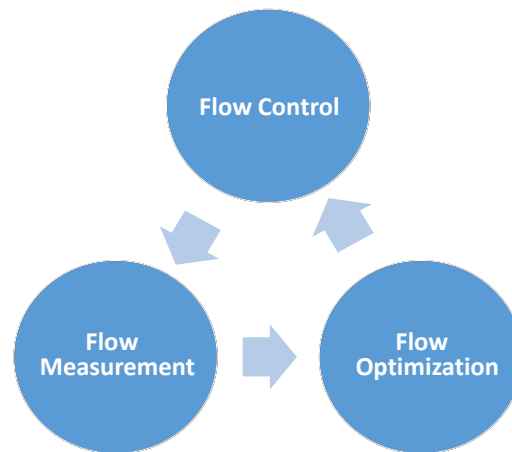


Figure 1.7: Closed-loop approach to achieve continuous flow measurement, control and optimization.

optimization (Figure 1.7). This cycle can continue until a well setting is optimized.

Closing this optimization cycle is partly enabled by downhole measurements. Most current optimization studies rely on surface flow rates to evaluate different flow scenarios, which neglects the contribution of individual flow segments. For example, it is not uncommon for operators to test the well’s production by shutting one zone at a time to determine the source of water production. The transition to downhole flow rates provided by distributed downhole measurements addresses this issue by determining in-situ flow rates. Ünalmsis and Trehan (2012) summarized other advantages that can be realized from continuous downhole measurements as:

- Allocating zonal and commingled production.
- Identifying production anomalies as soon as they arise.
- Estimating the productivity index as measurements are taken in flowing and shut-in conditions.
- Reducing surface well test requirements, which is especially crucial offshore.

Taking all of that into account, the key research objectives for this work were:

1. Develop an algorithm to solve for downhole two-phase flow rate using acoustic measurements. The algorithm would serve as a foundation for subsequent research steps. Once established, the algorithm would be used on data sets with

- different flow conditions to test its rigor.
2. Investigate potential improvements to the inflow profiling problem by analyzing temperature and acoustic data simultaneously. The main limitation in using DAS for three-phase flow is that there is one more unknown than the number of available equations. With temperature measurements, an additional equation based on the definition of enthalpy and Joule-Thomson coefficient is available.
 3. Investigate an optimization process that takes into account downhole flow rates and processed information from the previous steps. Calculated downhole flow rates from DAS and DTS in the previous steps would be the optimization input and smart well controls that maximize recovery or NPV are the output. Different optimization approaches are to be evaluated for this purpose. These include statistical data-driven methods that give preference to scenarios with positive historical outcomes. Another approach considers existing geological information by using a reservoir simulation realization for optimization.

The integrated workflow of this research is illustrated in Figure 1.8. After collecting DAS and DTS data, we started by estimating the flow velocity and fluid phase fractions that yield the corresponding temperature and acoustic response at that time and distance. Assuming that we have an uncertain forward simulation model, a history matching procedure was performed to update model permeabilities to match measured production rates. Then, an optimization algorithm was applied to the updated simulation model to find the settings of inflow control valves that optimize a defined objective function. When optimum valve settings are applied to the well, a change in downhole flow conditions is provoked and new DAS and DTS data are collected. From a production optimization point of view, the procedure would be repeated until no further increase in production is obtained. At that point, more valve settings should be tested if the actual well performance is still not matching the simulation model. The convergence criterion is either reaching a predetermined number of iterations or achieving an optimum solution while matching the simulation model.

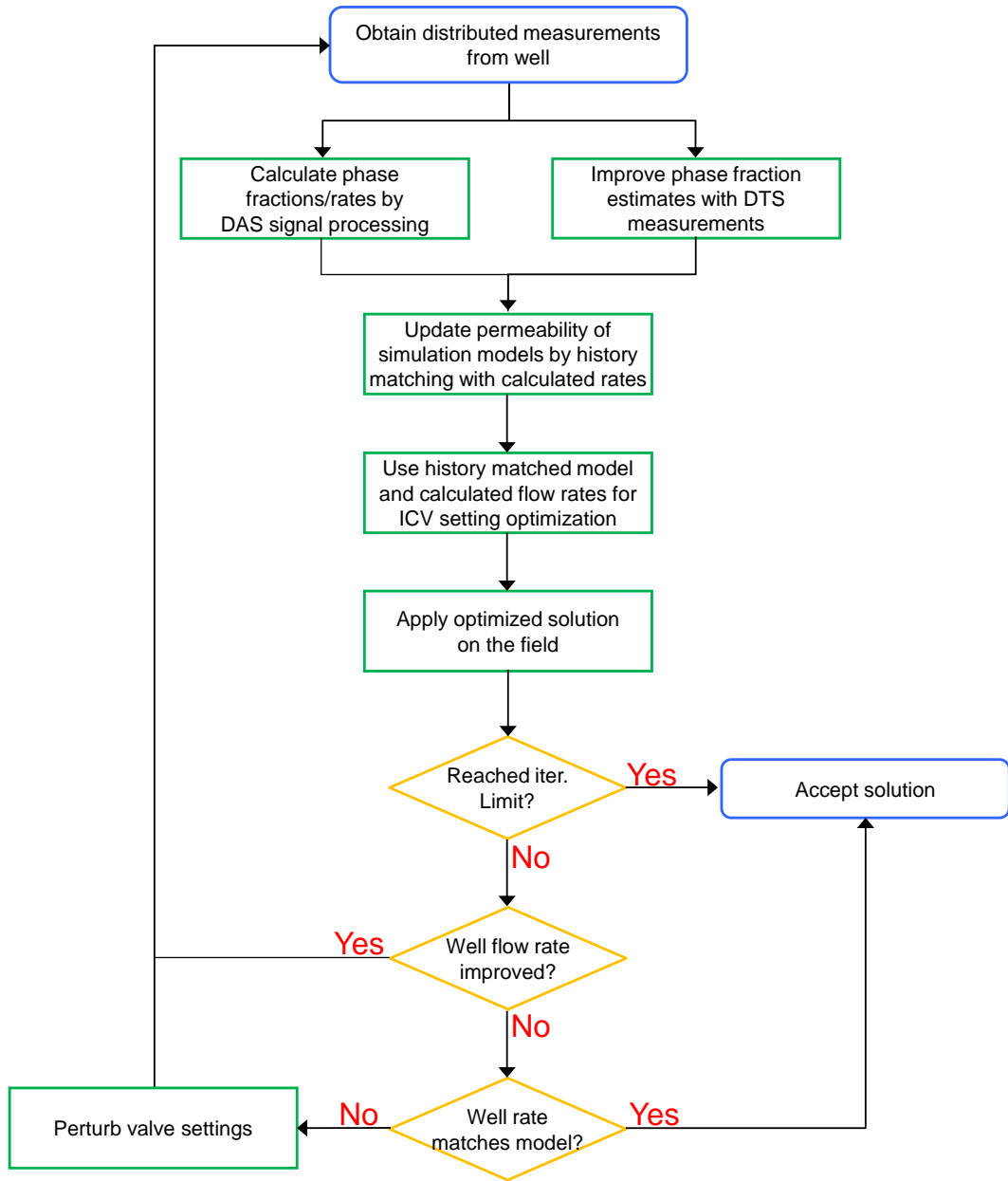


Figure 1.8: Flowchart for the overall integrated procedure.

1.4 Dissertation Outline

This dissertation proceeds as follows. In Chapter 2, we detail the application of different signal processing techniques to the acoustic measurements generated across the inflow devices and propagating along the wellbore tubing. The derivation of fluid flow rate and in-situ fraction as a function of the medium speed of sound is presented. Several examples are discussed, including the analysis of acoustic data collected in an experimental setup, DAS data from a single-phase oil producer, and DAS data from an oil producer cutting some water.

Chapter 3 introduces an equation of state approach to correlate the Joule-Thomson coefficient, which is interpreted from DTS data, to the fluid phase fractions. We explain how integrating results from temperature data into the acoustic data analysis improves the inflow profiling process, especially for three-phase flow. Several synthetic examples are discussed to support these findings.

Then, Chapter 4 presents example applications of using the information discussed in the previous two chapters. The main application is how the measured downhole flow rates are used as a basis for the smart well control optimization problem. The optimization algorithm is explained in detail here. Another application discusses improvements obtained from history matching a reservoir simulation model using downhole flow rates compared to the conventional method of history matching with surface flow rates.

Results from the procedure described in Chapter 2 along with some of the production optimization results presented in Chapter 4 have been published in Bukhamsin and Horne (2014). The improved results attained by adding temperature to the inflow profiling analysis Chapter 3 have been published in Bukhamsin and Horne (2016).

Finally, Chapter 5 summarizes the conclusions of this work and gives suggestions for future work. These recommendations include improving the integration of the optimization framework, introducing data mining into the analysis, and developing a wellbore mechanistic flow model based on downhole flow measurements.

Chapter 2

Inflow Profiling With Distributed Acoustic Sensing

In the early stages of this work, we attempted to construct a forward model to predict the acoustic response given the flow rate and other flow conditions. With an accurate forward model, it is possible to formulate an inverse problem to obtain the flow rate from a given acoustic response in a similar manner to existing temperature inverse models. A classical work in acoustic modeling was conducted by Mckinley et al. (1972), based on the rate of dissipation of mechanical energy into turbulence. After simplification, the correlation is expressed as:

$$q \propto \left(\frac{a A^2}{K_D \rho} \right)^{1/3}, \quad (2.1)$$

where q is the flow rate (m^3/s), a is the acoustic amplitude (volt or $kg \cdot m^2/(s^3 A)$), A is the pipe cross-sectional area (m^2), K_D is the drag coefficient, and ρ is the fluid density (kg/m^3).

One issue with this equation is that it assumes single-phase and very low flow rates. Currently, this equation is actually used to quantify fluid flow behind casing or through leaks in noise logging. It was also found that the relationship is extremely

dependent on the geometry of the tubulars. For example, it is very challenging to attribute noise sources of mixed fluids through perforations of varying sizes (Kashikar, 2012; Mckinley et al., 1972). For that reason, the research focus was placed on making direct flow measurement from DAS data in favor of modeling acoustic behavior associated with the flow.

This chapter begins by giving an overview of DAS data in its raw form and how it is handled and visualized. Then, the signal processing techniques involved in inferring flow information from acoustic data are presented. Interpreting flow properties starts by estimating the speed of sound within the fluid medium from the acoustic measurement; then, calculates fluid phase fractions. An approach to use the speed of sound to estimate the fluid flow velocity is also explained. Figure 2.1 depicts the overall procedure starting from loading the data until a flow rate profile is obtained. The specific process used to achieve each step is given inside the arrows. A number of examples that demonstrate these steps are given at the end of the chapter. It should be noted that while some of the described techniques have been applied recently in the petroleum industry, minimal theoretical details were revealed in those studies.

2.1 Raw Acoustic Data Preprocessing

Unprocessed acoustic data files are stored as matrices that contain values of the acoustic power in decibels (dB) with a time stamp on one axis and a distance indicator on the other. For our particular application, it is expected that a high-pressure fluid passing through a valve or a perforation would generate a high frequency acoustic energy. To be able to capture acoustic characteristics at this frequency range, it is required to collect DAS data at a very high temporal sampling rate (usually in the range of 5,000-25,000 samples/second for fluid flow analysis). Moreover, a low spatial resolution is desired to achieve true distributed flow profiles, which results in high spatial sampling rate. This leads to very large data files collected from the DAS system.

Consider a typical 6,000 ft horizontal well as an example. Sampling the well at

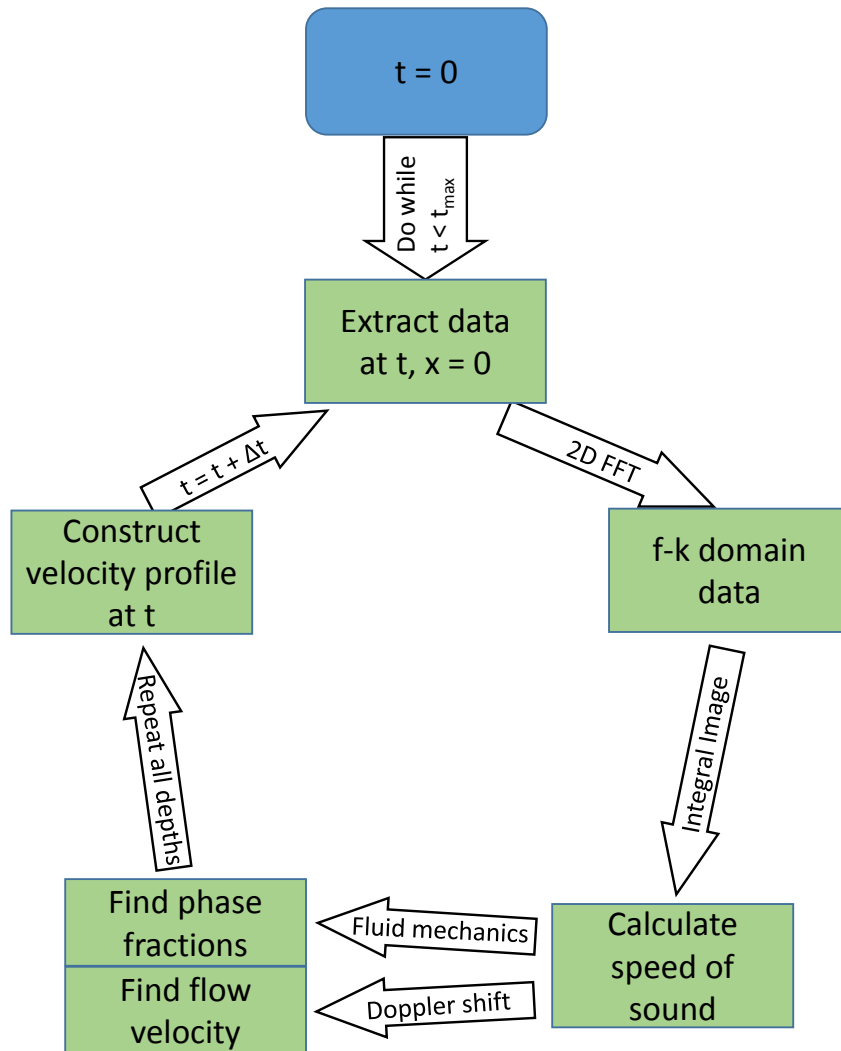


Figure 2.1: Procedure of calculating flow velocity and phase fractions using DAS data.

10 kHz every 1.5 ft, results in collecting 40 million samples per second. Assuming these data are saved as a standard text file with an average four-digit value per sample, the file size would grow by 160 MB per second or 9.6 GB of data per minute. Handling, opening, and viewing these large data files is a challenge by itself. Figure 2.2 shows a juxtaposition of five-second segments of raw acoustic data collected from one of the analyzed wells. With the exception of high noise levels against each ICV in the well (represented by red lines to the right end of the figure), minimal conclusions can be drawn from such a plot. Some vertical lines can also be observed during the test at times corresponding to surface disturbances. By transforming the data to the frequency-wavenumber (f - k) domain, it is possible to detect the propagation of acoustic energy and the frequency-dependent attenuation of that energy with distance.

In most cases, a file containing one minute of acoustic data could not be loaded with available computing resources. To overcome the challenge of handling large data files, we divided the raw data into a series of blocks for processing. The size of the block ($N_x \times N_t$) depends on the desired spatial and temporal resolution for calculated velocity profiles. For the next block, the window was moved by N_t time samples and $N_x/2$ spatial samples. Halving the spatial window size is performed to enhance repeatability and to increase spatial resolution in the results (Xiao et al., 2014). The end result are a set of f - k plots overlapping in distance and covering the entire file content as shown in Figure 2.3, with a velocity and volumetric phase fraction calculation from each block.

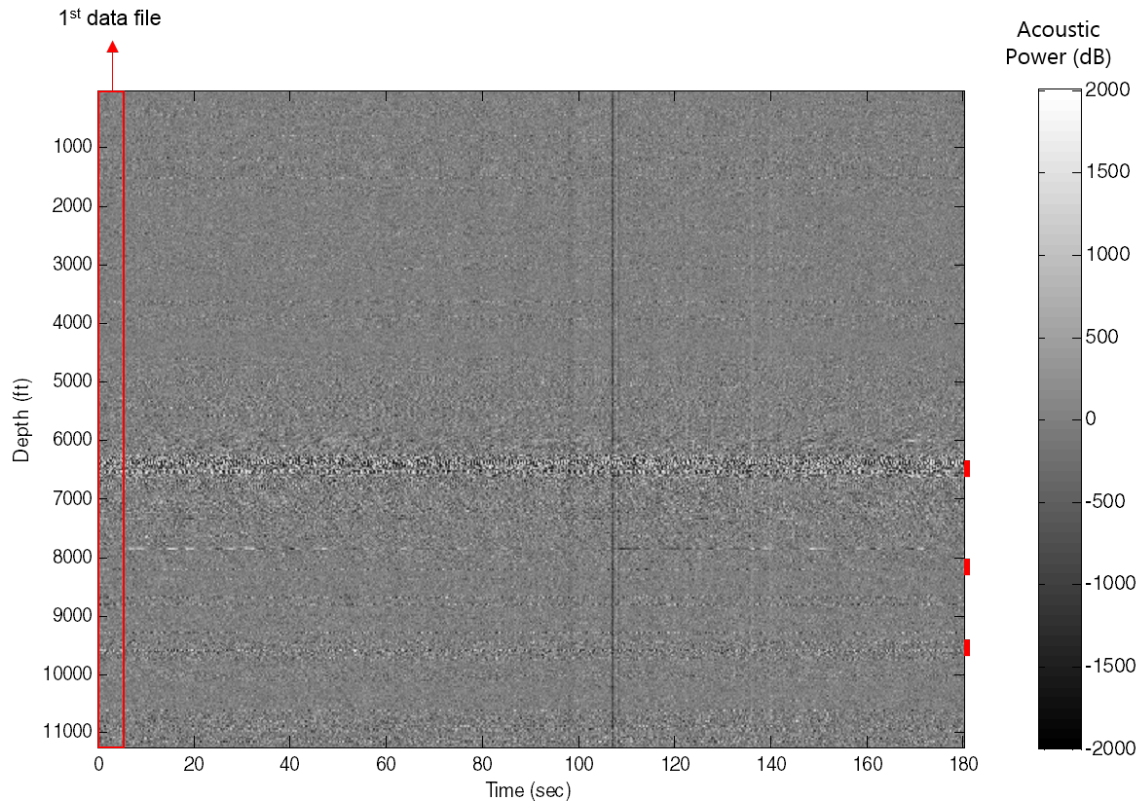


Figure 2.2: Example of raw acoustic data collected from a multilateral well. High noise levels are observed against the ICVs, which are represented by red lines at the right end of the figure. The original high-resolution image contains 12 gigapixels. This image was constructed by extracting five seconds of data at a time (800 MB).

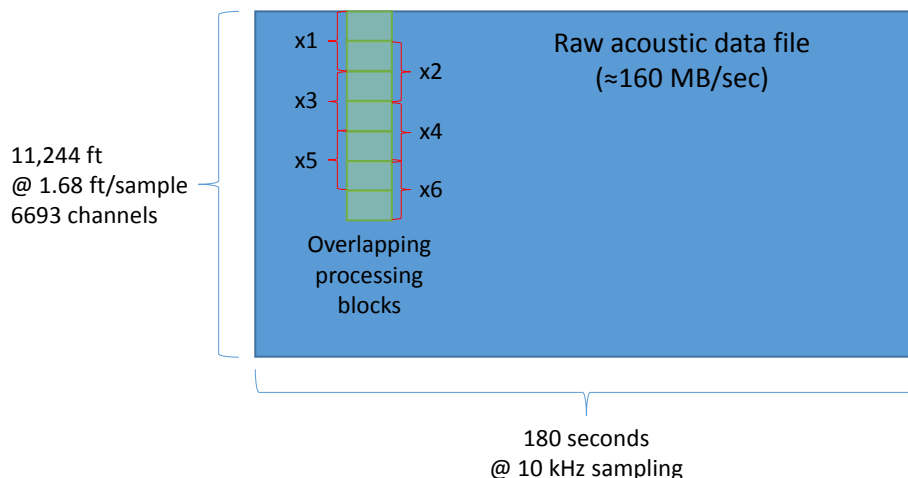


Figure 2.3: Parsing the raw data into different blocks for processing. Each subsequent block includes half the spatial samples from the previous block to increase spatial resolution of the results. Each processed block results in a velocity and phase fraction reading at that location in that instance of time.

2.2 Transforming Acoustic Data to the f - k Domain

When a propagating acoustic wave is measured in both the time and space domains, it is possible to transform these data to the f - k space. Analyzing a time-dependent signal with the Fourier transform provides the frequency content of the data (units of s^{-1} or Hz). Similarly, analyzing a space-dependent signal gives spatial frequency or wavenumber information (units of ft^{-1}). As such, it is possible to construct an f - k plot by feeding the data to a two-dimensional Fourier transform algorithm. This type of operation is capable of revealing aspects of data that are not easily detected in the time-space domain like trends, discontinuities, and self-similarity.

Basically, Fourier analysis consists of breaking up a signal into sine waves (referred to as the analyzing function) of various frequencies. In principle, the transform measures similarity between a signal and the analyzing function via an inner product operation between the two. The sine function is represented by complex exponentials

here using Euler's formula (Osgood, 2007). Mathematically, the Fourier transform can be represented as (Rahman, 2011):

$$\mathcal{F}(\xi) = \int_{-\infty}^{\infty} f(t)e^{-2\pi i\xi t} dt, \quad (2.2)$$

where $\mathcal{F}(\xi)$ is the Fourier transform for the transformation variable ξ , which represents frequency. $f(t)$ is the signal in the time domain and i is the imaginary unit $\sqrt{-1}$. $\mathcal{F}(\xi)$, in general, is complex valued because it is obtained by integrating a function times a complex exponential. If a signal contains significant oscillations at an angular frequency $\xi\theta$, the absolute value of $|F(\xi\theta)|$, would be large. By examining a plot of $|F(\xi)|$ vs. ξ , it is possible to determine the frequencies that contain the highest energy in the signal. Because analyzed time signals are discrete, we used the discrete Fourier transform variation, which can be expressed as:

$$F^k = \sum_{n=0}^{N-1} f_n e^{-2\pi i k n / N}, \quad k \in \mathbb{Z}, \quad (2.3)$$

where F^k refers to the k^{th} Fourier coefficient (k belongs to the integers set) resulting from transforming N discrete time-domain measurements, f_n . We applied a Fast Fourier Transform (FFT) algorithm in this study for its computational advantage. Because the signal is real-valued, the values of Fourier coefficients are symmetric around the x-axis and negative frequencies should be ignored (Osgood, 2007).

For our application, the axis of the transformed data are expressed in terms of the original data as:

$$\Delta k = \frac{1}{N_x \Delta x} \quad \text{and} \quad \Delta f = \frac{1}{N_t \Delta t}, \quad (2.4)$$

where k , f , x , and t are used to represent wavenumber, frequency, distance, and time; respectively. The maximum wavenumber and frequency values in the new domain are

given by Nyquist equations as (Osgood, 2007):

$$k_{max} = \frac{1}{2\Delta x} \quad \text{and} \quad f_{max} = \frac{1}{2\Delta t}. \quad (2.5)$$

2.3 The Speed of Sound in Pipe Flow

To determine in-situ phase fractions using acoustic data, it is important to understand the properties of the speed of sound in pipe flow. In this section, we explain how a well completed with ICVs generates acoustic signals that are picked up by DAS. Once we established this understanding, we developed an image-processing technique to track the line of high Fourier coefficients in the f - k plot to calculate a value of the speed of sound in the production fluid based on the integral image value. Then, two-phase fluid mixing rules were applied to find phase fractions given the calculated speed of sound. Finally, we conducted a study of the sensitivity of speed of sound measurement with respect to well conditions.

2.3.1 Mechanism of Acoustic Wave Propagation in Pipe Flow

Because velocity measurements are based on tracking acoustic waves, it is important to understand how these waves are generated. Turbulent pipe flow is inherently associated with self-generating pressure fluctuations (called eddies) that travel with a velocity near the volumetrically-averaged flow velocity (Figure 2.4). However, the acoustic waves generated by these fluctuations operate at a very low frequency and do not always show in DAS data (Silva et al., 2012). Nevertheless, if a well is completed with ICVs, a strong acoustic wave is generated as the fluid is forced through the valve constriction as shown in figure Figure 2.5. The acoustic wave propagates through the fluid in the wellbore in two directions; with the flow and against it. The upgoing (c_u) and downgoing (c_d) speed of sounds can be obtained by tracking these acoustic wave propagation paths.

The dynamic pressure exerted by acoustic waves causes local changes in the radial

strain of the pipe wall. This strain is captured by the optical sensors within the DAS. To understand this process easier, let us assume that only one acoustic wave is tracked. In such a case, the sensors along the wellbore would pick up pressure fluctuations with some time delay as the wave traverses through the fluid (Figure 2.4). The speed of sound is then calculated based on the time of flight and known distances between the sensors (Ünalmiş and Trehan, 2013). Because several superposed signals are picked up, however, these signals are fed into a signal processing algorithm based on a two-dimensional Fourier transform to take the data from a time-distance domain to a frequency-wavenumber domain as we will discuss in the next section.

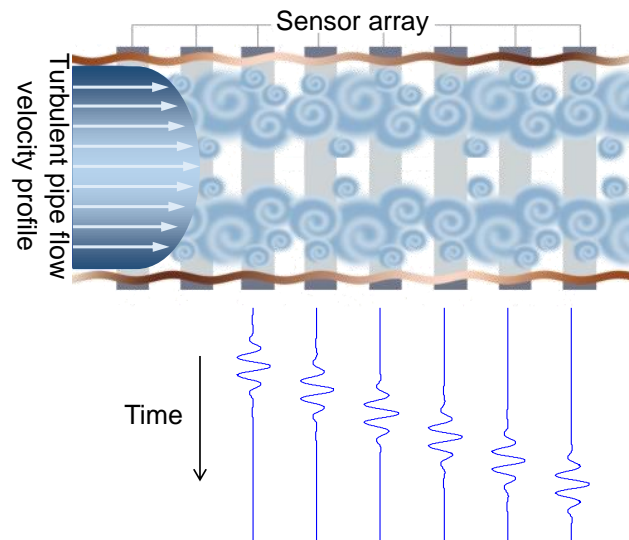


Figure 2.4: A sensor array picking up noises from the eddies as they arrive to the sensor location. Top sketch from Gysling and Loose (2004)

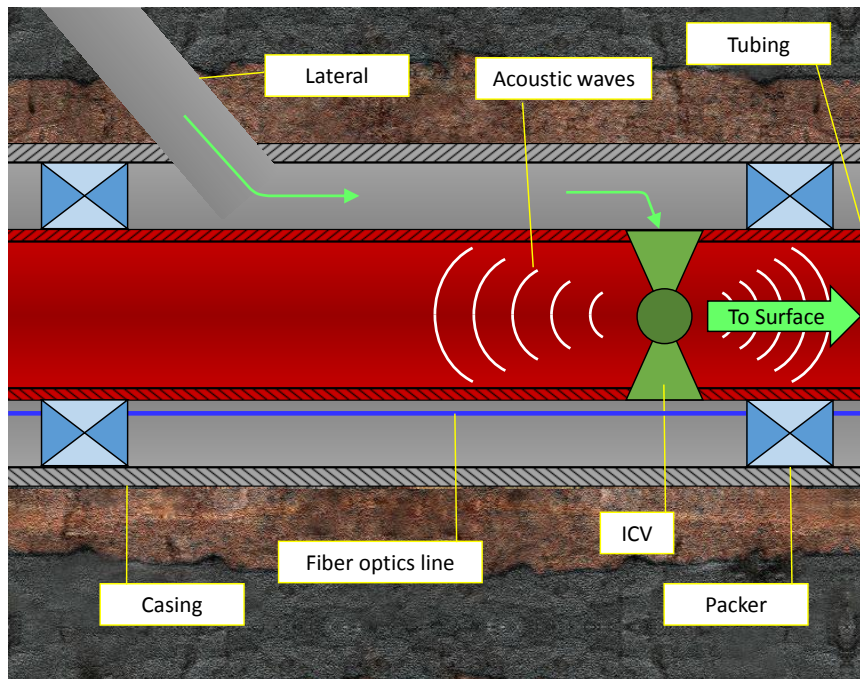


Figure 2.5: Mechanism of generating acoustic waves as the production fluid passes through an ICV.

2.3.2 Measuring the Speed of Sound from the f - k Domain

As DAS measures acoustic amplitude in a nondispersive medium, sound speed is independent of sound frequency; hence, the speeds of energy transport and sound propagation are the same (Dean, 1979). This phenomenon is revealed as a line emanating from the origin in the f - k plot corresponding to the high Fourier coefficients as shown in Figure 2.6. The speed of sound through the medium is equivalent to the slope line in frequency-wavenumber plot because:

$$c_m = \lambda f = \frac{2\pi f}{k} = \frac{f}{\tilde{\nu}}, \quad (2.6)$$

where c_m is the speed of sound in the mixture, λ is the wavelength, k is the angular wavenumber, and $\tilde{\nu}$ is the wavenumber. It is worth mentioning that the described methodology would not work in dispersive media, where the wavelength of the acoustic wave is close to the diameter of the dispersed particle. In such cases, waves of different

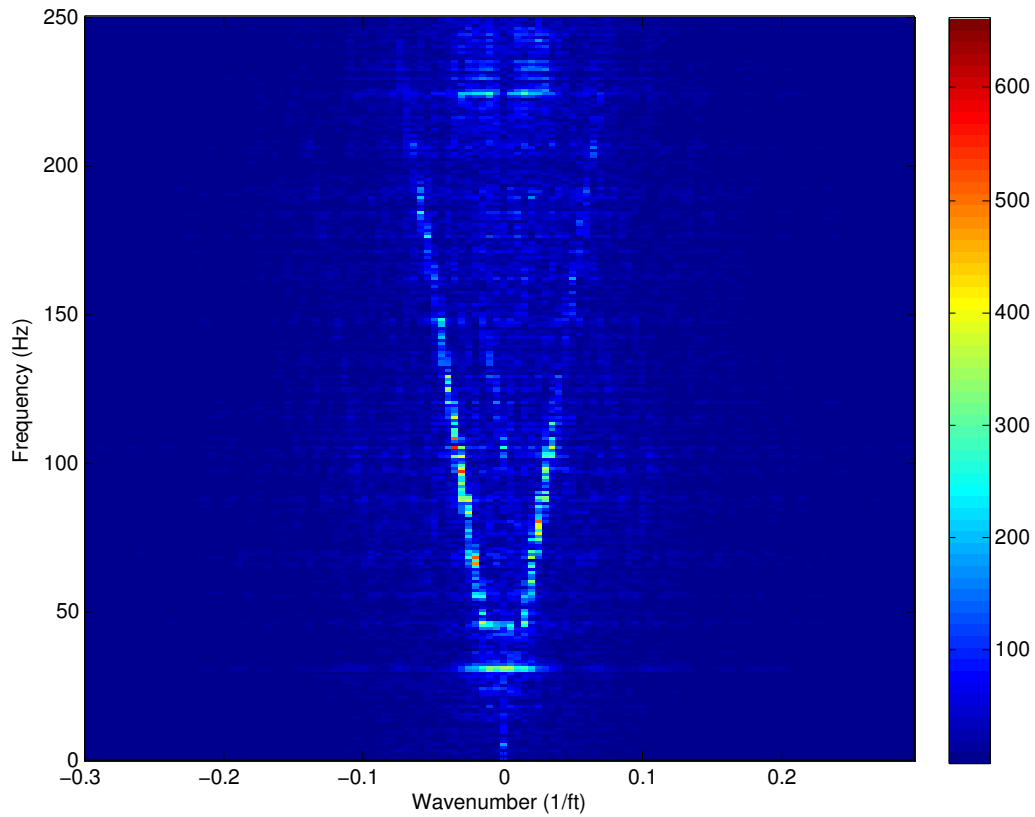


Figure 2.6: A frequency-wavenumber plot shows two distinct lines representing the upgoing (positive slope) and downgoing (negative slope) speed of sounds. Note that we are plotting the wavenumber not the angular wavenumber.

frequencies would travel at different velocities and the f - k plot would show a curved instead of a straight line (Born and Wolf, 1999).

To find the slope in such an image, we employed an image object-detection technique based on the Randon transform, which is explained in detail in Appendix A. The method calculates the integral value through the f - k domain image for a range of slope lines to produce the plot in Figure 2.7, which shows results for tracking upgoing (to the right) and downgoing (to the left) slope lines. Each point in the plot is given by the integral value in Equation (A.1) for that slope value. A slope line passing through high Fourier coefficients returns the highest integral value and is selected as

the most probable speed of sound value.

The width of the distribution around the highest value indicates our confidence in calculated speed of sound values. A slope line that is clearly visible would have an integral value that is much higher than other slope lines causing the distribution to be narrow and the spread between the maximum and minimum integral values to be high. On the other hand, if the acoustic energy is not very strong; the speed of sound slope line might not be easily detectable as the integral value becomes less sensitive to small changes in the slope line values. This phenomenon is demonstrated in Figure 2.8, which shows two cases with high and low confidence in the results. To quantify uncertainty associated with each speed of sound reading, the integral values are normalized (y-axis on the plot). Then, a line is drawn arbitrarily on the 0.95 value and values where this line intersects the distribution are recorded to measure the distribution spread near the highest value. These two intersection points designate the confidence range of the speed of sound measurement. As shown in the lower part of the plot, narrower distributions indicate higher measurement precision as they correspond to a clear line in the f - k domain.

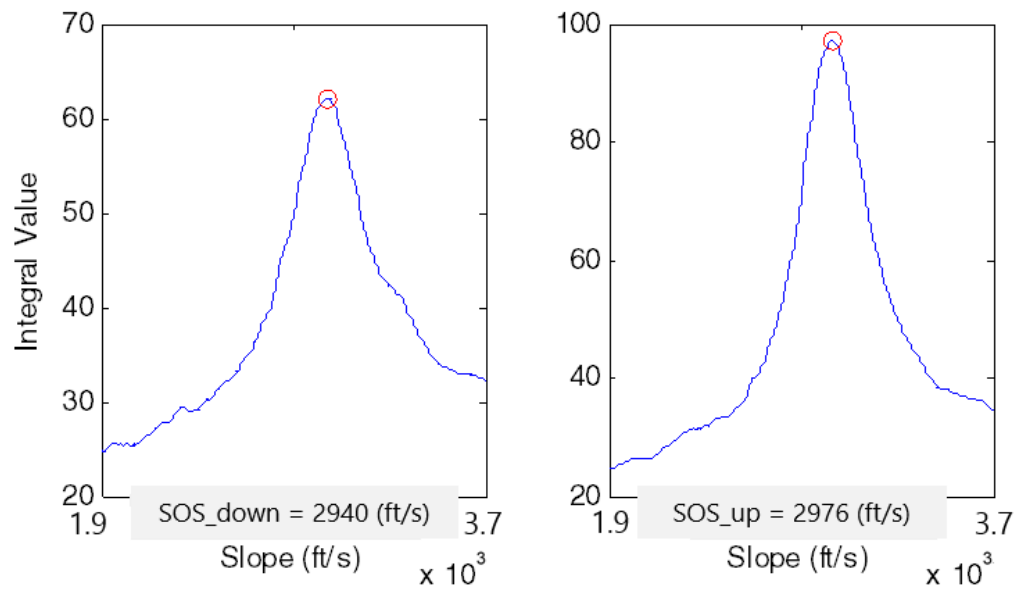


Figure 2.7: Image integral values for a range of possible slopes for the downgoing (left) and upgoing (right) speed of sounds. The most probable value is shown in red.

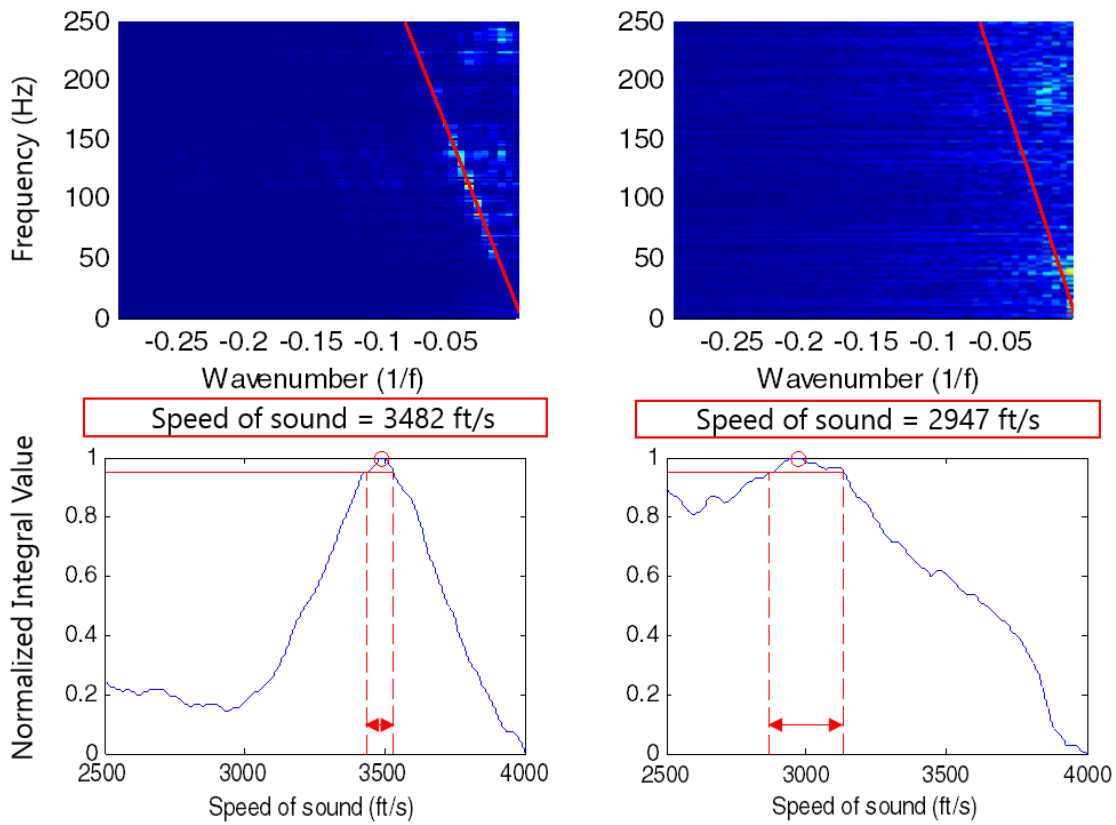


Figure 2.8: Comparing the integral value behavior when the speed of sound line is clear in the image (left) with a case where the speed of sound (in ft/s) is not clear (right). This is reflected in the lower plots with narrow confidence interval in the left plot and a wide one for the right plot.

2.3.3 Fluid Mixing Model for Phase Fraction Calculation

The next step in characterizing the flow using the speed of sound is to convert these measurements to phase fraction information. The procedure follows the two-phase model shown in the work of Chaudhuri et al. (2012). An extended model for three-phase flow is presented in the next chapter. The procedure starts from the definition of speed of sound given by the Newton-Laplace equation (Wood, 1941):

$$c_m = \sqrt{\frac{K_t}{\rho_m}}, \quad (2.7)$$

where ρ_m is the mixture density and K_t is the total bulk modulus of the fluid mixture and the pipe. The total bulk modulus and mixture density are determined by the mixing equations of these two properties. Assuming a homogeneous oil-water mixture, density averages arithmetically as:

$$\rho_m = \alpha_o \rho_o + (1 - \alpha_o) \rho_w, \quad (2.8)$$

while the bulk modulus of the fluid mixture is given by the harmonic average using Reuss approximation (Mavko and Mukerji, 1998) as:

$$K_t = \left[\frac{\alpha_o}{K_o} + \frac{(1 - \alpha_o)}{K_w} + \frac{d}{Et} \right]^{-1}. \quad (2.9)$$

To account for the flow conduit distensibility, the last term in Equation (2.9) includes the diameter of the pipe, d ; pipe wall thickness, t ; and the pipe material Young's modulus, E (Johansen et al., 2011). At this point, we substitute Equations (2.8) and (2.9) into Equation (2.7) and express oil and water moduli in terms of speed of sound and density as $K_o = c_o^2 \rho_o$ and $K_w = c_w^2 \rho_w$. After rearranging the equation, we obtain:

$$c_m = \left\{ [\alpha_o \rho_o + (1 - \alpha_o) \rho_w] \left[\frac{\alpha_o}{\rho_o c_o^2} + \frac{(1 - \alpha_o)}{\rho_w c_w^2} + \frac{d}{Et} \right] \right\}^{-\frac{1}{2}}. \quad (2.10)$$

The left-hand side of this equation is obtained by processing the acoustic signal as described previously. All properties in the right-hand side of the equation are individual phase properties. Phase densities can be obtained in the lab with PVT analysis while methods to obtain phase speed of sounds will be discussed in the following section. All of these properties are to be evaluated at the wellbore pressure and temperature, which can be obtained from DTS and ICV sensors, at that depth and time. The only unknown remaining in the equation is α_o . Equation (2.10) is manipulated to form a quadratic equation in the format $A\alpha_o^2 + B\alpha_o + C = 0$ with coefficients defined as:

$$\begin{aligned} A &= \left(\frac{1}{c_o^2} - \frac{\rho_o}{\rho_w c_w^2} \right) \left(1 - \frac{\rho_w}{\rho_o} \right) \\ B &= \frac{\rho_o}{\rho_w c_w^2} + \frac{\rho_w^2}{\rho_o^2 c_o^2} - \frac{2}{c_w^2} + \frac{\rho_o d}{Et} - \frac{d}{Et} \\ C &= \frac{1}{c_w^2} - \frac{1}{c_m^2} + \frac{\rho_w d}{Et} \end{aligned} \quad . \quad (2.11)$$

Solving this quadratic equation yields two roots given by:

$$\alpha_o = \frac{-B \pm \sqrt{B^2 - 4AC}}{2A}. \quad (2.12)$$

The major assumption in this derivation is that the flow regime is homogeneous, which comes from the way we define mixture density and bulk modulus in Equations (2.8) and (2.9). The example presented in Section 2.5.3 addresses how this limitation affects results. The model also assumes that individual components have distinct speed of sounds within the temperature range of the measurement and that multiple scattering effects of the sound fields are negligible. Another assumption is that the wavelength of the acoustic wave is longer than the pipe diameter and much longer than the characteristic size of the dispersed particles (nondispersive media). For the analyzed examples, the wavelength was about 20 ft ($\lambda = 1/\tilde{\nu}$), which satisfies these conditions. The other assumptions are reasonable for the cases analyzed.

Next, we show a solution of these equations for a typical fluid mixture in the tested

Table 2.1: Fluid properties used to solve the two-phase fraction model.

Property		Water	Oil	Gas
Density,	ρ (kg/m^3)	1100	820	100
Speed of sound,	c (m/s)	1525	1050	500
Bulk modulus,	K (GPa)	2.56	0.905	2.50×10^{-2}

wells. Figure 2.9 shows a plot of the resulting mixture speed of sound as a function of two-phase fluid fraction for the fluid properties listed in Table 2.1. It is noted here that for each speed of sound measurement, a unique phase fraction can be determined for an oil-water flow. However, this is not the case when gas is present as there are two possible phase fraction solutions for each speed of sound measurement between about 300 and 500 m/s for this particular mixture. Interestingly, when gas is present, the lowest mixture speed of sound of around 300 m/s is even lower than the speed of sound in single-phase gas. This is because, as more gas is added to an oil fluid, the rate of change in compressibility is much higher than the rate of change in density. For example, if only 5% gas is added to an oil fluid, bulk modulus of the mixture is reduced by almost three times while the density barely changes. This eventually causes a drastic drop in speed of sound when small amounts of gas are added to liquids. Outside the 300-500 m/s speed of sound range, the solution returns one positive and one negative phase fraction root, which is rejected. When two positive roots exist, one would have to apply knowledge of the flow to determine which solution to accept. For example, assuming a speed of sound measurement of 400 m/s was made in an oil-gas mixture (black dotted line in Figure 2.9), the corresponding Gas Volume Fraction (GVF) would be 0.9 if we knew the flow is gas-rich and around 0.2 if we knew the flow is oil-rich.

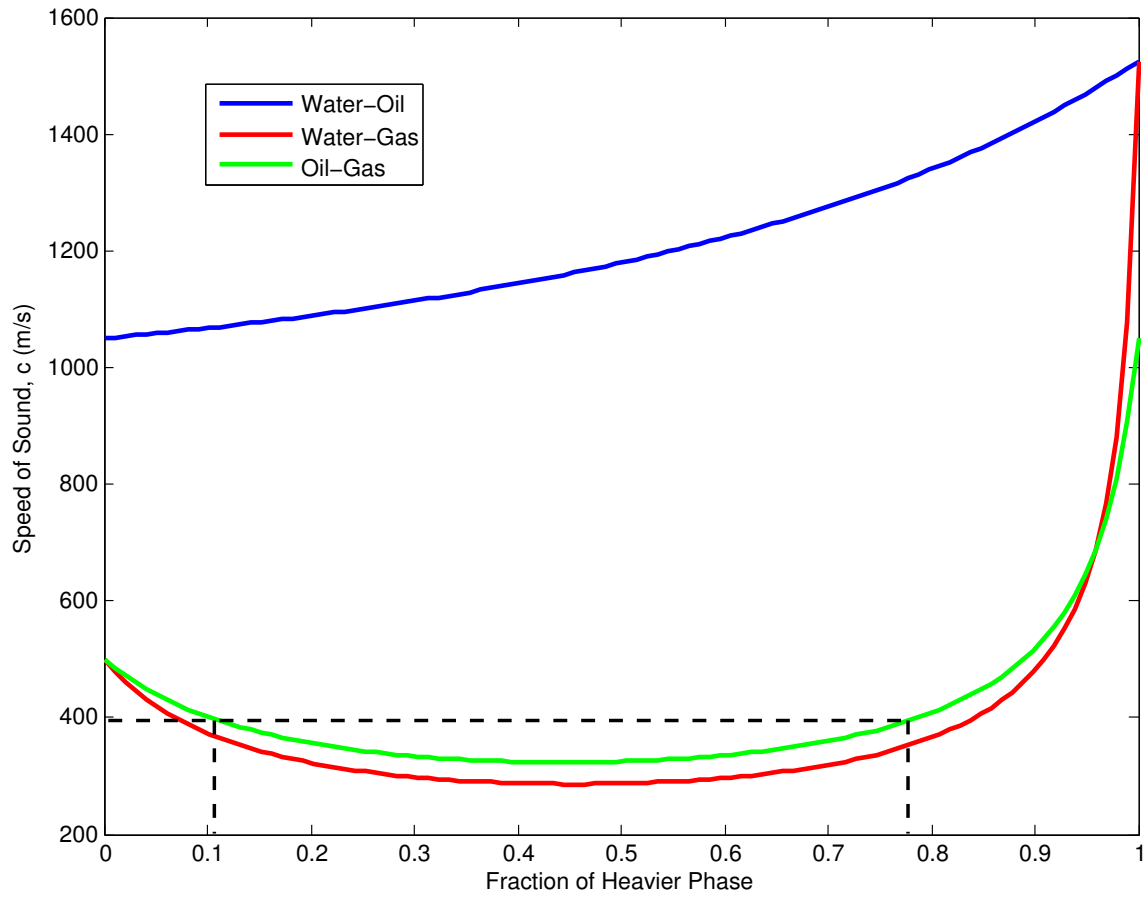


Figure 2.9: Speed of sound as a function of the heavier phase volume fraction for three different fluid mixtures. The black dotted line corresponds to a speed of sound measurement of 400 m/s.

2.3.4 Factors Affecting Single-Phase Speed of Sound Values

The speed of sound is a thermodynamic fluid property that can be derived with knowledge of fluid conditions at any state point. For this type of analysis, the speed of sound in individual phases and in the mixture are needed. Single-phase speed of sound can be determined by expressing it in terms of derivatives of the molar Helmholtz free energy, A ; the temperature, T ; and the molar density ρ as described by Levy et al. (2001):

$$c = \left\{ \frac{\rho}{M} \left[2 \frac{\partial A}{\partial \rho} \Big|_T + \rho \frac{\partial^2 A}{\partial \rho^2} \Big|_T - \rho \frac{\left(\frac{\partial^2 A}{\partial \rho \partial T} \right)^2}{\frac{\partial^2 A}{\partial T^2} \Big|_\rho} \right] \right\}^{\frac{1}{2}}. \quad (2.13)$$

The solution of Equation (2.13) can be plotted as a function of temperature along different isobars as shown in Figure 2.10. Obtained solutions show that the speed of sound is a strong function of temperature and pressure so it is essential to determine the flow conditions to obtain the corresponding speed of sound. Although this expression provides an exact analytical solution, it often cannot be generalized; the Helmholtz free energy surface (as a function of pressure and temperature) is not sufficiently known for most fluid systems. These surfaces are generally based on empirical correlations of experimental data of the particular fluid. Therefore, it is more common that the speed of sound is measured experimentally using nonintrusive liquid characterization techniques (Levy et al., 2001).

To address this issue, the National Institute of Standards and Technology compiled one of the most extensive sets of experimental data, which was made available online by Lemmon et al. (2016). Chaudhuri et al. (2012) used these data sets and conducted additional experiments to correlate the speed of sound of a sample of crude oil and deionized process water with temperature by the following N^{th} -order polynomials:

$$c_o = \sum_{i=0}^N a_o^i T^i \quad \text{and} \quad c_w = \sum_{i=0}^N a_w^i T^i, \quad (2.14)$$

where a_o^i and a_w^i are the calibration coefficients for sound speeds in oil and water listed in Table 2.2. Similar polynomials can be found to fit different fluids by changing the coefficients. The oil and water density was also fit in a similar manner as:

$$\rho_o = \sum_{i=0}^N b_o^i T^i \quad \text{and} \quad \rho_w = \sum_{i=0}^N b_w^i T^i, \quad (2.15)$$

To understand the effects of temperature on calculated single-phase sound speed (and its subsequent effect on our fluid mixing model), we used the Chaudhuri et al. (2012) empirical relationship to find the phase fraction based on mixture speed of sounds at different temperatures as shown in Figure 2.11. Results show that the speeds of sound in oil and water become closer as the temperature is lowered. In other words, the same change in measured mixture speed of sound would lead to higher changes in calculated phase volume fractions at lower temperatures. The speed of sound in oil is more sensitive to temperature changes than that in water.

The example above only demonstrates the sensitivity of speed of sound values to temperature. Batzle and Wang (1992) presented several expressions describing changes in the fluid density and bulk modulus when flow or fluid conditions change. Investigated factors included the pressure, temperature, oil API, molecular weight, solution gas-oil ratio, and the water salinity. The correlations were tested under the pressure and temperature conditions typical of hydrocarbon exploration.

Table 2.2: Calibration coefficients used to find the crude oil and process water properties.

Coefficient	Units	$i = 0$	$i = 1$	$i = 2$	$i = 3$
a_o^i	m/s	1491	-4.088	7.772×10^{-3}	-2.423×10^{-5}
a_w^i	m/s	1432	4.518	-4.539×10^{-2}	1.350×10^{-4}
b_o^i	g/cc	0.9098	-7.374×10^{-4}	6.528×10^{-7}	-2.891×10^{-9}
b_w^i	g/cc	1.017	-5.174×10^{-5}	-5.328×10^{-6}	1.599×10^{-8}

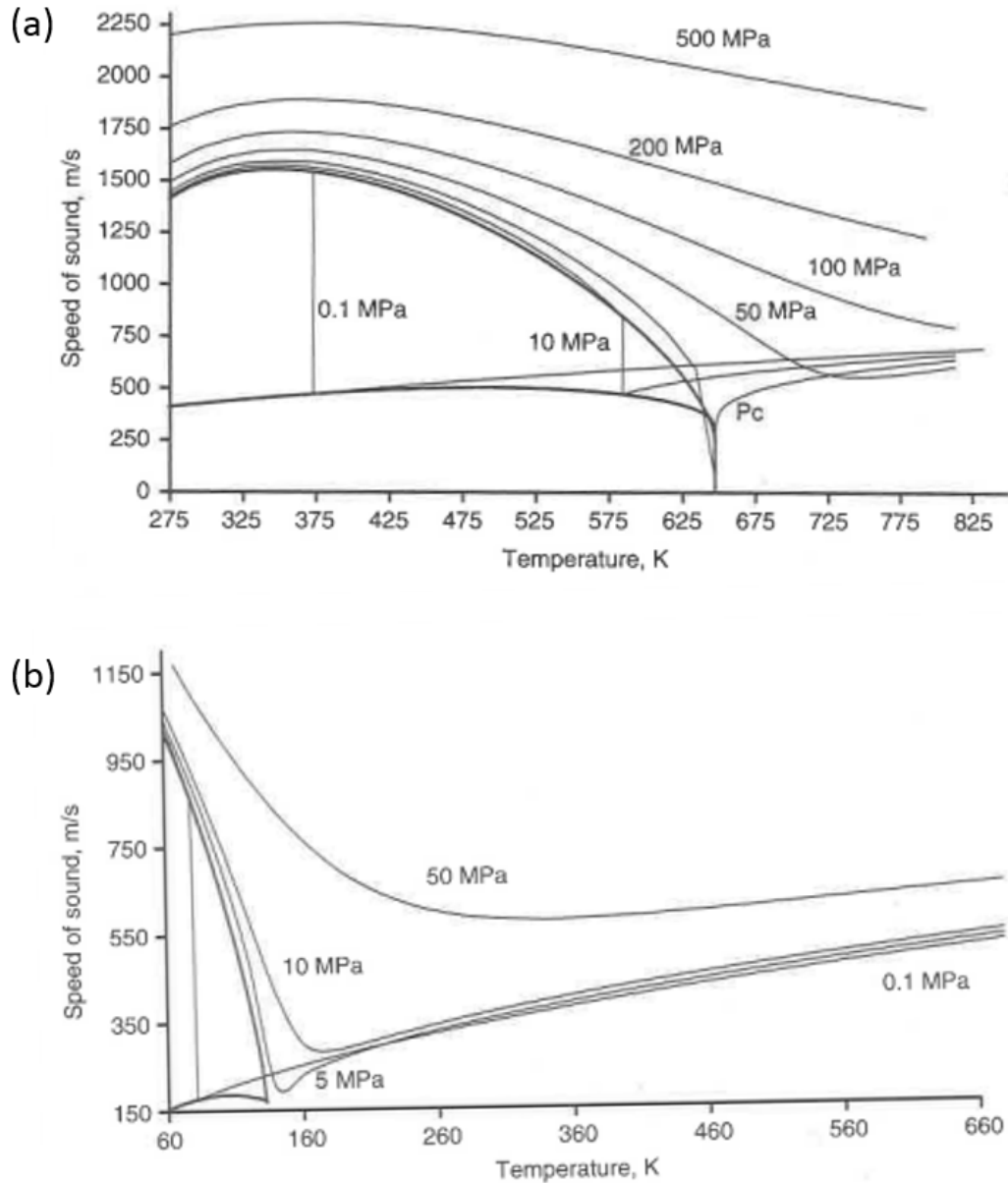


Figure 2.10: The speed of sound in (a) water and (b) air as a function of temperature along isobars. The bold lines represent values on the saturated liquid and vapor curves. Vertical isobars in the top plot represent the region of liquid-vapor phase separations where the thermodynamic speed of sound is not defined for the two-phase system. From Levy et al. (2001).

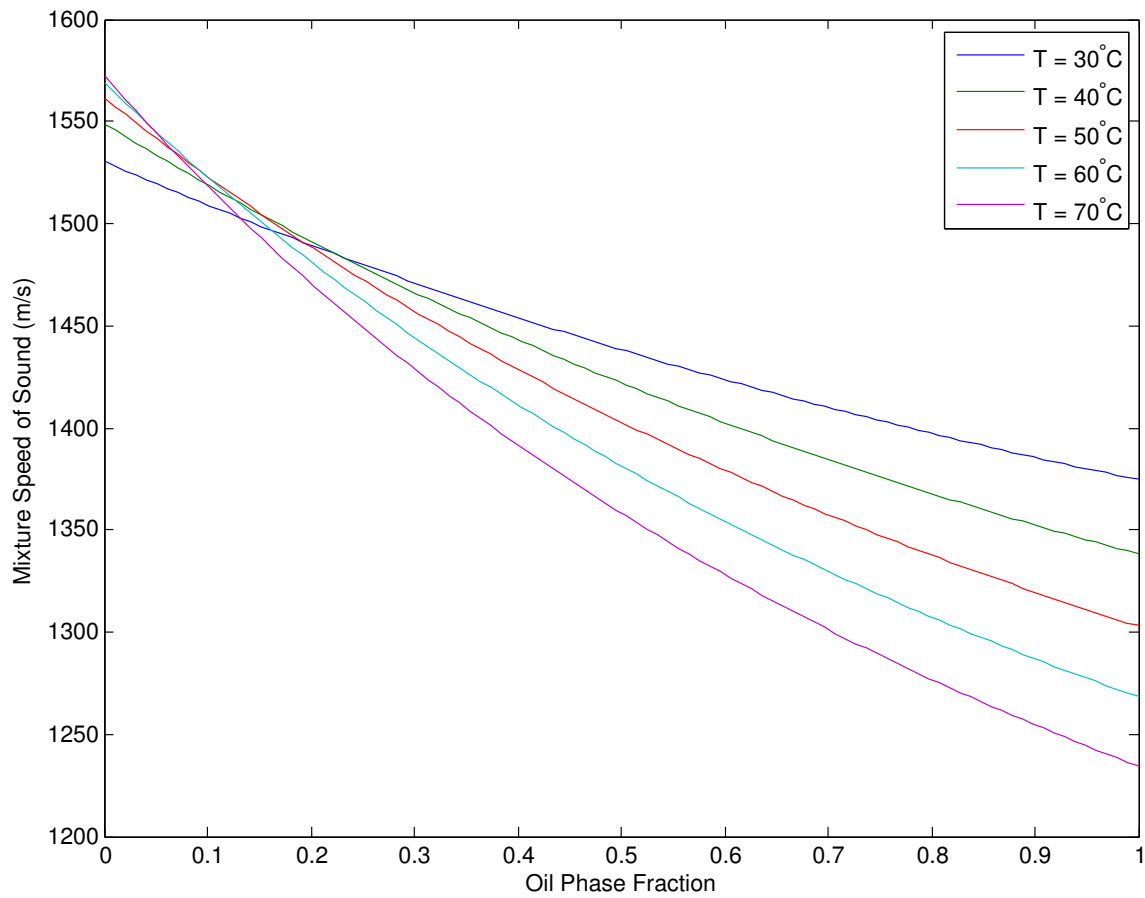


Figure 2.11: Speed of sound in an oil-water mixture with varying oil phase fraction at different temperatures. These solutions were found using Chaudhuri et al. (2012) empirical correlations.

2.4 Flow Velocity Calculation from the Doppler Effect

Once the upgoing (c_u) and downgoing (c_d) sound speeds are obtained from the previous procedure, the Doppler effect principle is used to calculate the flow velocity. When a wave source is moving closer to a stationary point as illustrated in Figure 2.12, the observed frequency at a point ahead of the flow (point 2) is higher than the original wave frequency, f . Point 1, on the other hand, observes a frequency that is lower than the real wave frequency as the sound source is moving away from that point. These two frequencies are expressed as a function of f as (Rosen and Gothard, 2010):

$$f_{obs1} = \frac{c_d}{c_d - v} f \quad \text{and} \quad f_{obs2} = \frac{c_u}{c_u + v} f, \quad (2.16)$$

where v is the fluid velocity. We also know that both observations are made from the original wave with the same wavelength:

$$\lambda = \frac{c_m}{f} = \frac{c_d}{f_{obs1}} = \frac{c_u}{f_{obs2}}. \quad (2.17)$$

This equation can be substituted in Equation (2.16) to obtain explicit expressions for the fluid flow velocity and the static speed of sound in the mixture as:

$$v_m = \frac{1}{2}(c_u - c_d) \quad \text{and} \quad c_m = \frac{1}{2}(c_u + c_d). \quad (2.18)$$

Note that this static speed of sound, c_m , is the value used in Equation (2.10) for phase fraction calculation. The flow rate is calculated by multiplying the mixture fluid flow velocity, v_m , by the cross-sectional area of the pipe.

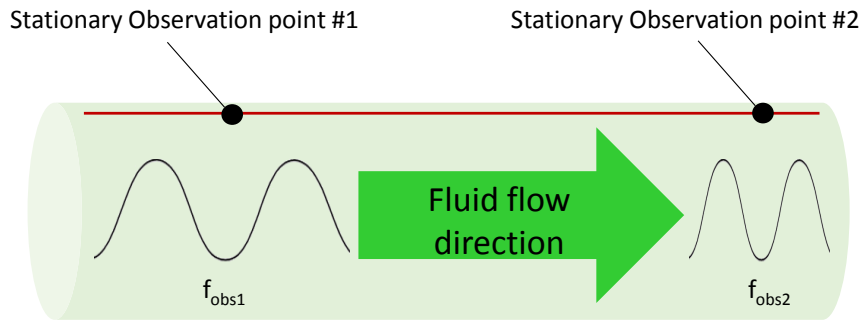


Figure 2.12: Effect of the Doppler shift on frequency observed by two sensors along the flow direction.

2.5 Results and Discussion

In this section, the signal analysis procedure is demonstrated through a number of examples. The first example is implemented on an acoustic data set that was made available online by the MIT Computer Science and Artificial Intelligence Laboratory (Weinstein et al., 2016). After that, we show two DAS analysis examples from real wells. For the real cases, we will present cases where the algorithm was applied successfully to obtain flow rate measurement. For cases that did not perform as expected, we provide an explanation of possible sources of failure to understand the limitation of the technology.

2.5.1 Analysis of Experimental Acoustic Data in Ambient Air

Although this experiment was designed originally to show the effects of beamforming on enhancing the ability to track a moving sound sources, it can also be used for the objective at hand. The data were collected with an array of sensors that were aligned in a two-dimensional plane to measure acoustic amplitude of a speaker that is placed some distance away from the sensors (Figure 2.13). The speaker was emitting a chirp signal, in which the frequency increases with time. Downloaded data included measurements of 1020 sensors that were placed just over an inch apart over two

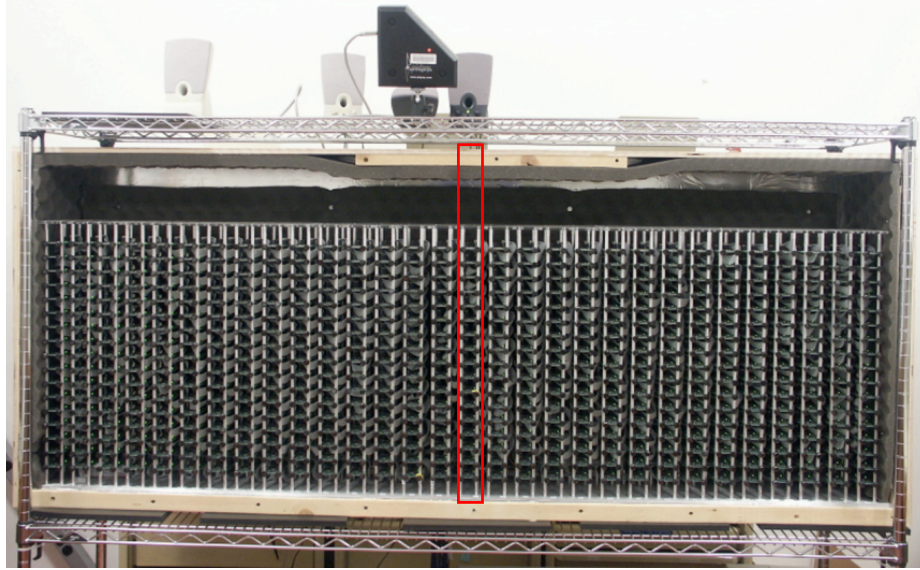


Figure 2.13: Experimental setup with the sensors at the bottom and the speakers at top. The red box encloses sensors that were used for this analysis. From Weinstein et al. (2016)

seconds with a sampling frequency of 16 kHz. Calculating the speed of sound from this experiment is possible by filtering acoustic data from sensors that fall linearly with the sound source as shown by the red box in Figure 2.13. This setup mimics a DAS fiber optic line (series of sensors) that collects acoustic measurement in the tubing from flow generated noises (the speakers).

After transforming the data to the f - k domain, the resulting lines had slopes of 1,187 and 1,184 ft/s for the upgoing and downgoing speed of sound as shown in Figure 2.14. As the experiment was performed in still air, no Doppler effect is expected and upgoing and downgoing sound speeds should be equal. Generated acoustic signals are expected to travel at a speed of sound of about 1,138 ft/s, which corresponds to the speed of sound in air in room pressure and temperature. The difference between calculated and expected speed of sound values is less than 5%. Sources of error might include temperature or pressure variations or additional noises due to equipment vibration. Note that the y-axis sampling frequency (in time) is much finer than the x-axis (in space), which leads to a seemingly elongated grid in

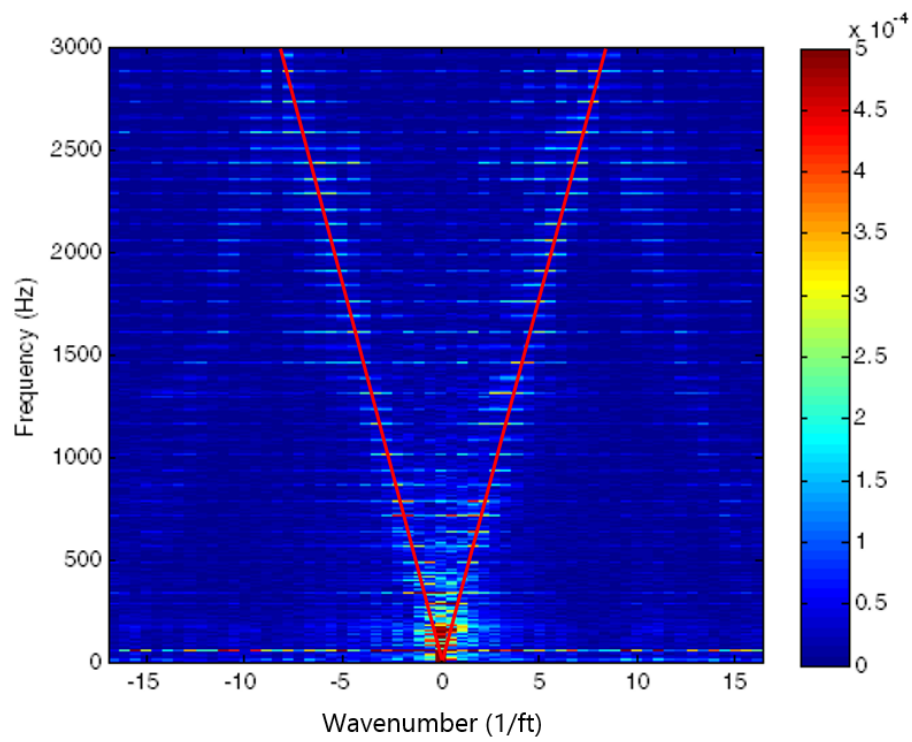


Figure 2.14: Speed of sound line-fitting in the f - k domain for experimental acoustic data in ambient air.

the x-direction.

2.5.2 Analysis of DAS Data in Single-Phase Oil Producer

After looking at the previous simple example, this flow profiling procedure was applied on several data sets collected from a trilateral oil producer in the Middle East. This well will be referred to as Well-A in subsequent discussion. Well-A is producing single-phase oil as it is operating above the bubble point pressure with no water. A sketch of Well-A completion is shown in Figure 2.15. The well has a cased-hole completion with junctions that connect it to two laterals and a main bore (a borehole section drilled out from an existing well). The main bore and laterals were left as open-hole to allow flow from their whole length. Three ICVs were installed in the well to control inflow from each lateral. A close-up of this completion was previously shown in Figure 2.5, which also indicates the fiber line location along the annulus between the tubing and casing.

The three ICVs provide the operator with the capability to run different production scenarios to study the effect of changing an ICV position. Table 2.3 shows the settings for four different production scenarios that were analyzed, where the positions 100%, 50%, and 0% refer to a fully-open, a half-open, and a fully-closed valve. Once a new valve setting had been applied to the well, DAS data were collected for three minutes after the surface flow meter had shown a stabilized flow.

Table 2.3: Interval Control Valve properties for Well-A.

Valve	Distance (ft)	Valve Opening (%)			
		Case 1	Case 2	Case 3	Case 4
ICV 1	6,100	0	50	50	0
ICV 2	8,265	0	0	50	100
ICV 3	9,575	100	100	100	50

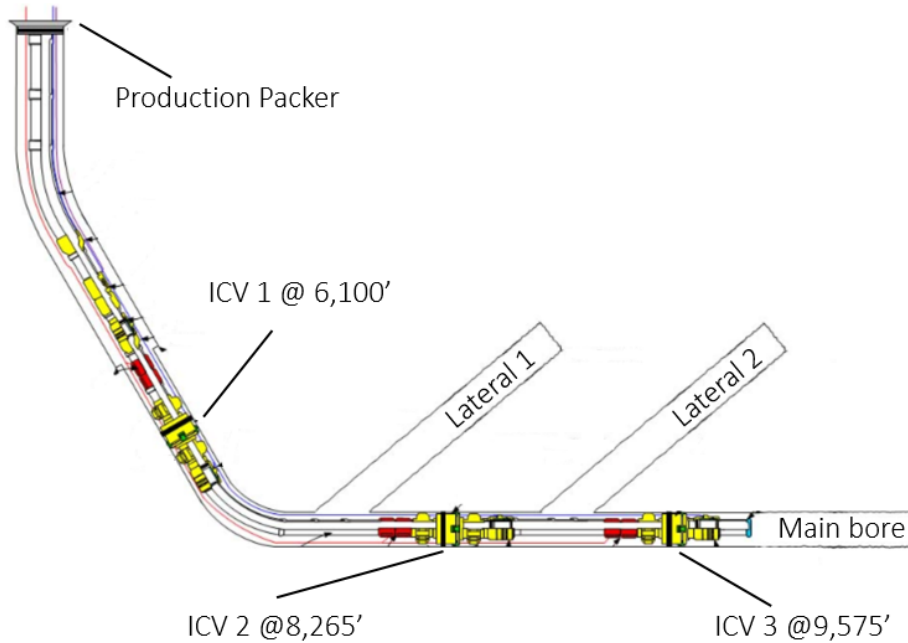


Figure 2.15: Completion sketch for a tri-lateral oil producer with three production segments. From Al-Arnaout et al. (2008).

As a raw data plot is usually not very revealing, we first tried to discern the data content by calculating the root mean square (RMS) value for the time-series along each sensor by:

$$a_{RMS}^k = \sqrt{\frac{1}{N_t} \sum_{n=0}^{N_t} a_n^2}, \quad (2.19)$$

where a contains N_t acoustic time-series measurement along the k^{th} sensor. The results of this calculation are illustrated in Figure 2.16, which shows a clear spike in acoustic power in every instance an ICV is restricted. By contrast, DAS did not pick high acoustic power when the valve was either fully-open or fully-closed in all cases except ICV 3 in Case 2, which showed a small spike against the ICV. This observation actually explains why the first test case, which did not have any restricted valves, did not yield accurate velocity results as shown later. In addition to calculating the RMS, we generated a spectrogram of the data to detect the dominating frequencies for the acoustic signal (Figure 2.17). As dictated by the wave propagation mechanism in

Section 2.3.1, Case 2 in the plot shows that restricting even one ICV is enough to generate detectable noises along the well. These noises are picked up more easily near the restricted ICV in the 300-700 frequency range. This also helps in determining what frequencies to look at in the $f-k$ domain to calculate a speed of sound slope. The spectrogram carries more details than the RMS plot as the latter is effectively an average spectrogram for all frequencies.

As acoustic data had been collected all along the well continuously over time, the data were segmented into several blocks (each containing one second and 320 ft of data) to calculate the speed of sound at that instance in time and at that particular distance. As was described in Figure 2.1, the overall procedure starts from well data collection until we get a flow rate measurement from the well. For each time-distance block, the two-dimensional Fourier transform is applied. Then, we fit the speed of sound line by finding the maximum integral value. The result of each block is inserted into a speed of sound table as shown in Figure 2.18 before moving to the next one.

By looping through all time-distance blocks, we can populate the whole table and are able to visualize changes in speed of sound as a function of time and distance. Resulting speed of sound values were in the range of 3,000 to 3,500 ft/s, which is expected from this type of oil at the wellbore temperature. There is an exception around the ICV locations (at about 6,100 ft, 8,265 ft and 9,575 ft) as high frequency noises dominate the signal at these locations. A shift in the speed of sound is observed around 6,100 ft. This change is not due to any phase change but because change in the tubing radius and the corresponding change in temperature and pressure at that location. Our phase fraction modeling accounts for these changes as we covered in Sections 2.3.3 and 2.3.4.

One problem with Figure 2.18 is that it does not reveal any quantification of measurement uncertainty. To address this, we can take speed of sound results at a single time instance (a vertical slice from Figure 2.18) and plot the integral values for all distances. At each well distance, we also label the most probable speed of sound value and calculated confidence limits that were defined in Section 2.3.2. Figure 2.19 shows the results for Case 2, where the top ICV was half-open. Each horizontal slice

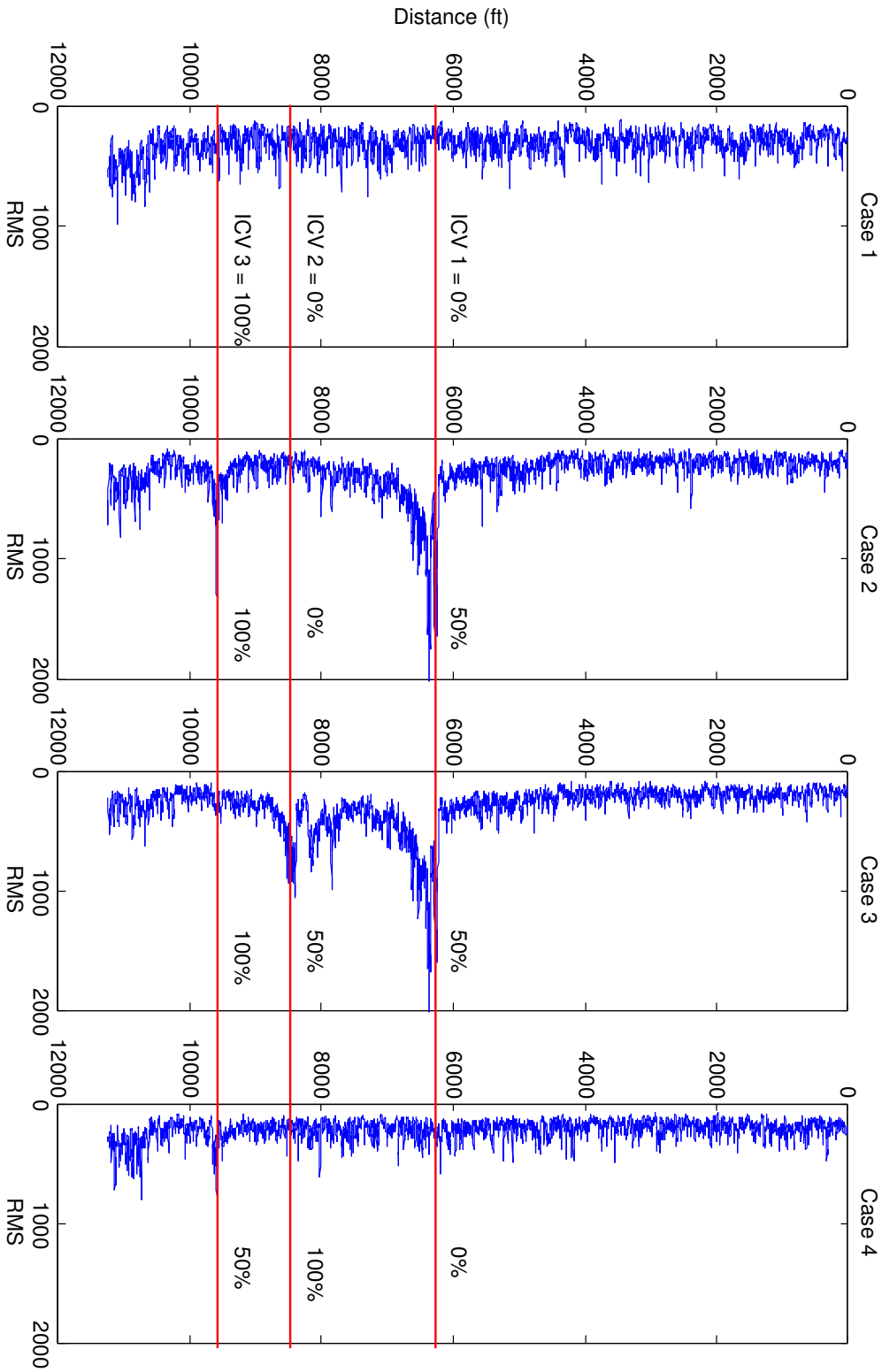


Figure 2.16: Root mean square values averaged over the test interval for four investigated flow scenarios.

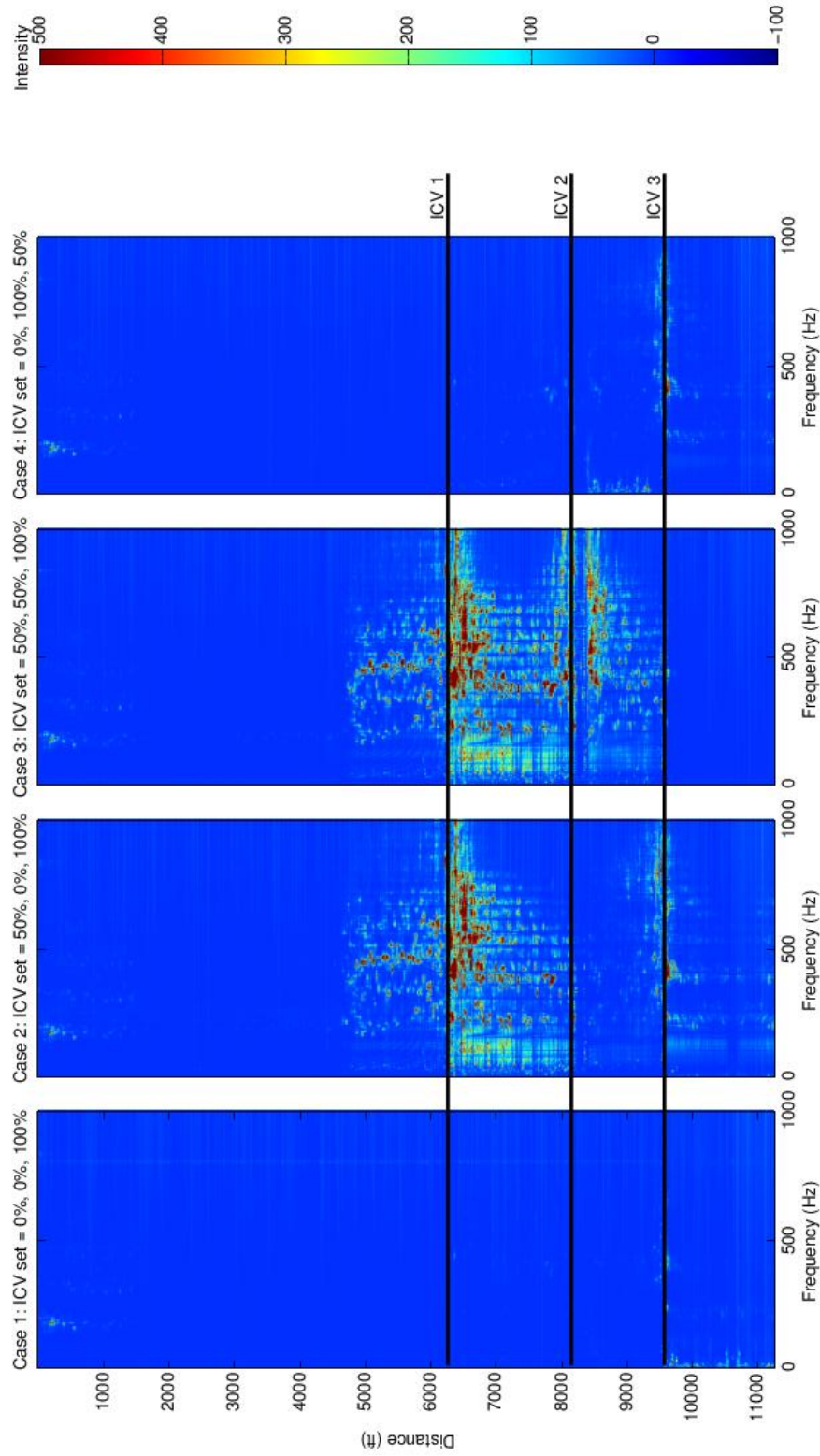


Figure 2.17: Frequency spectrogram for the four cases plotted against main bore distance.

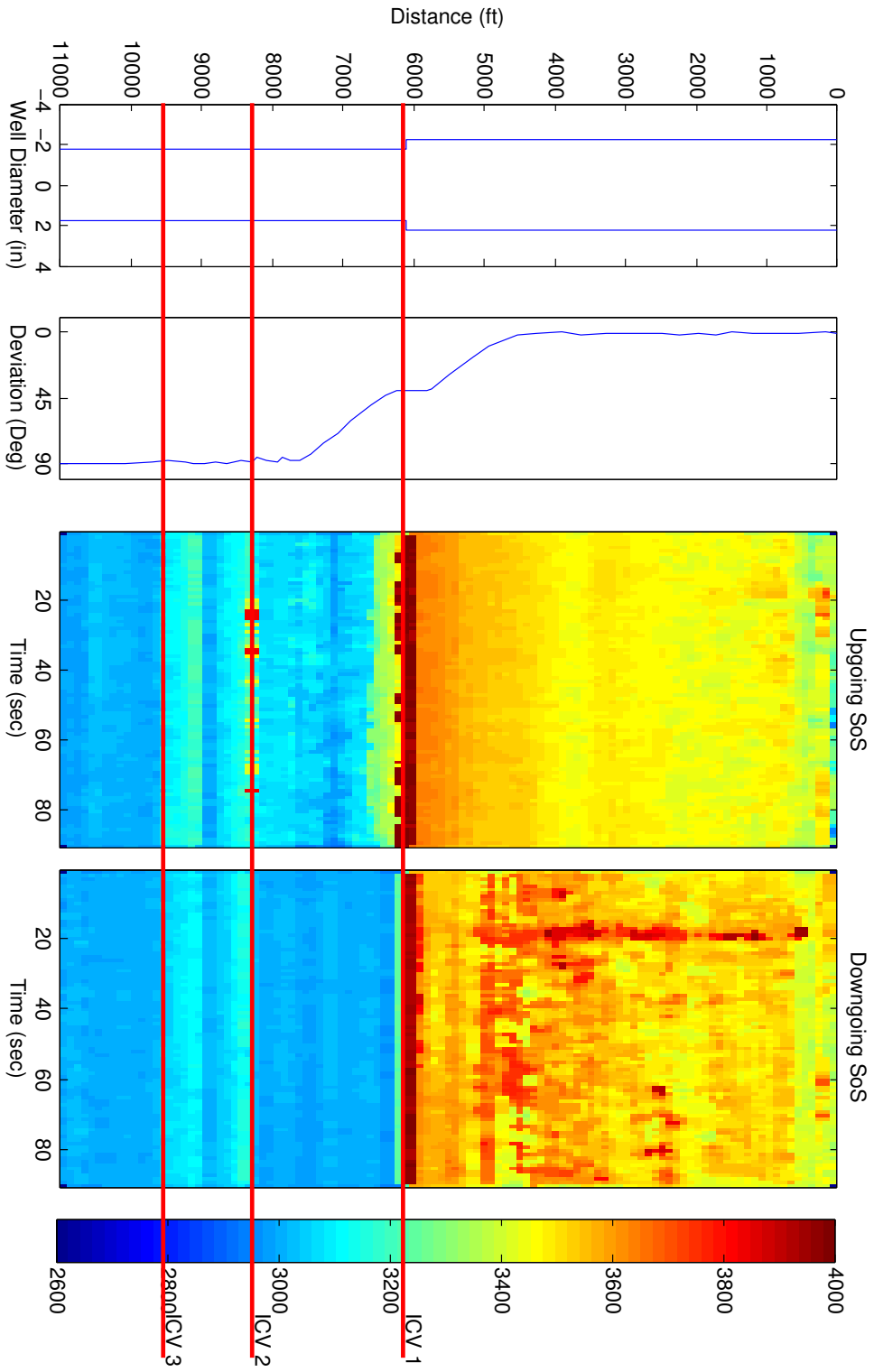


Figure 2.18: Upgoing (middle) and downgoing (right) speed of sound results after feeding the data to the signal processing algorithm. The plot to the left shows well completion details.

in that plot represents one integral image calculation at that corresponding distance. The confidence interval is indicated by the green bars on either side of the most probable speed of sound value (green circle). It can be seen from the figure that most measurements had high precision as the speed of sound line was very clear in the f - k domain. This observation was made for all other cases where at least one ICV was restricted. On the other hand, Case 1 (plotted in Figure 2.20), was the only tested case that does not exhibit this pattern. In this case, most confidence intervals were wide and the resulting speed of sound readings above 6,100 ft were above the expected range for this fluid (above 4,000 ft/s for single-phase oil). Estimates for the upgoing speed of sound in the upper and lower zones were also unreliable as the width of the confidence intervals exceeded the specified threshold. This is most likely related to what was observed in the spectrogram and RMS plots for this case; the acoustic signal was not strong enough when all valves were fully-open or fully-closed. This result makes further analysis for Case 1 unreliable.

These results were then used to calculate the fluid velocity using the Doppler shift derived in Equation (2.18) through several steps. First, some outliers that resulted in speed of sound measurements with uncertainty above a specified threshold were removed from the plot. Second, the instantaneous velocity calculated with the Doppler shift equation was averaged over several minutes. Then, velocity was converted to a volumetric flow rate estimation, as the wellbore diameter is known. Results for all but Case 1 are plotted in Figure 2.21. Because the well has three main entry points (against the ICVs), flow rate changes are only expected at these depths. This was not always the case, however, which might be due to the distance required to achieve a stabilized flow in the pipe after the inlet. Another artifact is observed at approximately 4,000 ft and above, where the flow rate tends to zero. This location coincides with the build-up section from vertical to horizontal. One explanation could be that the acoustic signal was lost from the tubing to the static fluid in the annulus due to high deviation angles at this location. Another reasoning for this phenomena might be related to overstretching the fiber when the tubing is bent. The fiber is attached to the well tubulars with clamps applying additional stress to it, so that might have caused additional disturbance in the acoustic readings.

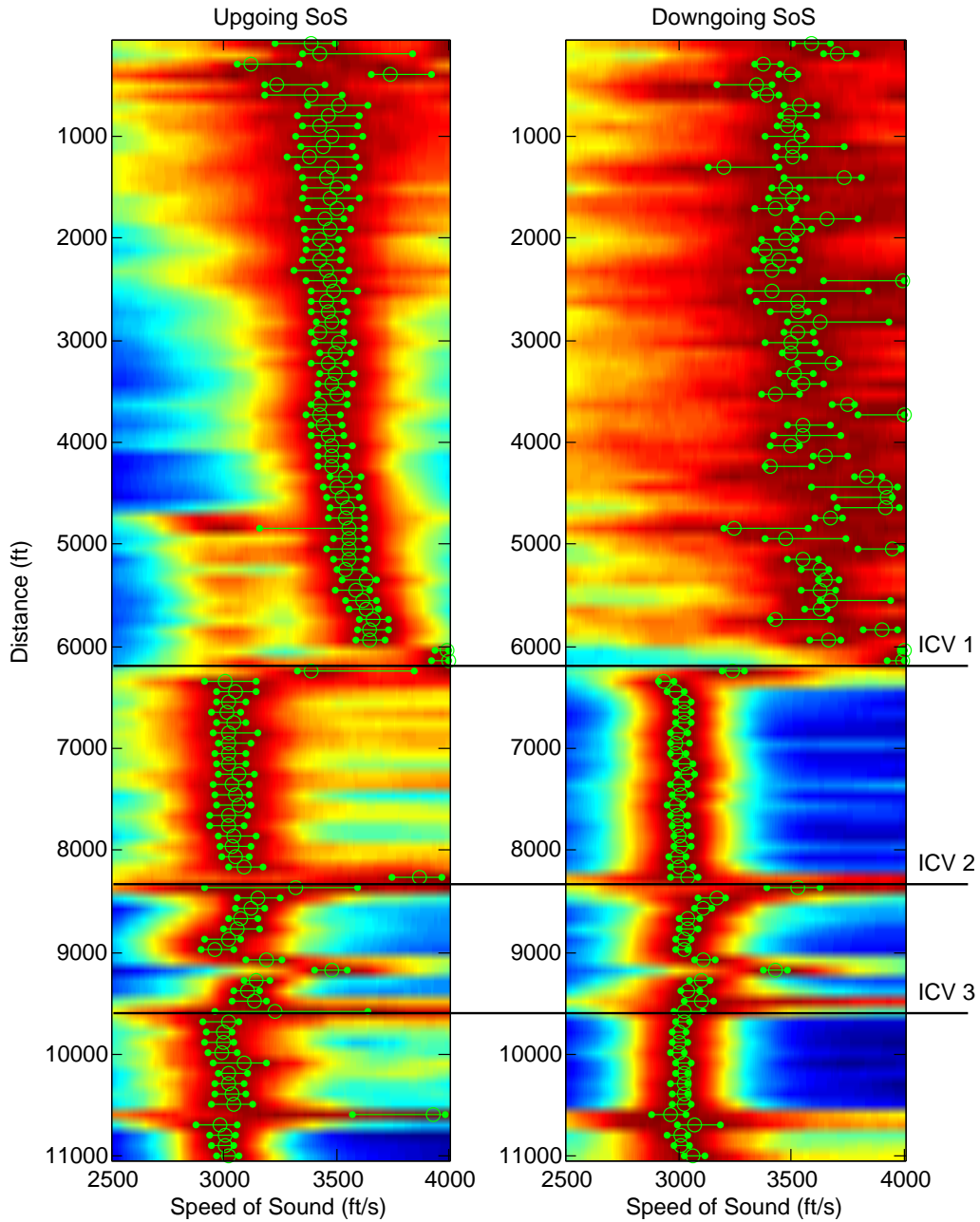


Figure 2.19: Speed of sound confidence interval for the second flow case. Green circles represent the most likely value and green bars represent the uncertainty range.

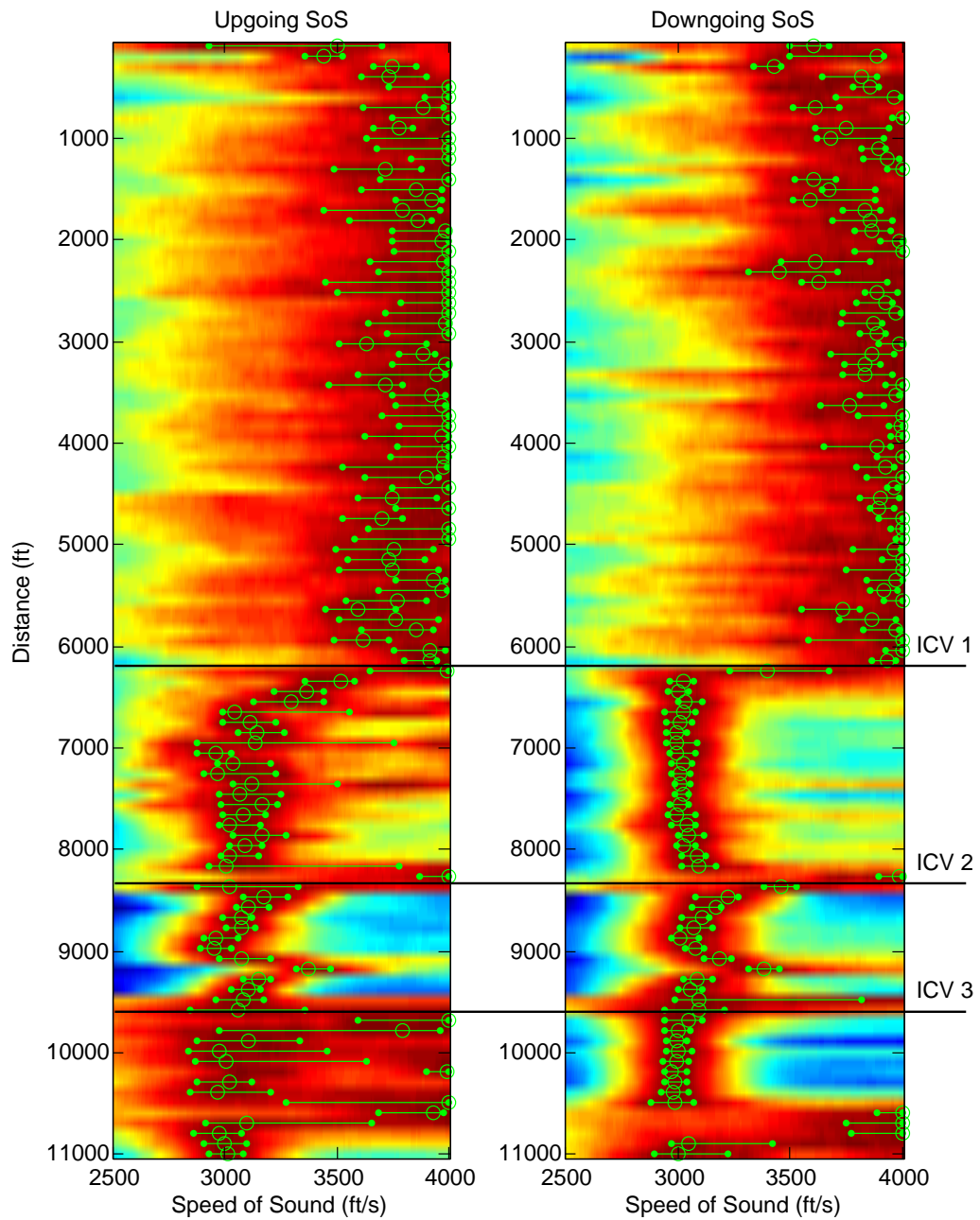


Figure 2.20: Speed of sound confidence interval for the first flow scenario. Green circles represent the most likely value and green lines represent the uncertainty range. Most calculated values have high uncertainty or are outside the expected range.

Because the diameter of ICVs constrict running PLT tools, only surface flow rates were available for reference. After accounting for flow from the three ICVs, the total flow rate from DAS was largely consistent with results from the surface flow meter. Total and individual ICV flow rate results are shown in Table 2.4. In general, the profile shape is analogous to results obtained by other flow profiling tools like the PLT.

To exploit one of the benefits of combining DAS with ICVs, we looked at the flow contribution from each ICV in every tested case (Table 2.5). This contribution was found by calculating the stabilized incremental production from each ICV. As tested cases were not exhaustive, the correlation between a valve opening size and its contribution is not always logical. Sometimes, competing production from laterals has the reverse effect on zone contribution as a closed ICV is opened and vice versa. For instance, as ICV 2 was moved from the closed to the half-open position between Case 2 and 3, the production of the other two ICVs was reduced by about 30% although their settings were unchanged. In another example, ICV 3 actually gained production when it was moved from the fully-open to the half-open position between Case 3 and 4 because ICV 1 was completely shut-off. This relieved some of the hydrostatic pressure in the well and encouraged lower production zones to contribute more. Testing more ICV setting combinations and analyzing them in a similar manner would enhance our understanding of the smart well performance. Note that shut-off ICVs did not show exactly zero contribution, which is common in mechanically operated valves.

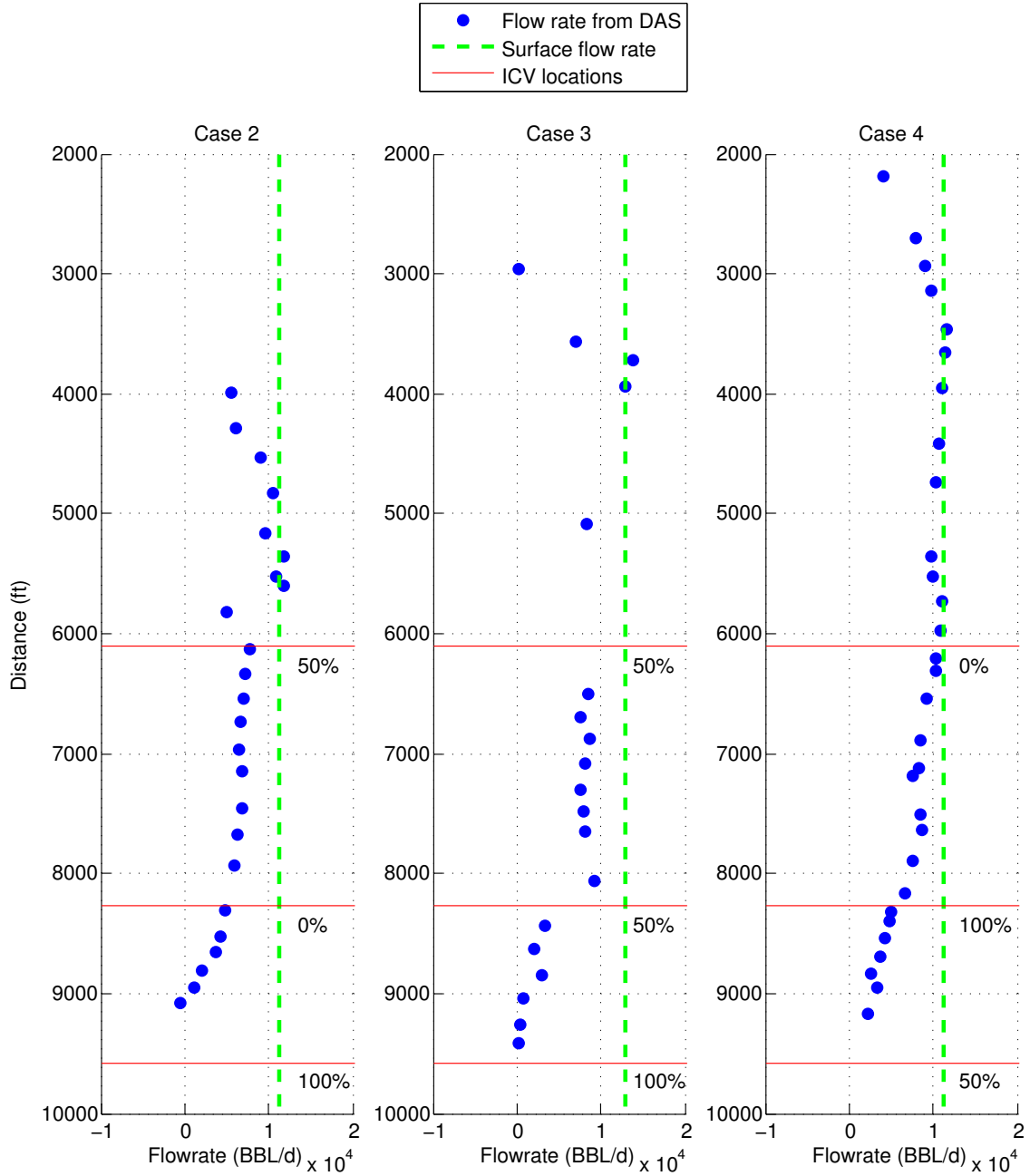


Figure 2.21: Flow rates calculated from DAS data compared with surface flow meter flow rates. ICV settings for the three cases are annotated below the red lines.

Table 2.4: Comparing flow rate results from DAS analysis with surface measurements for all flow scenarios. Flow rates corresponding to fully-open ICVs within a case are underlined while those representing fully-closed ICVs are between parentheses. Unformatted flow rates refer to ICVs that are 50% open.

	Production Rate (BBL/d)		
	Case 2	Case 3	Case 4
ICV 1	5,991	4,176	(83)
ICV 2	(429)	5,370	<u>6,046</u>
ICV 3	<u>4,860</u>	<u>3,337</u>	5,052
Total	11,280	12,883	11,181
Surface Meter	10,887	12,360	12,123
Difference (%)	3.61	4.23	-7.78

Table 2.5: Approximate production contribution percentage from each interval for the different flow scenarios. Fully-open ICVs in the case are underlined while fully-closed are between parentheses.

Valve	Flow Contribution (%)		
	Case 2	Case 3	Case 4
ICV 1	53.1	32.4	(0.7)
ICV 2	(3.8)	41.7	<u>54.1</u>
ICV 3	<u>43.1</u>	<u>25.9</u>	45.2

2.5.3 Analysis of DAS Data in an Oil Producer with High Water Cut

In this example, we looked at the added complexity introduced by two-phase flow as we analyzed DAS data from Well-B, which is an oil producer cutting 25% to 35% water. For the multiphase model to work, it is assumed that single-phase density, speed of sound and bulk modulus properties are determined accurately using one of the methods discussed in Section 2.3.4. Well-B is a long horizontal well with three ICVs installed to control three different production zones as shown in Figure 2.22. Each zone is isolated with a packer at either side of the ICV. The well is completed as cased-hole and was perforated selectively in each production zone. Data for two production cases were available, where the top ICV was moved from a fully-open to half-open position between the two cases as shown in Table 2.6. At room temperature, single-phase sound speeds were estimated to be 2,960 and 4,865 ft/s within oil and water, respectively (Xiao, 2013). These values were adjusted for downhole conditions accordingly.

Table 2.6: Well-B ICV details and results summary.

	Distance (ft)	Case 1	Case 2
ICV 1 opening	5,500	100	50
ICV 2 opening	7,040	50	50
ICV 3 opening	9,480	100	100
Surface WC (%)		34	29
DAS WC (%)		30	26

The speed of sound was calculated for every 300 ft and 10 seconds of data with results shown in Figure 2.23. It is clear that these results are different from the previous example. The behavior of the downgoing speed of sound is completely dissimilar from that of the upgoing, so each will be evaluated separately. To start, the distribution of downgoing speed of sound appears to be random with no correlation

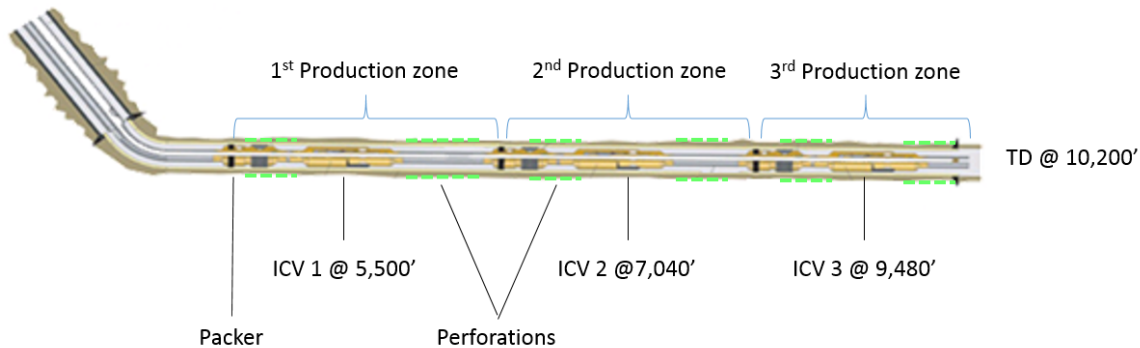


Figure 2.22: Well completion details for Well-B.

to depth or time. At most data blocks, the $f-k$ plot showed a clear line for the upgoing speed of sound but the high coefficients in the downgoing speed of sound were scattered (Figure 2.24). This behavior is characteristic of a low Signal-to-Noise Ratio (SNR) as explained in the work of Xiao et al. (2015). When this occurs, it is suggested that another sound source, such as a surface seismic wave, be used to increase the SNR in addition to acoustic waves generated by fluids passing through the ICV. To understand why this might have happened, we take a closer look at the well completion as illustrated by Figure 2.25. Due to the positioning of the ICV relative to the perforation intervals, the annulus behind the tubing exhibits both cocurrent (with the flow direction) and countercurrent (against flow direction) flows. The extra flow activity behind the pipe might have introduced destructive wave interference.

Despite the inaccuracies in the downgoing speed of sound, the upgoing speed of sound still revealed meaningful results. For example, as the fluid moves from the middle to the top flow zone, a slight increase in speed of sound values is recorded as shown in Figure 2.23. This indicates an increased inflow of water, the heavier of the two phases, from the top compartment. Another interesting phenomenon is taking place in the third flow zone, where pockets of low speed of sound are periodically followed by high speeds of sound. Although calculated sound speeds were based on the assumption that we have a homogenous flow pattern, this behavior presents a clear indication of slug flow. By drawing a slope line through the oil slug, we can estimate the in-situ velocity of the moving oil slug to be approximately 6 ft/s in

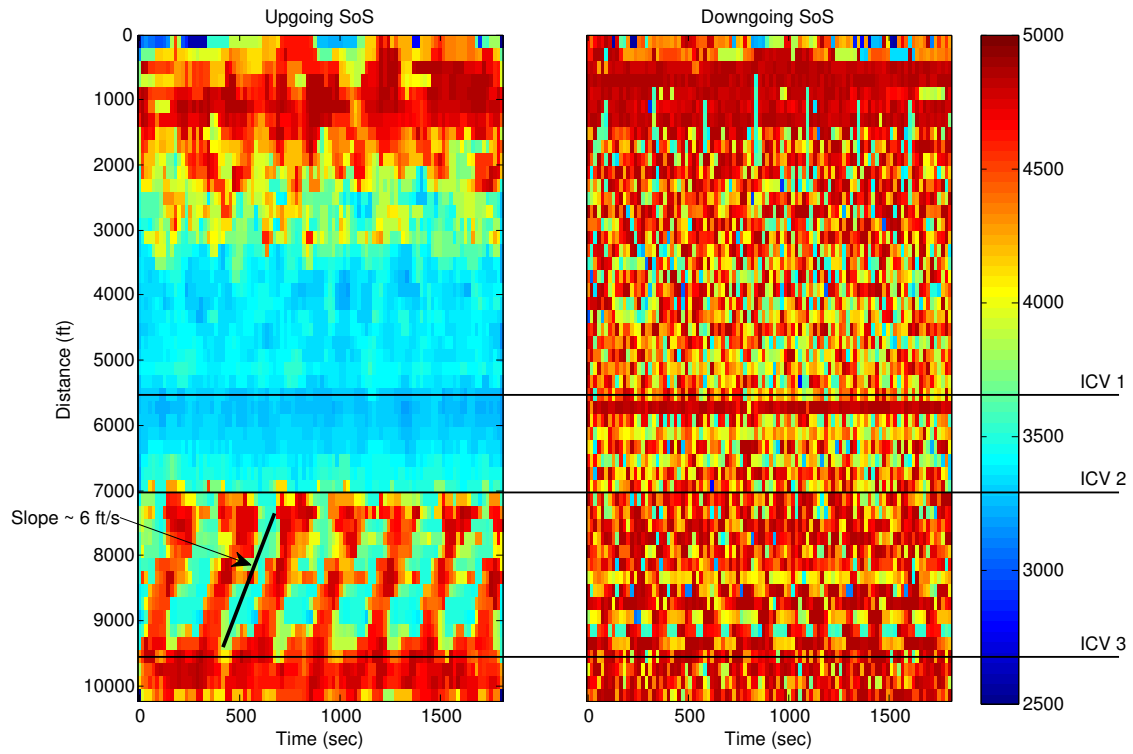


Figure 2.23: Upgoing and downgoing speed of sound calculated in ft/s at different time and well distances. Horizontal lines mark the ICV locations and the slope line in the left plot follows movement of the oil phase in the third production zone.

this case. Similar to Well-A, these data also showed an artifact near and above the build-up section of the well.

As downgoing speed of sound was inaccurate for this case, construction of a velocity profile was not possible. In two-phase flow, however, we can go one step further by calculating phase fractions using Equation (2.10). For this purpose, the static speed of sound in the mixture is approximated with the upgoing speed of sound. The result of completing this step is shown in Figure 2.26 for both flow scenarios. As an initial validation, calculated phase fractions were always between zero and one (speed of sound values were between the oil and the water phase values). Looking at the oil phase fraction variation with distance down the main bore confirms our earlier observations. The oil phase fraction in the bottom interval shows varying values as

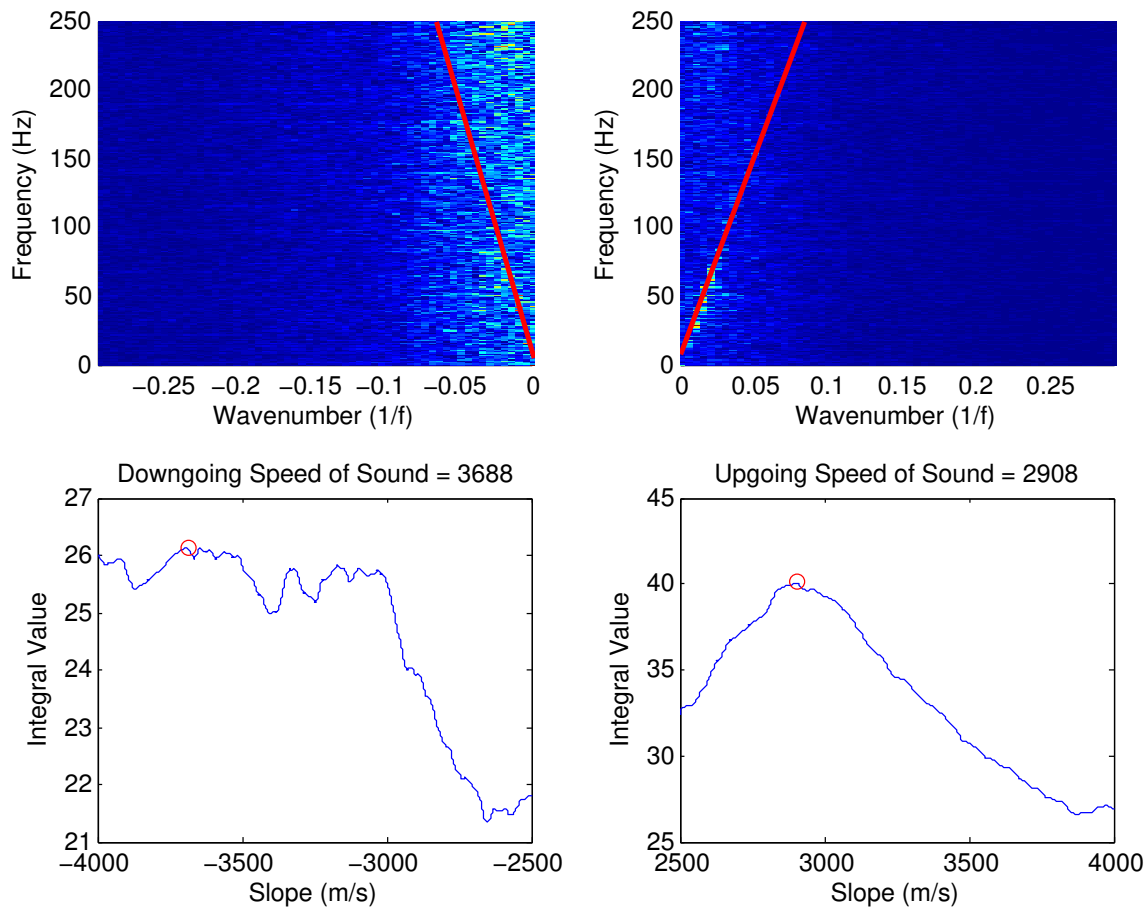


Figure 2.24: Typical $f-k$ plot for Well-B shows low SNR in the downgoing speed of sound (left), whereas the upgoing speed of sound line is easily detectable (right).

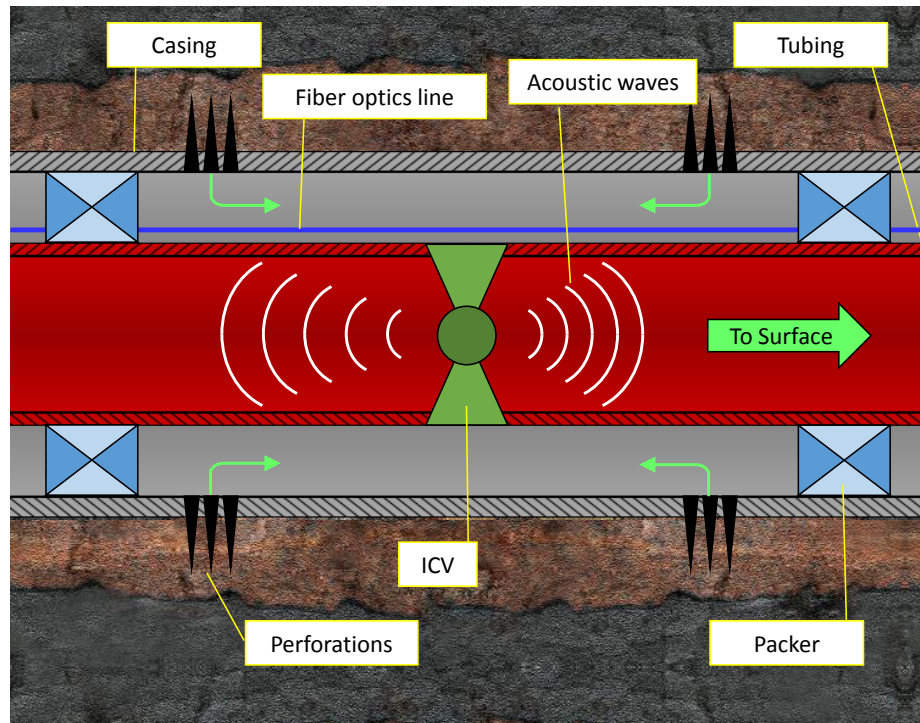


Figure 2.25: Close-up of the smart completion unit in Well-B highlights expected cocurrent and countercurrent fluid movement behind the pipe.

oil slugs move through the zone. The second zone shows more oil inflow relative to the lowest one, while the top zone introduces slightly more water. We only took this calculation up to 3,500 ft (near the horizontal build-up section) as acoustic data suffered increased noises above that location as discussed in Section 2.5.2. Calculated oil fractions at this distance were comparable to what was measured in the field with approximately 4% difference as summarized in Table 2.6. Interestingly, the restriction of ICV 1 in Case 2 actually increased the oil fraction by about 4%. This is because ICV 1 was producing higher water and restricting it might have reduced water coning effects around the segment. Such an outcome would be desirable if increasing oil recovery or reducing the water cut (WC) was a priority for the operator.

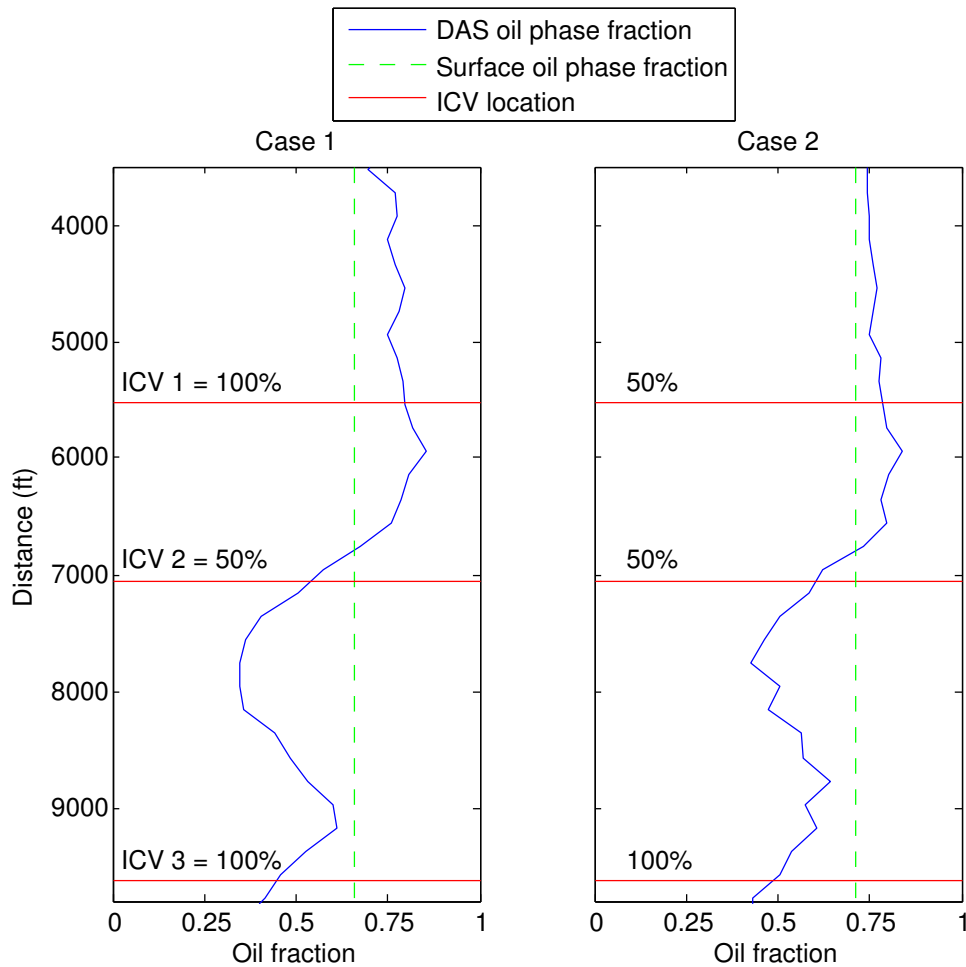


Figure 2.26: Calculation of the oil phase fraction as a function of well distance provides an insight of the oil contribution from each production zone.

2.6 Concluding Remarks

In this chapter, we have presented analysis of acoustic data that are distributed in time and space. Separate modules to open and visualize the data, calculate the speed of sound, and estimate in-situ phase fractions were developed. Results from such an analysis provide direct measurement of flow properties in a similar manner to PLT logs. Unlike PLT, however, DAS continuous flow of data enables the user to track production changes from a smart well.

This approach was applied to real wells involving single-phase oil and two-phase oil-water producers. We also tested the algorithm on a steam injection well but were unable to obtain permission to publish the results from the operator. For the single-phase oil well, a flow rate was calculated as a function of distance for different ICV settings. Analyzing those cases gave us some understanding of the effects associated with moving each individual ICV. In the two-phase flow well, the phase fraction was calculated for regions where a homogeneous flow regime exists. In another instance where our assumption of homogeneous flow was not satisfied, inferences about the flow (such as the oil slug velocity) could be made.

Although the algorithm showed success in flow profiling several cases, a number of limitations were recognized. For example, readings above the build-up section were mostly unreliable. This can often be overlooked as the vertical section usually does not contribute to production in horizontal wells. Another algorithm failure arose in calculating downgoing speed of sound for two-phase flow when there is countercurrent flow behind the pipe. As only one well was available with these conditions, it is not clear if the failure was caused by two-phase flow or the completion type. Moreover, evaluated flow scenarios indicate that at least one ICV should be restricted for an acoustic wave to be picked up clearly by DAS. In general, the speed of sound in the direction of flow (upgoing for production and downgoing for injection) was calculated with lower uncertainty for all analyzed cases.

In the next chapter, we explore temperature; another distributed measurement that is obtained from fiber optic sensors. The discussion will be focused mainly on ways in which DTS can be used to improve the inflow profiling scheme for DAS measurements.

Chapter 3

Inflow Profiling With Distributed Temperature Sensing

Generally, distributed temperature measurements can be collected along with acoustics using the same fiber. Therefore, evaluating how the addition of temperature improves the developed inflow profiling algorithm is the next logical step. DTS data track the absolute temperature value along time and depth. Figure 3.1 shows a typical DTS plot recorded during water injection, which can be used to quantify injectivity in different zones within the reservoir. Note that sudden temperature changes correspond to fluid influx from the hotter reservoir to the wellbore. Integrating temperature measurements in inflow profiling analysis provides an opportunity to improve performance in two-phase problems. Additionally, cointerpretation of temperature and acoustic data could be used for three-phase profiling problems under certain circumstances.

Most previous work on DTS focused on building an inverse model based on the energy equation to estimate flow rates from the temperature profile (Li, 2010; Wang, 2012; Yoshioka, 2007). As DAS analysis involves correlating direct measurements to the physical fluid properties to make a phase fraction calculation, it is difficult to integrate such inverse models with the DAS analysis. Moreover, these models are usually adequate to obtain the total flow rates but are insufficient to estimate

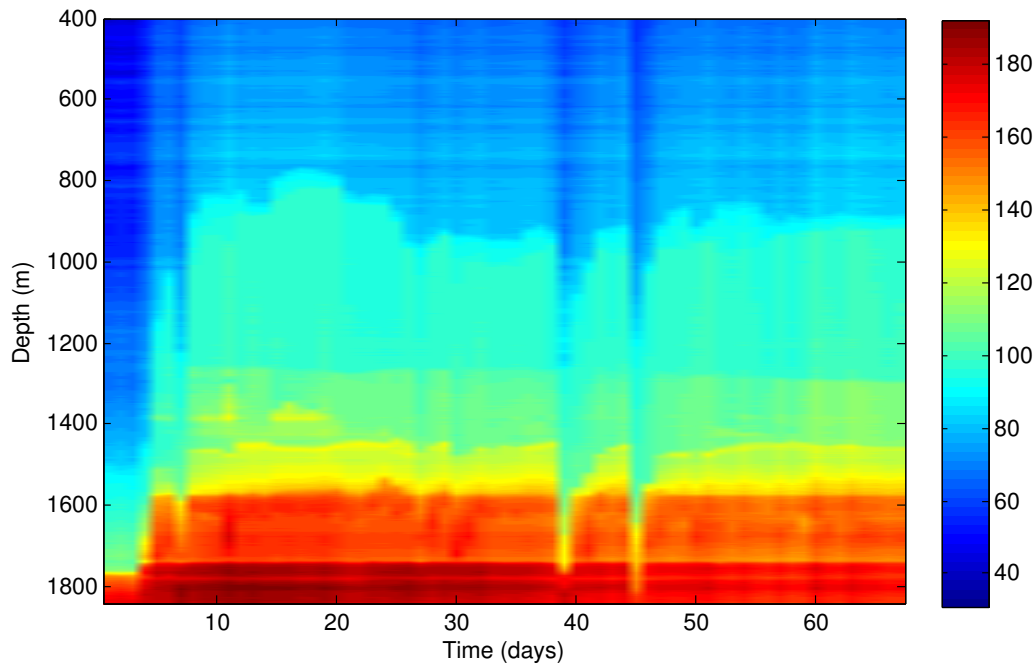


Figure 3.1: DTS data example recorded in $^{\circ}\text{C}$ as a function of depth and time

phase flows accurately. Thus, a novel approach is suggested to calculate inflow phase fractions based on the fluids' thermal expansion as the fluids undergo withdrawal pressure between the reservoir and the wellbore. The idea revolves around estimating the Joule-Thomson coefficient (C_{JT}), which describes this thermal expansion based on temperature measurements.

The chapter proceeds as follows. First, we describe the Joule-Thomson effect and derive its expression as a function of the fluid phase fractions. This definition implies that a fluid phase fraction can be determined if the coefficient is measured in a production zone. Next, we present a reservoir simulation study that demonstrates how we would employ the derived equations in calculating the producing phase fraction. Finally, we discuss the applicability of this approach in three-phase flows and how it can be easily integrated with DAS analysis.

3.1 The Joule-Thomson Coefficient

The Joule-Thomson effect is observable as the temperature change of real gases or liquids when they are forced through a valve or porous plug with no heat exchange in the environment (adiabatic process). The original experiments of Joule and Thomson state that this temperature change is (Roy, 2002):

$$C_{JT} = \frac{\Delta T}{\Delta p} = \frac{T_{sf} - T_{well}}{p_{sf} - p_{well}}, \quad (3.1)$$

where T_{sf} , T_{well} , p_{sf} , and p_{well} , refer to the sandface and well temperatures and pressures. This definition implies that positive values describe cooling effect as the fluid is drawn from the reservoir to the wellbore, as is the case with most gases for typical wellbore pressures and temperatures. On the other hand, liquids flowing to the wellbore usually show a heating effect indicated by a negative Joule-Thomson coefficient value.

Considering that this effect is a thermodynamic property, it can also be derived by applying Maxwell's relations to the definition of enthalpy. For that purpose, we follow the derivation presented in Hasan and Kabir (2002) starting from:

$$dH = TdS + Vdp, \quad (3.2)$$

where H is the enthalpy and S is the entropy. The entropy is replaced by more known and measurable properties with the following relationships:

$$dS = \left(\frac{\partial S}{\partial T}\right)_p dT + \left(\frac{\partial S}{\partial p}\right)_T dp = \left(\frac{\partial S}{\partial T}\right)_p dT - \left(\frac{\partial V}{\partial T}\right)_p dp, \quad (3.3)$$

and

$$c_p = \left(\frac{\partial H}{\partial T}\right)_p = T \left(\frac{\partial S}{\partial T}\right)_p, \quad (3.4)$$

where c_p is the fluid heat capacity. After substituting Equations (3.3) and (3.4) in

Equation (3.2), we obtain an expression for enthalpy change as:

$$dH = c_p dT + \left[V - T \left(\frac{\partial V}{\partial T} \right)_p \right] dp. \quad (3.5)$$

A final equation of state (EoS) definition of the Joule-Thomson coefficient can be found by dividing all terms in Equation (3.5) by dp . By doing so, the left-hand side of the equation will be reduced to zero as we are working under the assumption that there is no heat exchange with the environment. This gives us the following correlation for the Joule-Thomson coefficient (Hasan and Kabir, 2002):

$$C_{JT} = \frac{T_{well} - T_{sf}}{p_{well} - p_{sf}} = \frac{1}{c_p} \left[T_{well} \left(\frac{\partial V}{\partial T_{well}} \right)_p - V \right]. \quad (3.6)$$

3.1.1 Joule-Thomson Coefficient for Mixtures

The previous derivation for C_{JT} was made for a single-phase fluid. Utilization of the Joule-Thomson coefficient in interpreting in-situ phase fraction will become clearer when the derivation is extended for two-phase flow. This extension was presented by Wang et al. (2008) and depends on two main notions. First, mixture thermal properties (such as heat capacity and thermal expansion) are the mass-weighted average of individual phase properties. Second, thermal expansion for real gases is defined based on $V = ZnRT/p$ as:

$$\left(\frac{\partial V_g}{\partial T} \right)_p = \frac{ZnR}{p} + \frac{nRT}{p} \left(\frac{\partial Z}{\partial T} \right)_p = \frac{V_g}{T} + \frac{V_g}{Z} \left(\frac{\partial Z}{\partial T} \right)_p, \quad (3.7)$$

where n is the fluid amount in moles and Z is the gas compressibility factor. For liquid, compressibility plays a lesser role, which allows us to define thermal expansion as:

$$\beta_l = \frac{1}{V_l} \left(\frac{\partial V_l}{\partial T} \right)_p \Rightarrow \left(\frac{\partial V_l}{\partial T} \right)_p = \beta_l V_l, \quad (3.8)$$

where β is the liquid thermal expansion coefficient. Applying these two steps on Equation (3.6) and assuming a gas-oil mixture provides us with the final expression for the mixture Joule-Thomson coefficient as:

$$C_{JT} = \frac{\frac{x_g T_{well}}{Z \rho_g} \left(\frac{\partial Z}{\partial T_{well}} \right)_p + \frac{x_o}{\rho_o} (T_{well} \beta_o - 1)}{x_g c_{p,g} + x_o c_{p,o}}, \quad (3.9)$$

where x_g and x_o are the gas and oil mass-weighted phase fractions. If water was present in the flow system, it would take a form similar to the oil phase equation. It should be noted that this equation is valid for the bottom production zone. When measuring temperature from a perforation in the middle of the wellbore, temperature change is a function of the Joule-Thomson effect of incoming fluids as well as the heat flux from lower zones. A description of the modification needed to account for that is provided in Appendix B. As our objective is to solve for the phase fraction as a function of measured Joule-Thomson, we invert Equation (3.9) to get $x_g = 1 - x_o$ as:

$$x_g = \frac{(T_{well} \beta_o - 1) / \rho_o - C_{JT} c_{p,o}}{C_{JT} c_{p,g} - C_{JT} c_{p,o} + \frac{T_{well} \beta_o}{\rho_o} - \frac{T_{well}}{Z \rho_g} \left(\frac{\partial Z}{\partial T_{well}} \right)_p}. \quad (3.10)$$

C_{JT} here is calculated with DTS measurements as we will explain in Section 3.1.2 while all other parameters are single-phase properties, which can be found with PVT analysis. The volumetric phase fraction, α_g , can be found with the following expression:

$$\alpha_g = \frac{\text{gas volume}}{\text{total volume}} = \frac{x_g / \rho_g}{x_g / \rho_g + (1 - x_g) / \rho_o}. \quad (3.11)$$

To show a general solution of Equation (3.10), we look at different two-phase mixture combinations with the fluid properties listed in Table 3.1. The solution is presented in Figure 3.2 in a similar manner to the solution of Equation (2.10) for the speed of sound (previously shown in Figure 2.9). Contrary to that plot, solutions for all three fluids mixtures are monotonic functions. This allows for a unique phase-fraction calculation if C_{JT} is determined accurately for two-phase flows. The water-gas and oil-gas curves have a very high slope when the gas fraction is low. This is

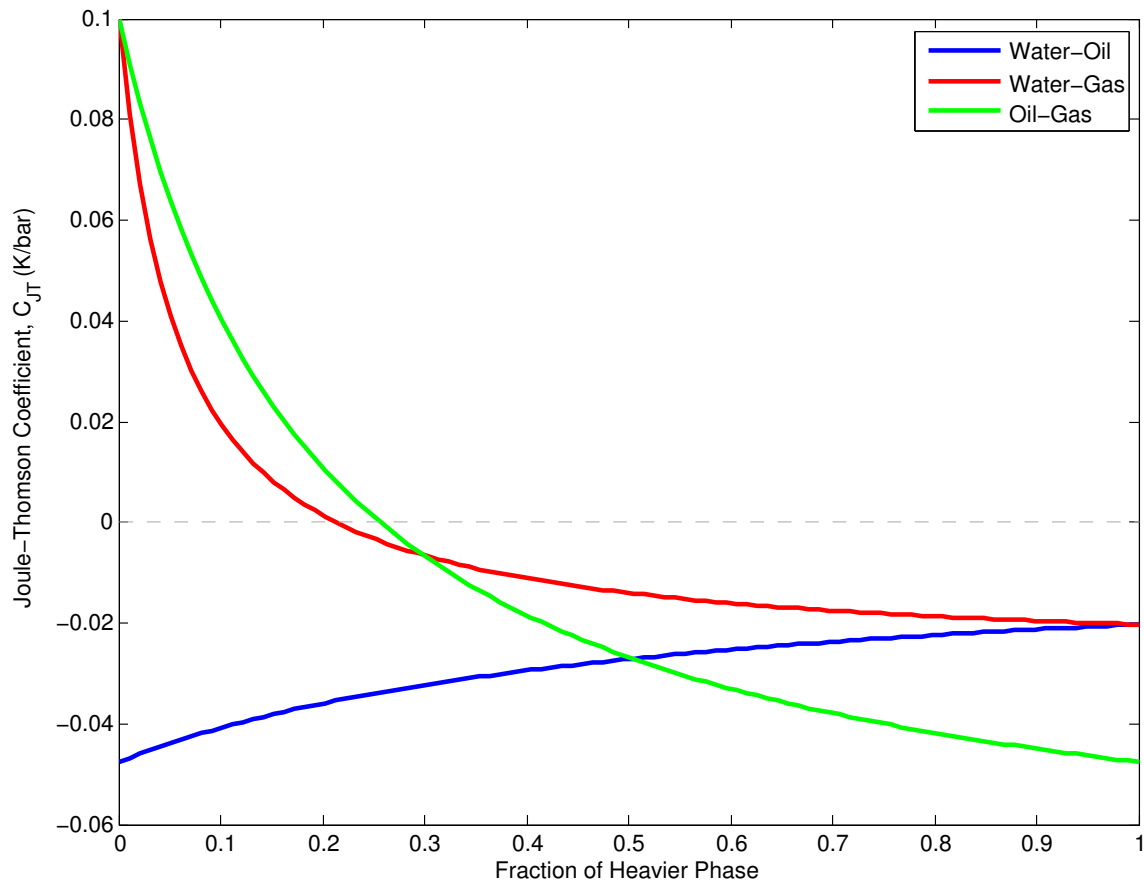


Figure 3.2: Joule-Thomson effect as a function of the heavier phase volume fraction for three different fluid mixtures.

the opposite of the speed of sound vs. phase fraction correlation, which had a very high slope for low gas phase fractions. This suggests that using DTS is preferable to solve the problem for high gas volume fractions whereas DAS should perform better for low gas fractions. It is also noted that the Joule-Thomson coefficient is negative for the liquids but becomes positive in gas-dominated mixtures. This is consistent with the convention of cooling/heating effects associated with the fluid type flowing into the wellbore.

Table 3.1: Fluid thermal properties used to solve the correlation between phase fraction and Joule-Thomson coefficient

Property		Water	Oil	Gas
Density	ρ (kg/m ³)	998	820	127
Thermal Expansion	β (1/K)	2.0×10^{-4}	8.0×10^{-4}	7.6×10^{-4} *
Heat Capacity	c_p (J/g/K)	4.18	1.88	2

* $\frac{1}{Z} \left(\frac{\partial Z}{\partial T} \right)_p$ for gas approximated by $\frac{1}{Z} \left(\frac{\delta Z}{\delta T} \right)_p$ from simulation output.

3.1.2 Well Completion Design to Capture the Joule-Thomson Coefficient

In the previous section, we have established that phase fractions can be determined from the Joule-Thomson coefficient in two-phase flow. In this section, we show that a measurement of C_{JT} can be made in smart wells enabled by their sensory capabilities. Equation (3.1) shows that we can accomplish this by obtaining four well measurements; namely, the reservoir and well temperatures and pressures. Note that the reservoir temperature referred to here is the entry temperature at the sand-face just before the fluid undergoes thermal expansion. At the entry points to the well, this temperature is different than the undisturbed geothermal temperature away from the well due to several viscous dissipation, heat transfer effects, and adiabatic expansion effects (Wang, 2012). The difference between the two temperatures and the mixing temperature in the wellbore is demonstrated in Figure 3.3.

A simple modification to current completion strategies could be made to capture pressure and temperature measurements needed to evaluate C_{JT} as shown in Figure 3.4. The modified completion involves only one adjustment compared to typical smart well completions; installing another optical fiber behind the casing. Running a fiber behind the casing and running multiple fibers have both been done in the past as highlighted by examples from Koelman et al. (2011) and Furniss et al. (2014). Because behind-the-casing fibers are permanently cemented, it is actually common

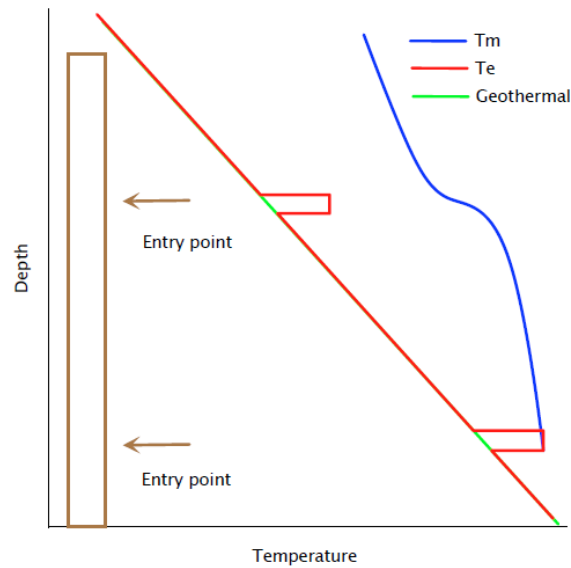


Figure 3.3: Difference between mixing temperature, T_m ; entry temperature, T_e ; and geothermal temperature. From Wang (2012).

to duplicate them in case one was damaged by perforating the casing.

Now that the smart well is equipped with two fibers and a set of ICVs, it is possible to obtain all information required to calculate C_{JT} . We specifically mention ICVs as current fiber technology is not capable of providing distributed pressure. Each item is obtained by the following:

Reservoir pressure by the pressure sensor in each ICV when the well is shut-in.

This is a common current practice to estimate the reservoir pressure.

Well pressure by the pressure sensor in each ICV during flowing conditions.

Reservoir temperature from the fiber placed behind the casing.

Well temperature from the temperature sensor in the ICVs or from the fiber placed in the tubing.

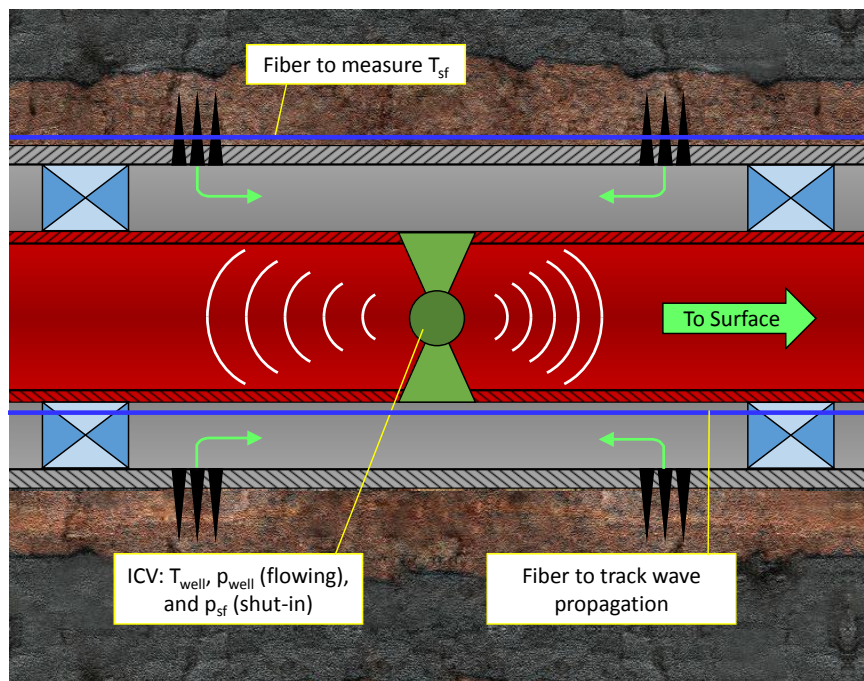


Figure 3.4: Suggested completion configuration to capture all needed values for the Joule-Thomson coefficient calculation.

3.2 Practical Application for Inflow Profiling Using Distributed Temperature Sensing

As we did not have data from a real well completed with the described configuration to calculate C_{JT} , synthetic data were generated with a commercial thermal simulator. After testing how temperature changes in single-phase flow scenarios, Equation (3.10) was used to find phase fractions in two phase flow. The chapter is concluded by discussing the implications of adding this information to DAS inflow profiling information.

To generate temperature data that resembles the well completion described in Figure 3.4, ECLIPSE 2013.2 thermal reservoir simulation package was used. The simulation involves solving an energy balance equation for each grid cell in addition to the mass balance equation. The expression of the energy equation is in the form:

$$R = \frac{d}{dt}(V_b e) + F_e + C_e + Q_{HL} + Q_w = 0, \quad (3.12)$$

where R is the residual, V_b is the bulk volume and e is the bulk internal energy density. F_e and C_e refer to the convective enthalpy and conductive energy flow rates into neighboring grid blocks. Lastly, Q_{HL} and Q_w represent the heat loss to surrounding rocks and the net enthalpy flow rate into wells. Details of the individual terms in this equation and the solution method can be found in the software documentation (GeoQuest, 2013).

A simple radial reservoir simulation model was constructed to test this inflow profiling methodology. Diameter of the first ring was set to 0.1 ft higher than the wellbore diameter to get a measurement of the sand-face temperature (Figure 3.5). The well was defined as a multisegment well to track temperature variation along the wellbore. The model contains 40 1-foot layers to provide temperatures with a similar resolution to DTS. With this setup, grid block and wellbore simulation temperature and pressure values would be considered as those provided by the fiber and ICV.

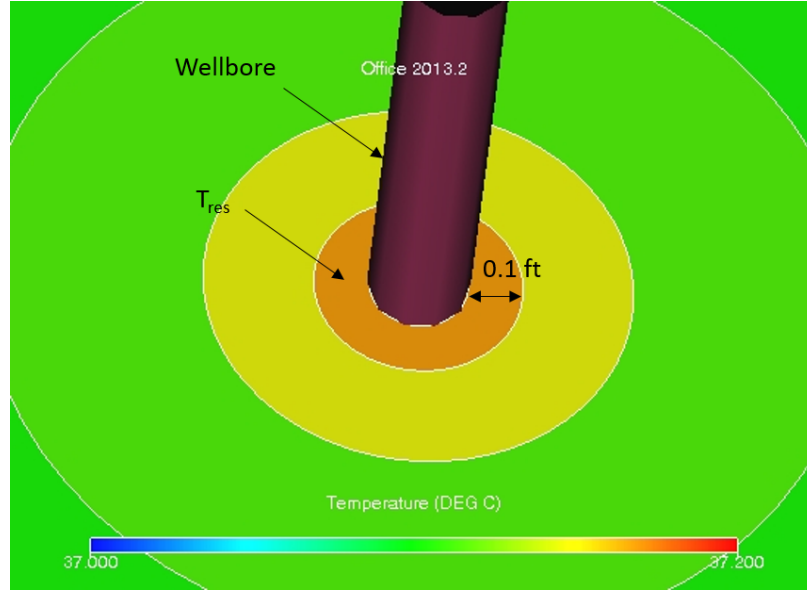


Figure 3.5: Radial reservoir simulation model used to replicate DTS in providing reservoir and wellbore temperature data.

3.2.1 Solution for Single-Phase Flow

Before using the Joule-Thomson coefficient to calculate phase fractions, we examined single-phase flow cases for validation. At a wellbore connection, reservoir fluids are produced through the well perforations according to the following equation (GeoQuest, 2013):

$$q_p = T_w M_p (p_{res} - p_{BH} - p_H), \quad (3.13)$$

where q_p is the volumetric flow rate of phase p in the connection at standard conditions and T_w is the transmissibility factor. The three pressures in the equation refer to the grid block pressure containing the connection, the bottom hole pressure of the well, and the hydrostatic pressure, respectively. M_p is the phase mobility at the connection defined as:

$$M_p = \frac{k_{r,p}}{B_p \mu_p}, \quad (3.14)$$

where $k_{r,p}$ is the relative permeability of the phase, μ_p is the phase viscosity, and B_p is the phase formation volume factor.

The thermal simulator accounts for Joule-Thomson effects of each component in the gaseous phase with the following equation (GeoQuest, 2013):

$$H_g = \sum_{c=1}^{N^c} y^c (M^c H_g^c(T) + H_{JT}^c(p)), \quad (3.15)$$

where y^c is the mole fraction of N^c components in the gas phase and M^c is the molecular weight of the component. The temperature dependent gas enthalpy is given by:

$$H_g^c = H_{vap}^c + c_p^c (T - T_{std}), \quad (3.16)$$

where H_{vap}^c is the heat of vaporization at the standard temperature, T_{std} , and c_p^c is the specific heat of the component. Similarly, the pressure dependent enthalpy is expressed as:

$$H_{JT}^c = -C_{JT}^c M^c c_p^c (p - p_{std}). \quad (3.17)$$

When it comes to liquids, the simulator only accounts for Joule-Thomson effects in the water phase. This is accomplished by using water and steam energies and enthalpies from steam tables in Perry and Green (1984). Because ECLIPSE ignores the Joule-Thomson effect in the oil phase, we modeled oil as a second water component for runs that required three-phase flow.

To demonstrate the solution for the above equation, simulation runs were performed using the thermal fluid properties listed in Table 3.1. As shown in Figure 3.6, the cooling and heating effects are captured by the simulator as fluids are produced through the perforations for single-phase gas and water, respectively. In other words, the produced gas temperature drops as it undergoes the pressure drop from the reservoir to the wellbore. This behavior is reversed for water and oil due to their thermal properties. Note that the reservoir and well pressures are dropping during production. This causes a slight drop in reservoir and well temperatures when gas is produced as $C_{JT} = dT/dP > 0$ and a slight increase for liquid production since $C_{JT} = dT/dP < 0$. The temperature for single-phase water is also plotted as a function of distance from the wellbore in Figure 3.7. As we move from the reservoir

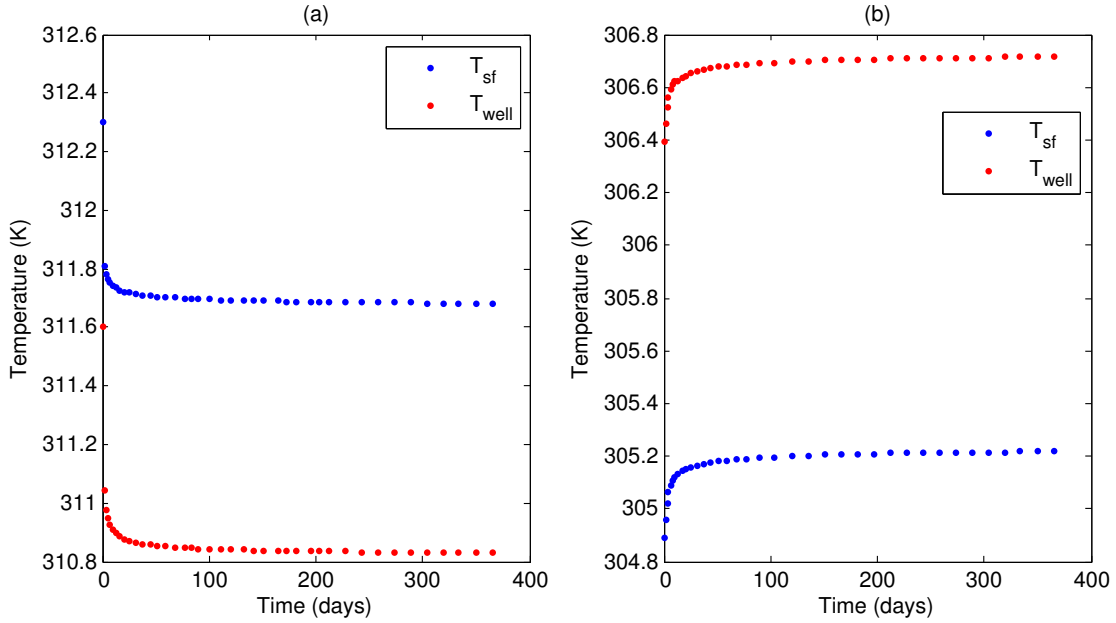


Figure 3.6: Single-phase reservoir and wellbore simulation data for (a) gas and (b) water. Cooling/heating effects associated with thermal expansion of the two fluids is apparent in the plots.

to the wellbore, the temperature increases either due to pipe material conductivity or due to the Joule-Thomson effect.

Next, temperature results from the simulator were treated as the DTS output, to be used in Equation (3.1) to find simulated C_{JT} (or measured via DTS in real applications). The coefficient was also evaluated from the EoS for each phase using Equation (3.9). Comparisons of the two values for gas and water are shown in Figure 3.8. The difference between theoretical and calculated Joule-Thomson coefficient values was no more than 3% for gas and 0.5% for water.

3.2.2 Example in an Oil-Gas Producer

After validating the procedure for single-phase flow, the simulation run was modified to include two-phase oil-gas production. A gas cap was placed above the reservoir and the simulation was run for a year. This provided a wide range of gas volume fractions

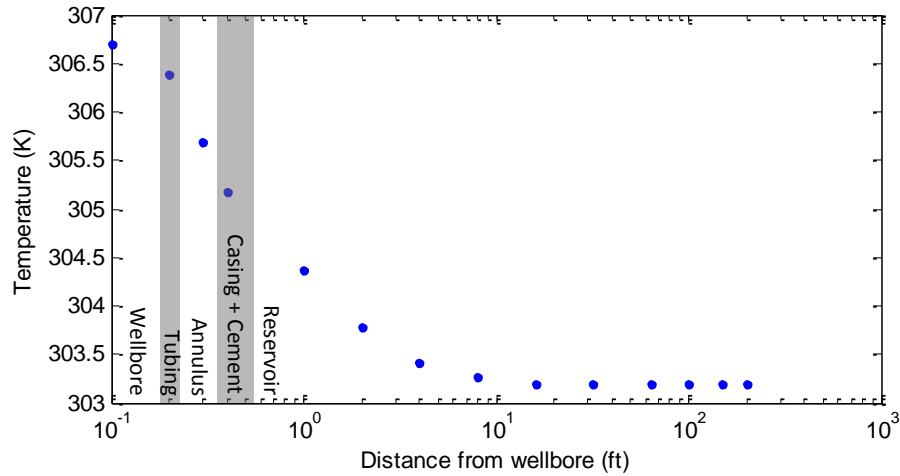


Figure 3.7: Temperature as a function of distance from the wellbore for single-phase water production. Approximate locations of the tubing, the annulus, and the casing are indicated in gray.

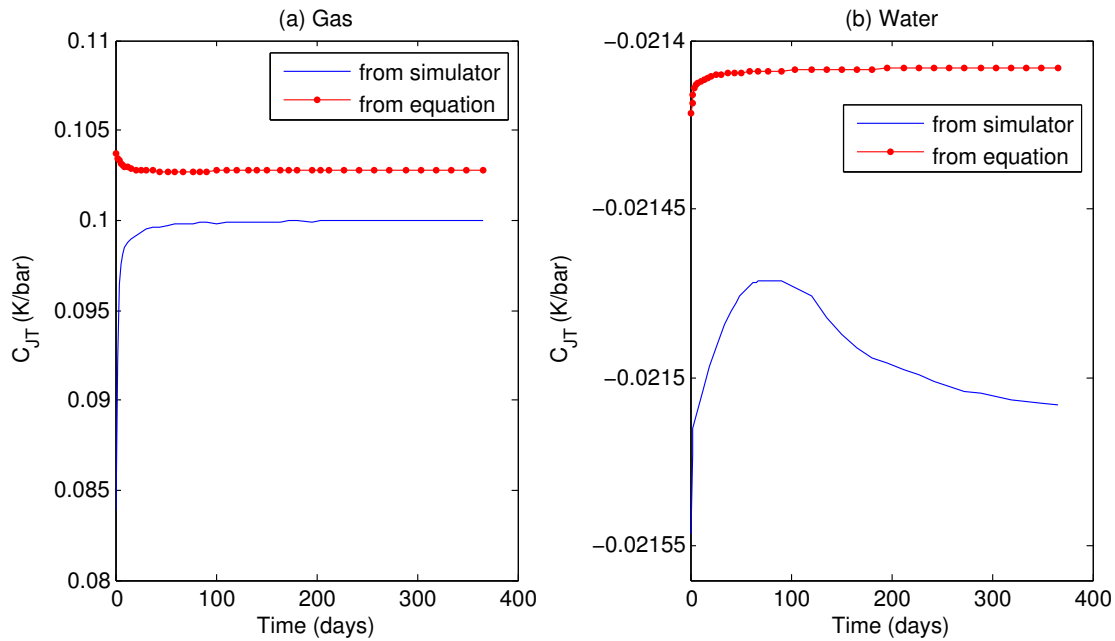


Figure 3.8: Comparison of the Joule-Thomson coefficient from the simulator and from EoS equations for single-phase (a) gas and (b) water.

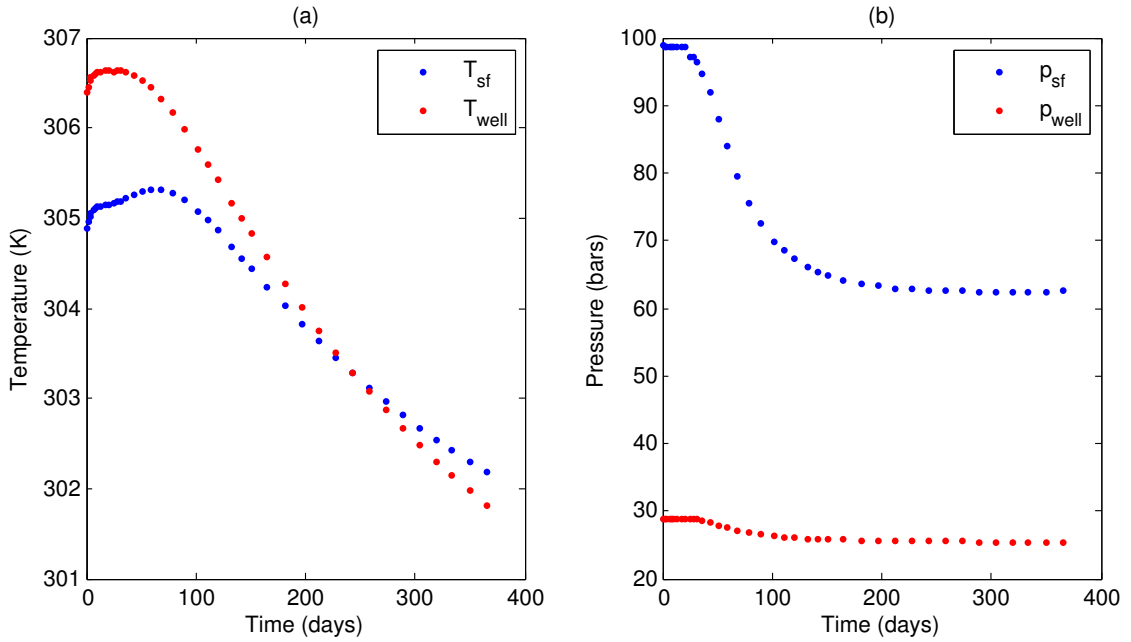


Figure 3.9: (a) Temperature and (b) pressure data as reported at the sandface (T_{sf}) and wellbore (T_{well}) by the simulator for an oil-gas flow.

starting from dry oil production until reaching a gas-dominated flow by the end of the run. Looking at reservoir and well temperature for this case revealed a different behavior than single-phase cases (Figure 3.9a). When oil is the dominating phase in the wellbore fluid, T_{well} is higher than T_{sf} indicating heating effects. The effect is gradually reduced as more gas is produced until reservoir temperature becomes higher than that of the wellbore by the end of the run. The same conclusion cannot be reached by looking solely at the reservoir and well pressures (Figure 3.9b), which makes it difficult to detect gas breakthrough by monitoring only reservoir and well pressures.

With the presumed availability of reservoir and well temperatures and pressures, we proceeded to calculate the gas holdup using Equations (3.10) and (3.11). The outcome from this exercise can be compared with the simulator gas holdup values (represents surface flow meter measurement) from this production segment and results are plotted in Figure 3.10. It can be seen that the gas holdup resulting from this

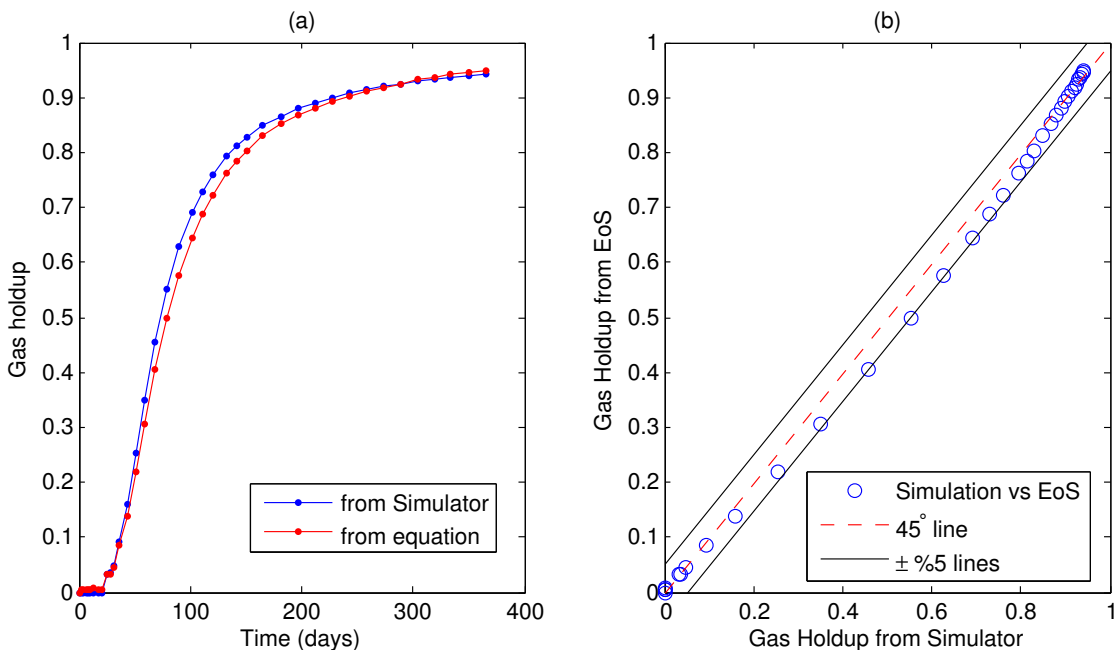


Figure 3.10: (a) Gas holdup solution from the simulation and from our developed C_{JT} equation. (b) Errors from the equation are within $\pm 5\%$ from simulation results.

approach closely follows simulated values. The biggest absolute difference between the two values at any timestep is 5%. This finding was independent of the gas holdup value. Because characterizing high gas production scenarios with DAS was questionable, this result presents an opportunity to rectify the phase fraction calculation in such cases. In the next section, we explore further how integrating temperature with acoustic measurements can help in that regard.

3.3 Integrating DTS with DAS and Applications in Three-Phase Flow

Both of the inflow profiling approaches discussed were capable of characterizing two-phase flow. For three-phase flow, however, we have an underdetermined system as there are more unknowns than equations. For example, in DAS analysis, we are trying

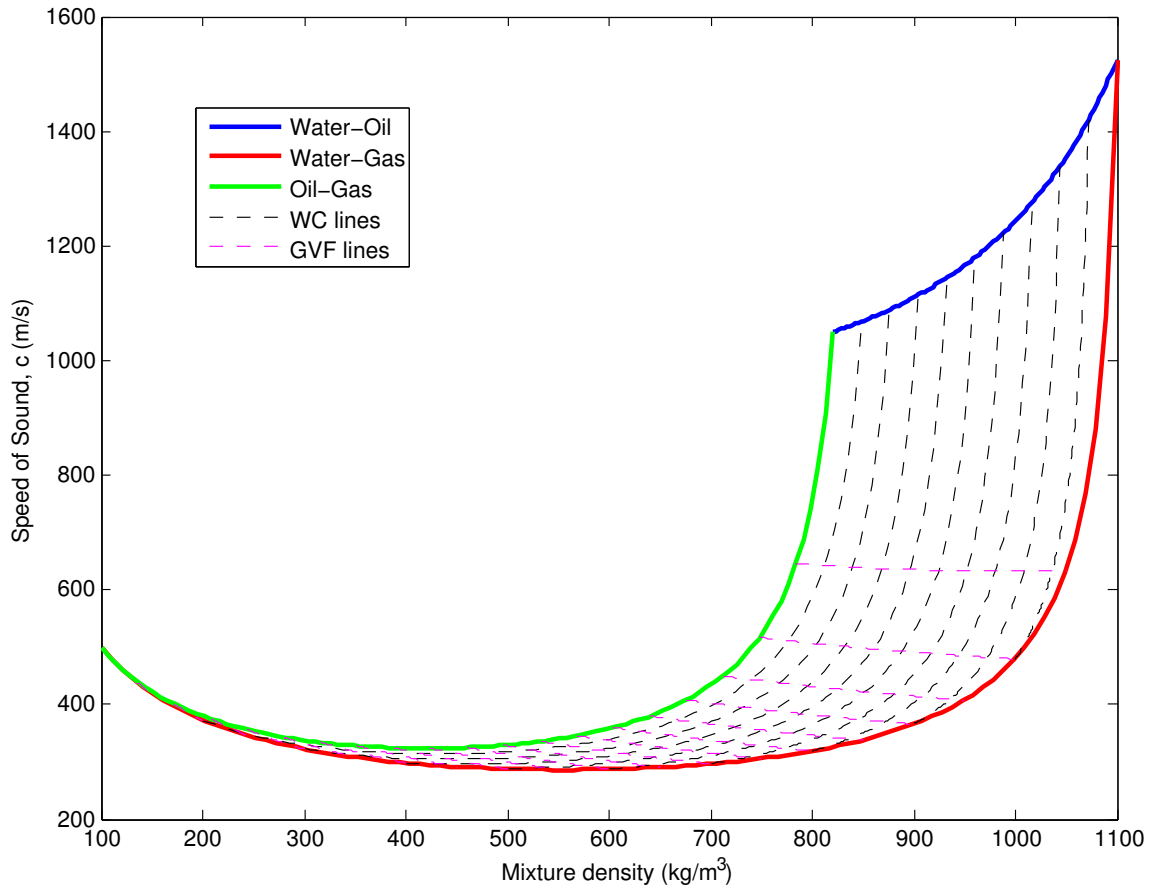


Figure 3.11: Three-phase fluid fractions based on speed of sound in the mixture and fluid density. DAS alone cannot resolve the system requiring an additional reading of water cut, gas holdup, or density.

to solve for the three phase fractions given the mixture speed of sound equation and the summation of the phases equation. Solving such a system, would result in the plot presented in Figure 3.11. For each speed of sound measurement, there is a range of possible solutions enveloped by the two-phase solution at either extreme. An additional water cut or gas volume fraction measurement is required to fully determine the system. However, adding the C_{JT} equation from DTS analysis (Equation (3.9) for three-phase flow) to the speed of sound equation from DAS (Equation (2.10) for three-phase flow) allows to find the three phase fractions by solving the following system of equations:

$$\begin{aligned}
c_m &= \left\{ [\alpha_g \rho_g + \alpha_o \rho_o + \alpha_w \rho_w] \left[\frac{\alpha_g}{\rho_g c_g^2} + \frac{\alpha_o}{\rho_o c_o^2} + \frac{\alpha_w}{\rho_w c_w^2} + \frac{d}{Et} \right] \right\}^{-\frac{1}{2}} \\
C_{JT} &= \frac{\frac{\alpha_g T_{well}}{Z} \left(\frac{\partial Z}{\partial T_{well}} \right)_p + \alpha_o (T_{well} \beta_o - 1) + \alpha_w (T_{well} \beta_w - 1)}{\alpha_g \rho_g c_{p,g} + \alpha_o \rho_o c_{p,o} + \alpha_w \rho_w c_{p,w}} \quad (3.18) \\
\alpha_g + \alpha_o + \alpha_w &= 1 \\
\text{subject to : } & 0 \leq \alpha_g, \alpha_o, \alpha_w \leq 1
\end{aligned}$$

In this section, we present two methods to solve this system of equations. Our aim is to evaluate how rigorous is each method given different fluid mixtures. Because we did not have real data available with both DTS and DAS measurements, we had to rely on reservoir simulation for that purpose. Therefore, hundreds of reservoir simulation runs were performed where the gas holdup and water cut were varied by adjusting fluid contact depths in the reservoir. This allowed us to evaluate the confidence ranges for each method. For each production scenario, the DAS speed of sound measurements were represented with simulator output by considering the produced fluid density and bulk modulus according to Equation (2.7). Likewise, DTS measurements were represented by substituting reservoir and well temperatures and pressures in Equation (3.1). The end result is a solution for the in-situ three-phase fractions as a function of speed of sound and Joule-Thomson coefficient. Table 3.2 summarizes the information needed to complete this exercise and how that information is simulated. Note that α_g is defined as the gas volume fraction (V_g/V_t) while the water cut is the fraction of water volume over liquid volume (V_w/V_l).

3.3.1 Lumping Oil and Water as One Liquid Phase

The first approach we consider to solve Equation (3.18) is to represent the two liquid phases, oil and water, as a single phase. This practice is common in the literature to reduce a three-phase system to two phases. This basically reduces each

Table 3.2: Properties used to solve three-phase flow.

Property	Source	Equation	Simulation Equivalent
Speed of sound	DAS	$c_m = \left\{ [\alpha_g \rho_g + \alpha_o \rho_o + \alpha_w \rho_w] \cdot \left[\frac{\alpha_g}{\rho_g c_g^2} + \frac{\alpha_o}{\rho_o c_o^2} + \frac{\alpha_w}{\rho_w c_w^2} \right] \right\}^{-\frac{1}{2}}$	$c_m = \sqrt{\frac{K_m}{\rho_m}}$
Joule-Thomson coefficient	DTS	$C_{JT} = \frac{\left[\frac{\alpha_g T_{well}}{Z} \left(\frac{\partial Z}{\partial T_{well}} \right)_p + \alpha_o (T_{well} \beta_o - 1) + \alpha_w (T_{well} \beta_w - 1) \right]}{\alpha_g \rho_g c_{p,g} + \alpha_o \rho_o c_{p,o} + \alpha_w \rho_w c_{p,w}}$	$C_{JT} = \frac{T_{well} - T_{res}}{P_{well} - P_{res}}$

equation in Equation (3.18) to its two-phase counterpart, which were presented previously as Equation (2.10) and Equation (3.9) for the mixture speed of sound and Joule-Thomson coefficient, respectively. The following steps summarizes this solution method:

1. Treat oil and water as a single liquid phase, $\alpha_l = \alpha_o + \alpha_w$.
2. Calculate average liquid properties according to the property's mixing rules. For example, arithmetic average is used for density; harmonic average is used for the bulk modulus; and mass-weighted average is used for the specific heat:

$$\rho_l = \frac{1}{2}(\rho_o + \rho_w)$$

$$K_l = \left(\frac{1}{2K_o} + \frac{1}{2K_w} \right)^{-1} .$$

$$c_{p,l} = \frac{\rho_o c_{p,o} + \rho_w c_{p,w}}{2\rho_l}$$

3. Replace α_l with $1 - \alpha_g$ and solve for the gas volume fraction using equation Equation (3.10).
4. Now that the gas volume fraction is known, use the mixture speed of sound expression in Equation (3.18) to estimate α_o and α_w .

Let us refer to this procedure as Lumping 1. Another variation of this procedure,

Lumping 2, was performed by switching the order of steps 3 and 4. In Lumping 2, α_g was found first from the mixture speed of sound equation; then, this value was substituted in the Joule-Thomson effect equation to find α_o . Absolute phase fraction errors resulting from the two variations are plotted in Figure 3.12 as a function of gas volume fraction and water cut. Figure 3.12a and Figure 3.12b show that starting with temperature information to deduce the gas phase fraction only works for high gas holdup values. This is because the cooling effects of gas entry to the wellbore becomes dominant only for high gas flow. The error distribution for Lumping 2 shown in Figure 3.12c, is quite different. The method is more accurate overall but it fails in gas volume fraction values between 0.45 and 0.65 for this particular mixture. Looking back at Figure 2.9, this finding must be related to the flat speed of sound region within this range when gas is present; a measurement of the mixture speed of sound is insufficient to distinguish exact gas phase fraction. The errors in the oil phase fraction shown in Figure 3.12d are inherited and amplified from the gas phase fraction.

3.3.2 Solving the System of Nonlinear Equations with Least Squares

Another more direct solution is to approach Equation (3.18) as an optimization problem. To that end, the least squares with trust region reflective Newton algorithm was employed to find a solution $(\alpha_g, \alpha_o, \alpha_w)$ that minimizes the residual of the system of nonlinear equations. After the simulator outputs speed of sound and C_{JT} values for each fluid mixture, a random initial guess was provided to the optimization algorithm. Figure 3.13a and Figure 3.13b show absolute errors from the least squared optimizer relative to the simulation phase fractions. Errors are reduced in most gas holdup and water cut ranges except when the former values are between 0.35 and 0.6. From the two-phase solution, we know this is the region of high nonlinearity in the speed of sound equation. In those high error areas, it is clear that the optimizer got stuck in a local optimum. Such a plot helps to identify regions where we have an indeterminate system.

This issue can be alleviated by providing the optimizer with some information about the initial guess instead of selecting it randomly. In a real production case, this information can include historical production data or simulation results. For this study, however, we achieved this by selecting the converged solution of the nearest gas holdup and water cut combination as an initial guess. Result improvements from this modification are illustrated in Figure 3.13c and Figure 3.13d. The maximum observed absolute error for this case was below 0.04.

To close discussion of this section, we show that a reasonable solution can be obtained from the first three solution methods: Lumping 1, Lumping 2, and the uninformed least squared method (assuming no prior knowledge about the flow). Figure 3.14a and Figure 3.14b show the minimum error obtained by any of these three methods. The bottom section of the plot indicates which of the three methods obtains the least error at any given gas volume fraction and water cut range. In general, the plot shows that it is recommended to use the lumping method only when gas volume ratio is high. Performing such an analysis for every well under investigation would be a helpful exercise to determine which solution to use under certain flow conditions.

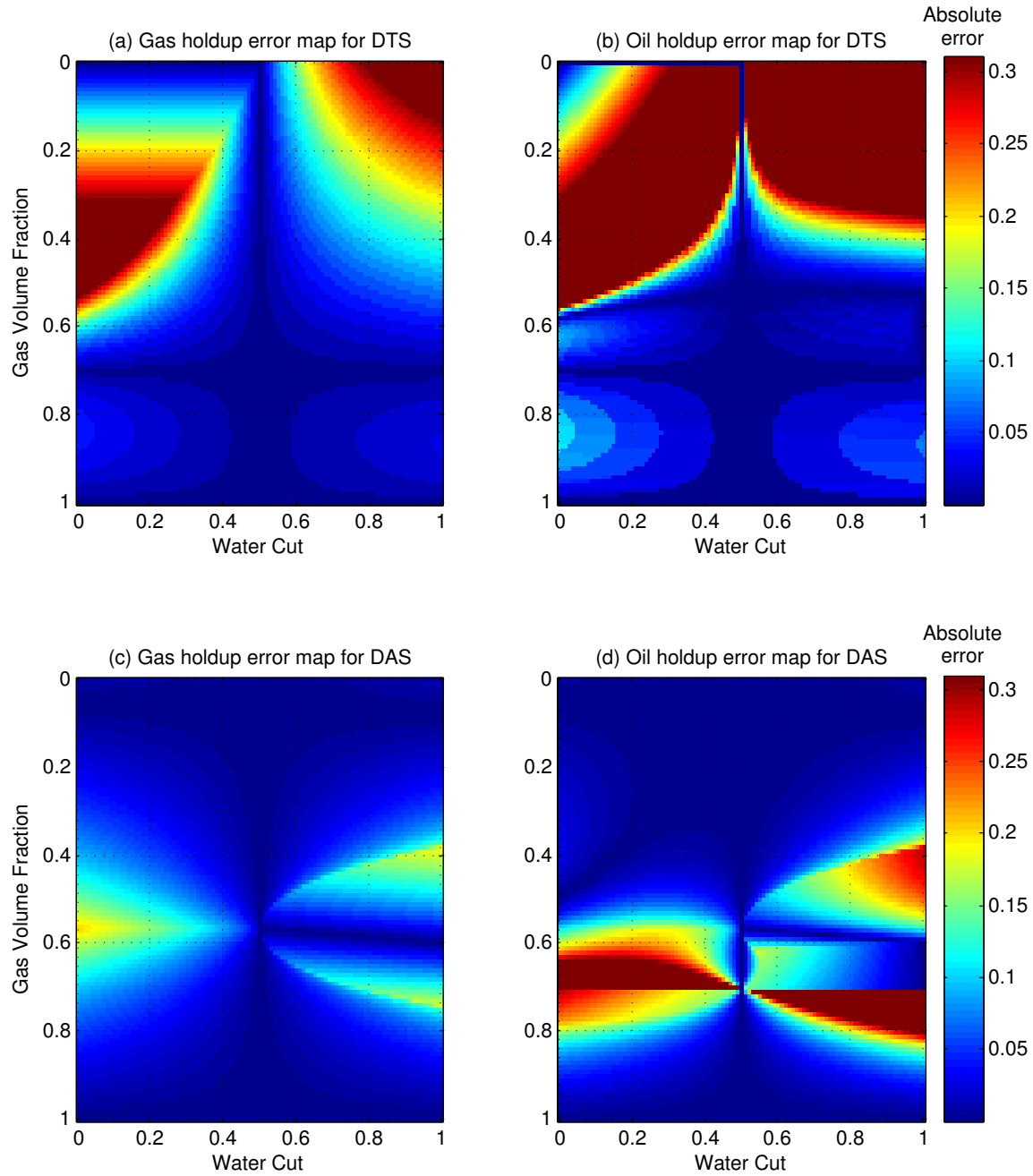


Figure 3.12: (a) Gas and (b) oil holdup absolute errors when the oil and water are represented as one liquid phase (Lumping 1). The same results are presented in (c) and (d) for Lumping 2.

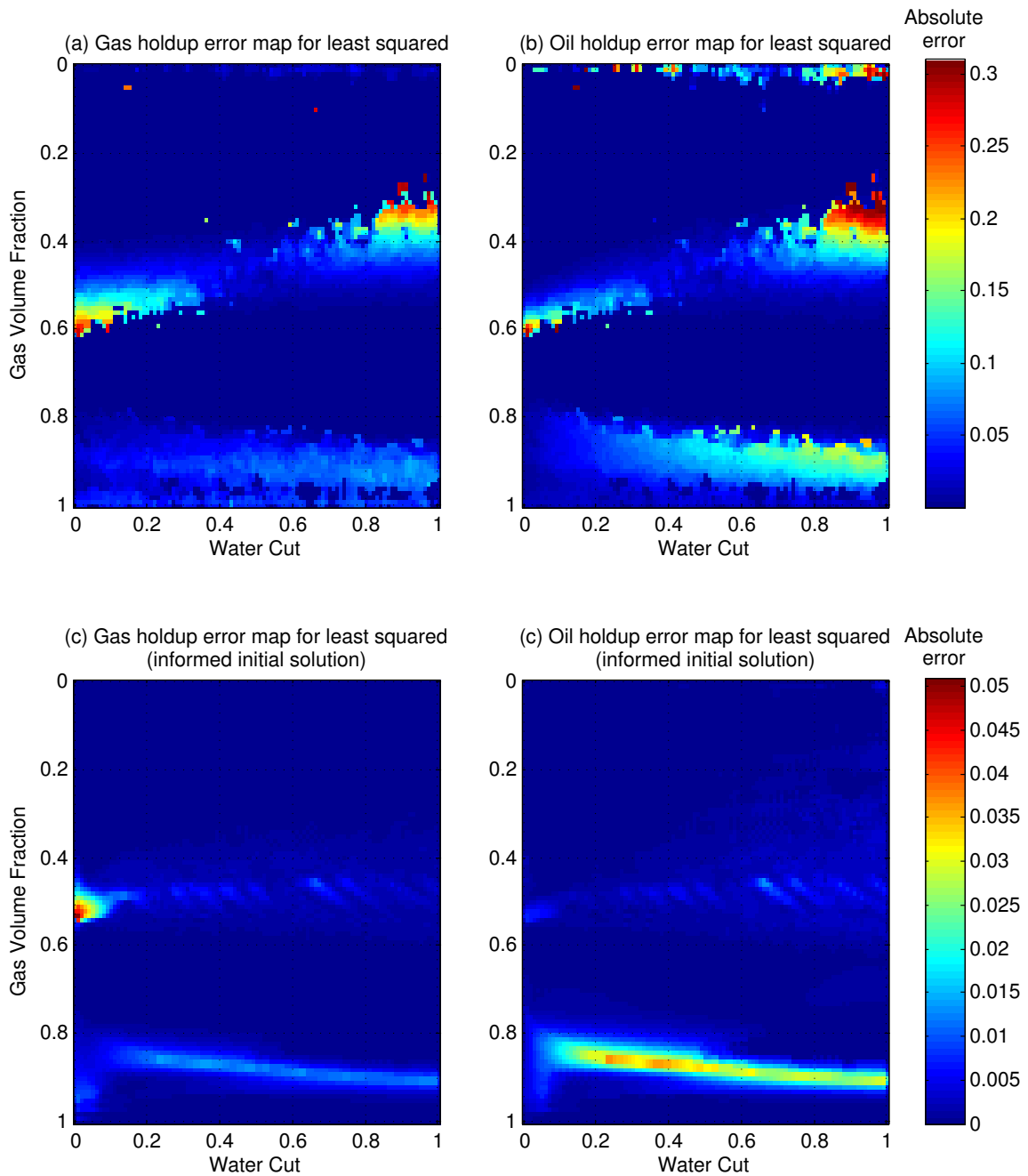


Figure 3.13: (a) Gas and (b) oil holdup absolute errors when solving the nonlinear system of equations using a least squared optimization problem. (c) and (d) show improvement in results when an informed initial solution is specified.

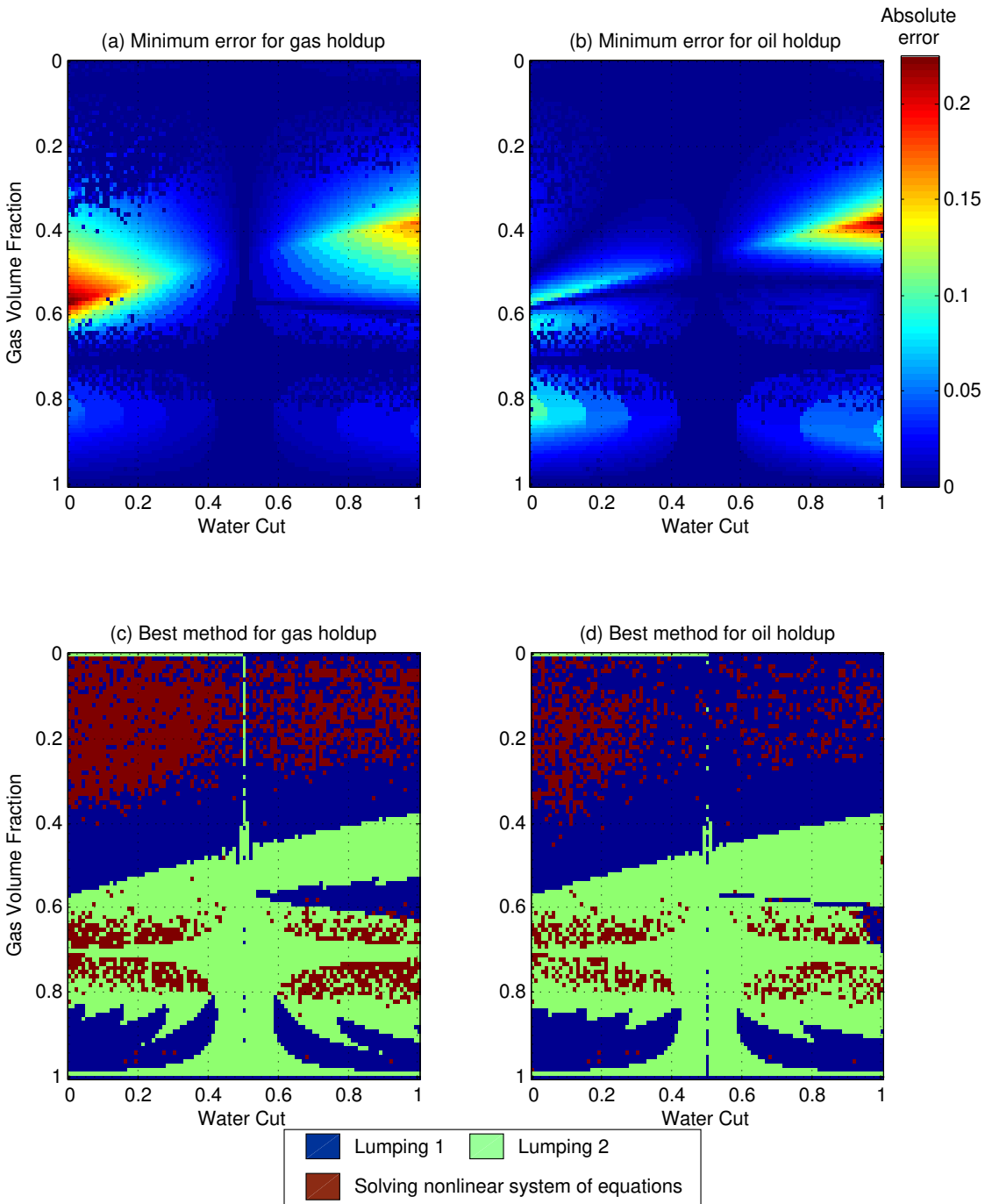


Figure 3.14: Minimum absolute error in calculated (a) gas and (b) oil phase fraction from three proposed solution methods. Lower plots show the most accurate method to get (a) gas and (b) oil holdup.

3.4 Concluding Remarks

The aim of this chapter was to discuss the use of DTS to amend some of the drawback of using DAS for inflow profiling. Improvements obtained by adding temperature measurements to the inflow profiling analysis fall in two main areas. First, temperature helps to determine nonunique gas fraction solutions that DAS suffers from for some gas holdup values. Second, an additional equation is added, which makes it possible to determine in-situ fraction for three-phase flow. Contrary to DAS, producing gas actually helps to solve the DTS equations due to the cooling effect associated with adiabatic thermal expansion of gas (whereas fluids thermal expansion has heating effects). This makes temperature an ideal complement to acoustic measurements to achieve three-phase inflow profiling.

These improvements were accomplished by deriving an equation of state expression for the Joule-Thomson coefficient. Moreover, a simple well completion configuration was suggested to capture a measurement of the coefficient through temperature and pressure drops between the reservoir and the wellbore. Through thermal reservoir simulation, the general solutions for this equation were found for a wide range of gas and oil fractions in the mixture. The two-phase solution was accurate for all gas production ranges. Different methods were suggested to attain solutions for three-phase flow with minimal error using DAS and DTS.

This analysis concludes discussion of inflow profiling in this work. The focus of the next chapter will be the incorporation of the continuous flow profiling technique in production optimization. We should note that results from the DAS and DTS inflow profiling consist of fluid phase fractions and the total flow rate. Meanwhile, the optimization technique discussed next assumes the availability of individual downhole phase flow rates. To bridge this gap, an implementation of a drift-flux model or other mechanistic models might be needed. Although the deployed optimization methods would work efficiently to maximize the oil-cut or reduce fractions of water and gas, it is often more intuitive to work with the individual phase flow rates.

Chapter 4

Application in History Matching and Production Optimization

In general, optimization solvers seek to minimize a cost function or maximize system performance as predicted by a specific simulation model, subject to a set of constraints on the input variables. Such optimization involves an iterative and automated processes of tuning of the input variables, executing the simulator, evaluating performance objectives, then adjusting the system parameters. For that purpose, we built an interface between an optimization algorithm and a reservoir simulator as depicted in Figure 4.1. The data preprocessing step involves converting the tuned input parameters into an input file that can be read by the simulator. Once the simulation is performed, we postprocess its output and tabulate the results in an easy to visualize way.

The objective of the study discussed in this chapter was to investigate the benefits of using distributed downhole measurements to calculate downhole inflow rates in smart wells. This was examined for two main applications: history matching and well control production optimization. For each application, we begin by explaining how the process is enhanced when downhole measurements through DAS and DTS are available. Then, we show several examples to assess improvements attained for each application when distributed measurements are used compared to conventional

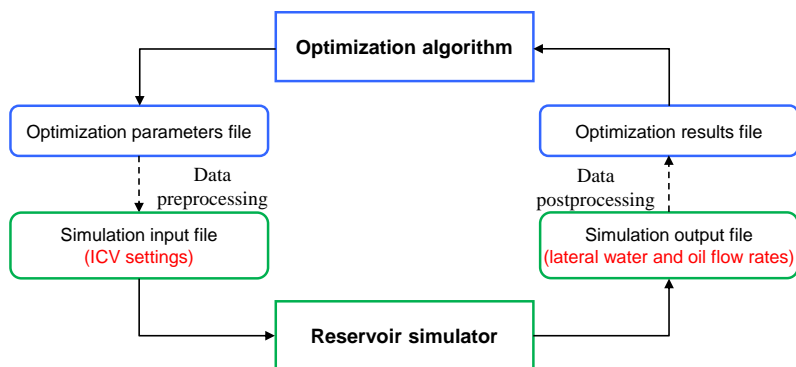


Figure 4.1: The interface between the optimization algorithm and the reservoir simulator.

surface measurements. First, we shed light on the optimization engine used to perform these studies.

4.1 The Main Optimization Engine

In the examples discussed in this chapter, a continuous Genetic Algorithm (GA) (Abukhamsin, 2009) was used for optimization. The GA is a stochastic and heuristic search technique based on the theory of natural evolution and selection. The basic idea revolves around survival of the fittest and solutions are evolved through mating (information exchange) of the best performing solutions. Evolution of the best solution is achieved through three main operators: selection, crossover, and mutation. The operators' role in advancing the solution between iterations is depicted in Figure 4.2. As shown in the figure, the GA process constantly discards low performing solutions to reduce the probability of using their properties their properties in subsequent iterations.

This was our optimization algorithm of choice due to the following reasons:

- The algorithm can be easily parallelized because individual solutions in the iteration can be evaluated separately.
- The search for the optimum is geared towards finding the global optimum as

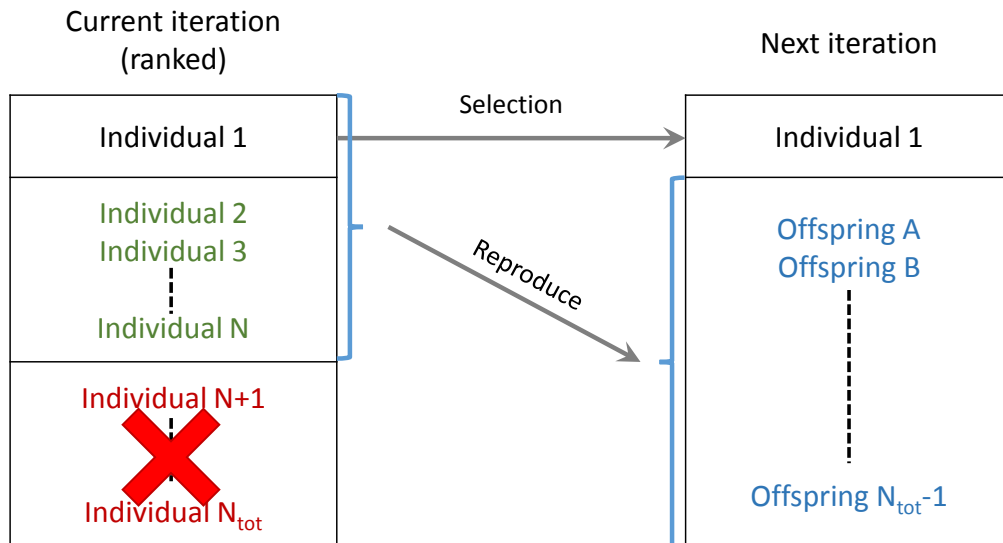


Figure 4.2: Reproduction procedure in GAs.

the algorithm does not get trapped easily in local optima. This is due to using an initial population that is composed of multiple solutions, which provides the opportunity to explore more of the search space (Temizel et al., 2014).

- GAs perform well in problems where the fitness function is complex, discontinuous, noisy, changes over time, or has many local optima (Holland, 1992).
- The algorithm is capable of manipulating many parameters simultaneously.
- No gradients are required during the optimization process.
- The algorithm can be customized easily to fit different applications.

On the downside, genetic algorithms suffer often from premature convergence. This was not significant in the cases studied as the search space is limited to the range of feasible valve settings. To rectify this issue, several optimization runs were performed for each case studied. Another drawback is the algorithm's high computational intensity, which can be addressed by developing accurate proxies as discussed in Section 4.5.

Details of the algorithm were explained in our previous work in Abukhamsin (2009) and we give an overview here. In selection, a few of the best performing solutions are kept for the next iteration. This ensures that every new iteration is at

least as good as the previous one. Also, a fraction of the top-performing solutions in each iteration (dictated by the selection fraction) is selected for the pool of potential parents in the next iteration. Crossover provides the main mating mechanism by which improved solutions are created. This operator is designed such that an efficient information exchange and inheritance is achieved between subsequent iterations. In the continuous variation of GA, this is performed by the following equation (Radcliffe, 1991):

$$P_{new}^i = \eta P_{old1}^i + (1 - \eta) P_{old2}^i, \quad 0 \leq \eta \leq 1, \quad (4.1)$$

where P_{new}^i is the i^{th} variable in a new individual, and P_{old1}^i and P_{old2}^i carry the property values of the same variable from the mother and father individuals. η is a blending coefficient that keeps new property value between property value of its parents.

The last operator is mutation, which is responsible for an occasional alternation of the fit solutions to explore other parts of the search space or to avoid entrapment into local optima (Mitchell, 1996). Mutation is applied to some solutions according to a small predetermined probability and can be represented with:

$$P_{new*}^i = P_{new}^i + \sigma N(0, 1), \quad (4.2)$$

where P_{new} and P_{new*} are the property values before and after mutation, respectively. N is a random number with standard normal distribution, and σ is the standard deviation of this property in the current iteration. The added value is scaled by the standard deviation of the current property to make sure mutated properties do not exceed their feasible range.

The three operators described above are responsible for what is referred to as the reproduction procedure in GAs. The overall optimization loop is shown in Figure 4.3 and is summarized by the following steps:

1. Define the control parameters and identify their feasible limits.
2. Create a diverse pool of possible initial solutions, which honor parameter limits and cover the entire solution space.

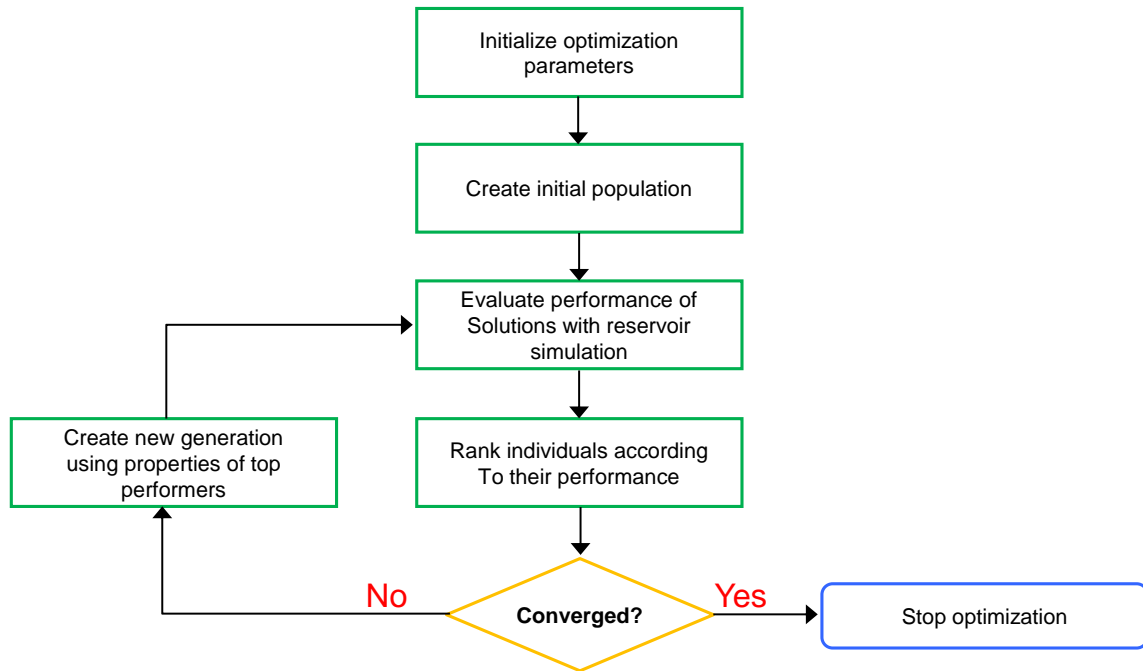


Figure 4.3: Flowchart of the overall optimization procedure using GAs.

3. Evaluate the objective function for each of these solutions, which should be a reflection of the solution quality.
4. Rank the current population according to the value of the objective function.
5. Check for convergence. In this work, a maximum number of iterations was used as a convergence criterion.
6. Apply reproduction operators described in the previous section to the current solution population.
7. Repeat steps 3-6. The best performing solution after convergence is declared as the optimum solution

Before applying the algorithm to more complicated problems, the sensitivity of different genetic algorithm parameters on the optimum solutions was tested on a small scale problem (discussed later in Section 4.3.1). The testing procedure was similar to that presented in Abukhamsin (2009). For these examples, we used a selection fraction and mutation probability of 0.8. The mutation probability was 0.1 for the

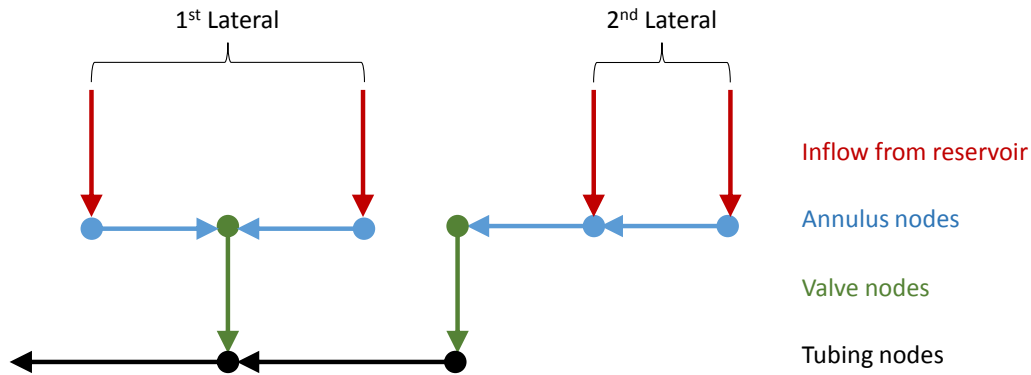


Figure 4.4: Representation of the different nodes in the multi-segment network model.

first half of optimization and 0.05 for the later half. This allows for more exploration and modification on prior solutions in the earlier stages of the run. The size of initial population was varied depending on the number of optimization parameters. To cover more of the solution space, a large initial population was evaluated first. Then, we proceeded with the top performing half of this population for subsequent iterations.

4.2 Modeling Inflow Control Devices

Because the smart well optimization problem involves frequent changes in ICV settings, accurate valve representation is required in all performed reservoir simulations. This is achieved with the multisegment well model in ECLIPSE. In this model, the flowing conditions of the fluid within the well are determined by dividing the wellbore into a number of one-dimensional segments. Each segment has its own set of independent variables to describe the local fluid conditions. The segments are connected by nodes to form a segment network as shown in Figure 4.4.

The inflow into each valve is dictated by the total pressure drop across the valve,

which is given by (GeoQuest, 2013):

$$\Delta p_{ICV} = \Delta p_c + \Delta p_f = \frac{\rho_m q_m^2}{2A_c^2 C_v^2} + 2f \frac{L}{D} \rho_m q_m^2 A_p^2, \quad (4.3)$$

where the two pressure components Δp_c and Δp_f refer to the constriction and frictional pressure drop, respectively. A_c and A_p are the cross-sectional areas of the constriction and the pipe, q_m is the volumetric flow rate of the fluid mixture, f is the Fanning friction factor, and C_v is a dimensionless flow coefficient for the valve geometry. When solving the reservoir pressure equation, the general sink/source term is modified to:

$$q = PI(p_{res} - (p_{well} + \Delta p_{ICV})), \quad (4.4)$$

where PI is the productivity index for that well.

4.3 Production Optimization in Smart Wells

In this section, we present the general setting of the production optimization problem by adjusting smart well control. Generally speaking, optimization problems search for the set of variables, x , that achieves a maximum objective function according to the following equation:

$$\begin{aligned} F(x_{opt}) &\geq F(x) \text{ for all } x \in \Omega \\ \text{Subject to } LB &< C_n(x) < UB \end{aligned} \quad (4.5)$$

Here, Ω symbolizes the search space domain, C_n corresponds to the problem constraints defined by upper and lower bounds, and F stands for the objective function we are trying to optimize. For the well control optimization problem, x_{opt} contains the ICV setting of all valves in the smart wells. The objective function is usually cumulative oil production but can also include economic implications by considering the Net Present Value (NPV) of the project. In history matching cases, the objective

function is the mismatch between production from the true model and the model realization. To accommodate the stochastic nature of the algorithm, each optimization example is repeated three times and the case with the maximum objective function is reported.

Smart wells have an apparent advantage over horizontal well in terms of improving reservoir sweep efficiency and delaying water breakthrough as examples in this section will demonstrate. To investigate this, we started with a simple single-phase reservoir model, which has four homogeneous permeability zones. This helped to build intuition on the behavior of the optimizer. Then, we introduced two phases in the model to investigate how downhole control enhances production recovery.

4.3.1 True Optimum Search Test

This first example case was set up such that the optimal answer was known beforehand to test the ability of the optimizer in determining the true answer. The reservoir model includes four homogeneous permeability zones as shown in Figure 4.5. Other model and fluid parameters used in the example are listed in Table 4.1. There is a single horizontal oil producer in the middle of the top layer of the model with pressure support from an underlying aquifer. The well is segmented into four production zones, where an ICV controls production in each different homogeneous permeability zone. The objective function is initial oil inflow rate (fluid outflow performance is not considered). Since the well starts producing single-phase oil with no interference between the zones, the fluid inflow into the well is maximized by maximizing the drawdown pressure between the wellbore and the reservoir. This is achieved by fully opening all the valves.

Each of the four control variables can hold 11 values between 0% (fully-closed ICV) and 100% (fully-open) at 10% increments. The optimization started with a randomly generated initial population of 20 individuals and was stopped when no improvement was achieved in the objective function for five consecutive iterations. The fully-open and true optimum for this example yielded a flow rate of 5,056 BBL/d.

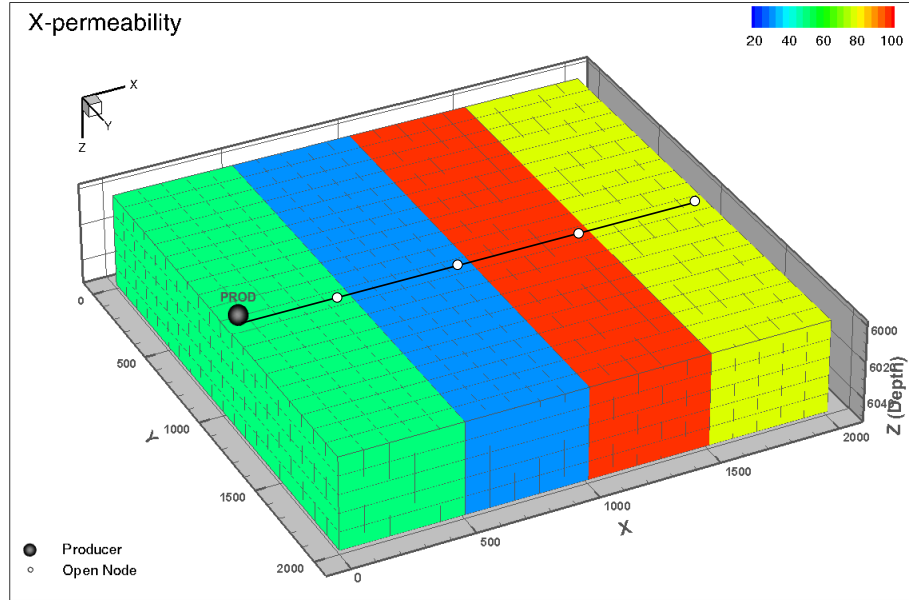


Figure 4.5: Permeability of the reservoir model used for the well control optimization example.

Table 4.1: Reservoir and fluid parameters for the well control optimization example.

Property	Value
Grid size	$20 \times 20 \times 5$
Grid cell dimension	100 ft \times 100 ft \times 10 ft
Porosity	20%
Initial pressure (p_i) at datum	2,000 psi at 6,000 ft
Initial temperature	180 °F
ρ_o and ρ_w at p_i	40 and 63 lb/ft ³
μ_o and μ_w at p_i	0.60 and 0.36 cp
S_{or} and S_{wi}	0.18 and 0.0
Production BHP	1,000 psi

As shown in Figure 4.6, all three optimization runs reached the true optimum value in less than 22 iterations. An average of 342 simulations per optimization run was required to reach the optimal answer. Although not needed in this case, an exhaustive search would have required 14,641 (11^4) simulations had the optimum not been known. As such, only about 2% of all possible ICV combinations were evaluated by the algorithm before reaching the optimum solution.

Table 4.2 shows the ICV settings of the best performing individual in each iteration, which gives an insight of the solution progression. It should be noted that solutions for higher permeability zones are found faster because the objective function has higher sensitivity to their settings. When the production profile is plotted for the horizontal well as shown in Figure 4.7, it is observed that the flow rate from each zone is proportional to the permeability of that zone. With that point in mind, we tried to optimize oil recovery in the presence of water in the next example.

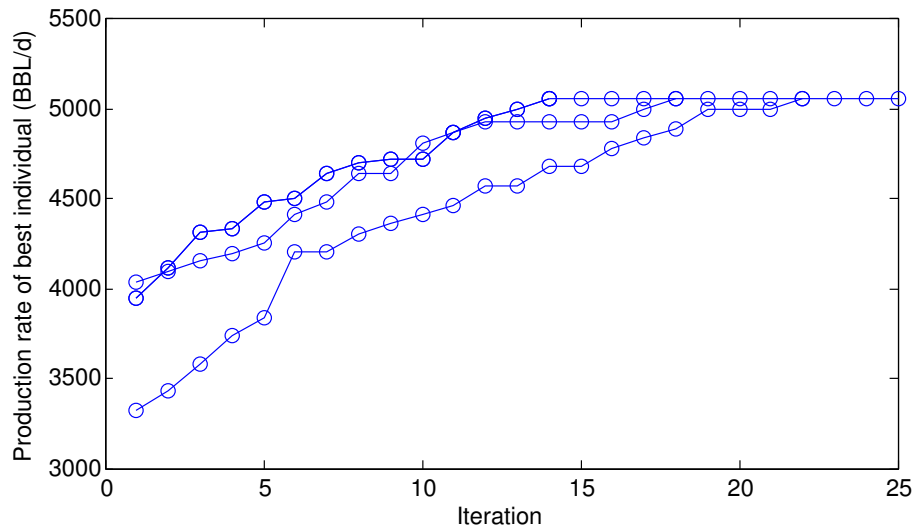


Figure 4.6: Progression of the objective function fitness for three different optimization runs. On average, the true optimum was found after 18 iterations.

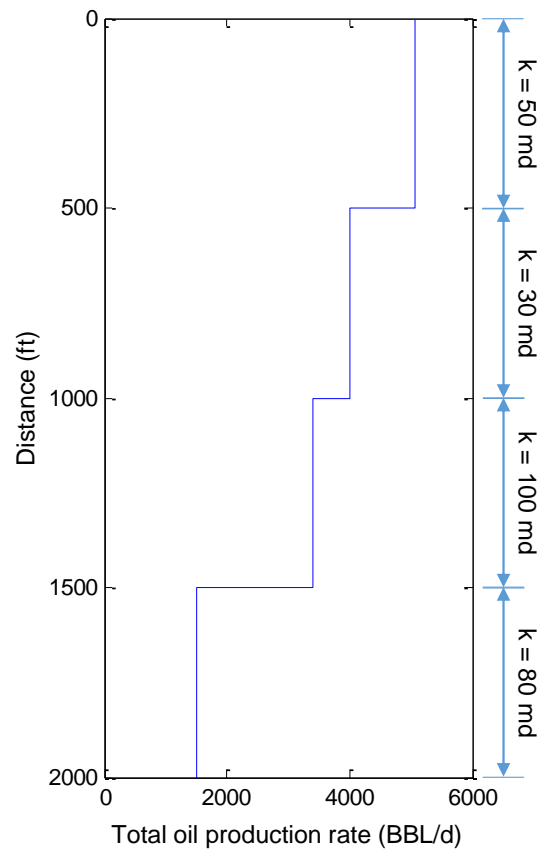


Figure 4.7: The well flow profile for the optimum solution. Production from each zone (incremental total production rate) is proportional to the zone's permeability.

Table 4.2: ICV setting of each zone as the optimization run progressed.

Iteration	1	2	3	4	5	6	7	8	9	10	11	12	13	14
ICV 1 (50 md)	0.6	0.7	0.7	0.8	0.8	0.9	0.9	0.9	0.8	0.8	1	1	1	1
ICV 2 (30 md)	0.6	0.6	0.6	0.7	0.6	0.7	0.6	0.7	1	1	0.7	1	0.9	1
ICV 3 (100 md)	0.9	0.9	1	0.9	1	0.9	1	1	1	1	1	1	1	1
ICV 4 (80 md)	0.7	0.8	0.9	1	1	1	1	1	1	1	1	0.9	1	1

4.3.2 Maximizing Oil Recovery in Two-Phase Flow

Withdrawing the most liquid from a zone does not necessarily lead to optimal production in two- and three-phase flow. Early water breakthrough might leave behind bypassed oil zones. Moreover, the presence of water in the production tubing increases the hydrostatic head, which could negatively impact oil production. In this example, we investigated these effects by moving the oil producer to one end of the reservoir and adding a water injector on the other end (Figure 4.8a). The producer is completed in the top layer and was modified to have four laterals. The injector is completed in the bottom layer and is injecting water at a Bottom Hole Pressure (BHP) of 2,500 psi. All other properties are as listed in Table 4.1.

The objective function for this example was the oil recovery after three years of production. In addition to the fully-open case (Base Case), two optimization cases were tested. In the first case, initial valve settings that maximize recovery were selected as the optimization variables. For the second case, two changes were allowed to occur; one immediately after water breakthrough and another at the beginning of the third year. This increases the number of optimized variables from four to 12. The injector remained fully-open throughout the three years. Again, three runs were performed for each case and results are shown for the best run.

Optimal valve settings are summarized in Table 4.3. To rationalize these results, we also plot the oil saturation map at the end of the run for the three cases in Figure 4.8. The main difference between Case 1 and the Base Case is the restriction

Table 4.3: Summarizing results of the tested optimization cases. In the Base Case, all valves all open throughout productions. Case 1 finds the optimal initial valve settings, while Case 2 finds optimal settings at three different time steps (**1:** initial setting, **2:** at 480 days, and **3:** at 720 days).

Case	Oil recovery (MMBBL)	Optimum valve settings
Base	2.361	[1, 1, 1, 1]
Case 1	2.472	[1, 1, 0.7, 0.8]
Case 2	2.679	1: [1, 1, 1, 1] 2: [1, 1, 0.4, 0.8] 3: [0.6, 1, 0.5, 0.7]

applied to the two highest permeability zones. In effect, this lowered the initial production rate but extended the plateau by 120 days as the water breakthrough was delayed (Figure 4.9). This resulted in 4.7% improvement in the total oil recovery.

However, this case still did not sweep the second production zone (lowest permeability) efficiently. The more dynamic manipulation of ICVs in Case 2 appears to address this issue to some extent. By just applying two ICV changes, the algorithm was able to identify a set of ICV settings to enhance sweep efficiency from the first two zones. This was achieved by initially opening the well at full capacity to attain early high production; then, restrict the high permeability zones to encourage other zones to produce. This adjustment resulted in 8.4% gain over Case 1 and 13.5% over the Base Case. A comparison of the zone flow distribution in the well between the two cases is shown in Figure 4.10. The plot reveals that the valve settings in Case 1 almost equalized production in all the zones to delay the water breakthrough. However, Case 2 results showed that it is optimal (for this particular test) to keep changing the valve settings depending on the waterfront encroachment near the well.

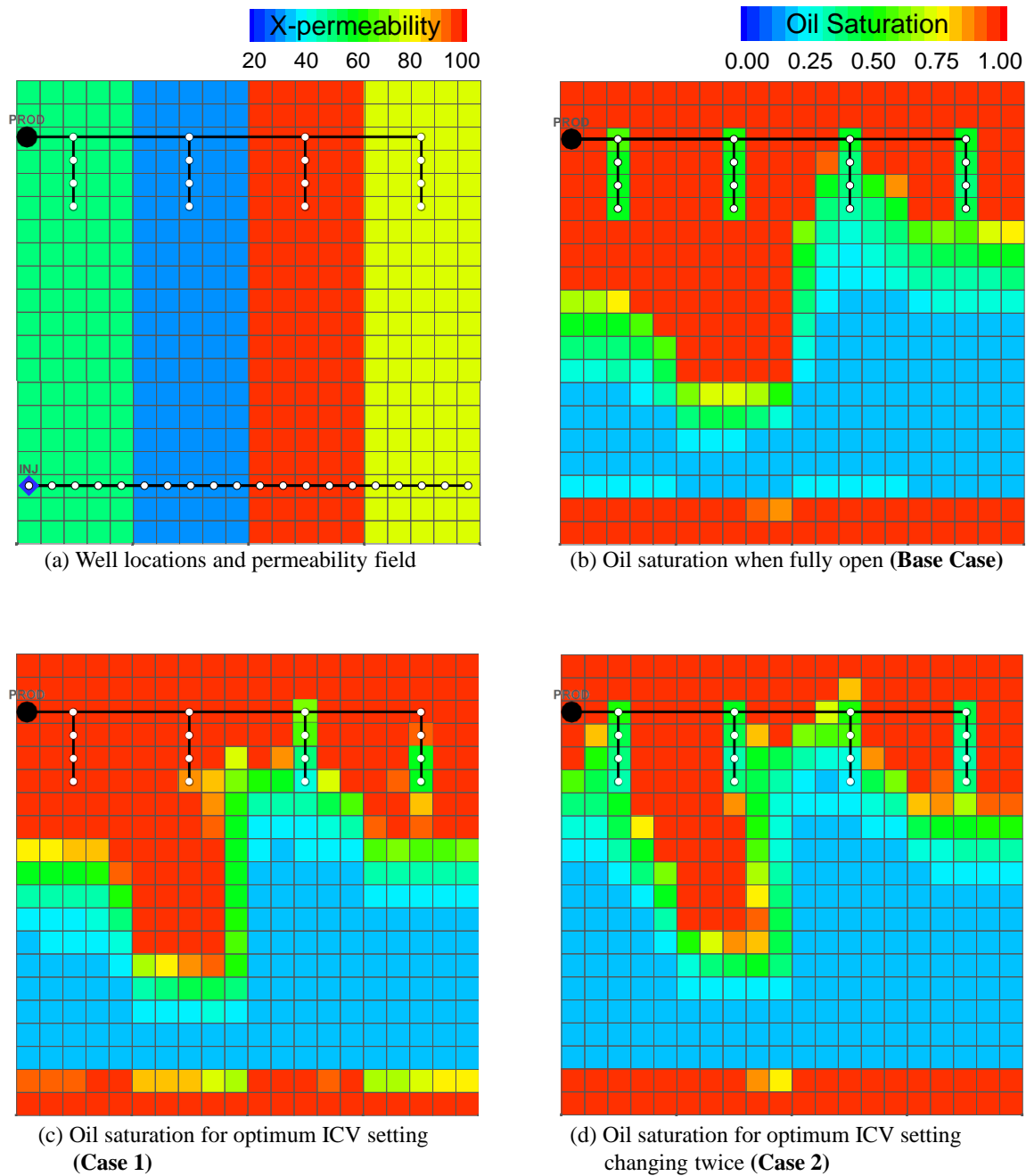


Figure 4.8: (a) Permeability and well locations for the reservoir model. The oil saturation map for the optimum valve setting at the end of simulation for the Base Case, Case 1, and Case 2 are shown in (b), (c), and (d), respectively.

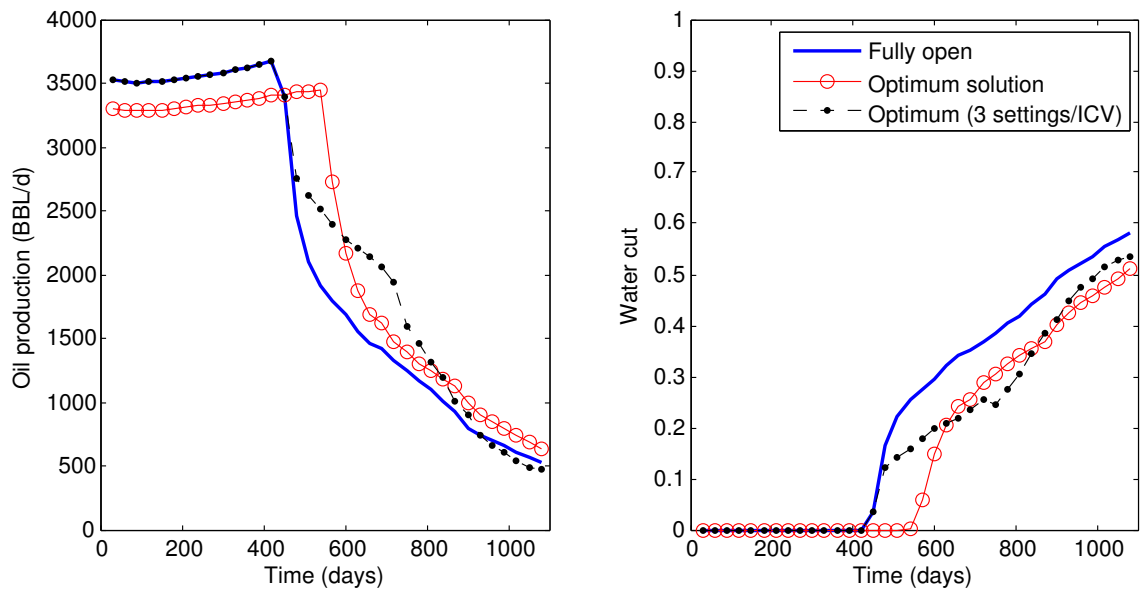


Figure 4.9: Oil production rate (left) and water cut (right) for the Base Case and optimum solution from the two cases.

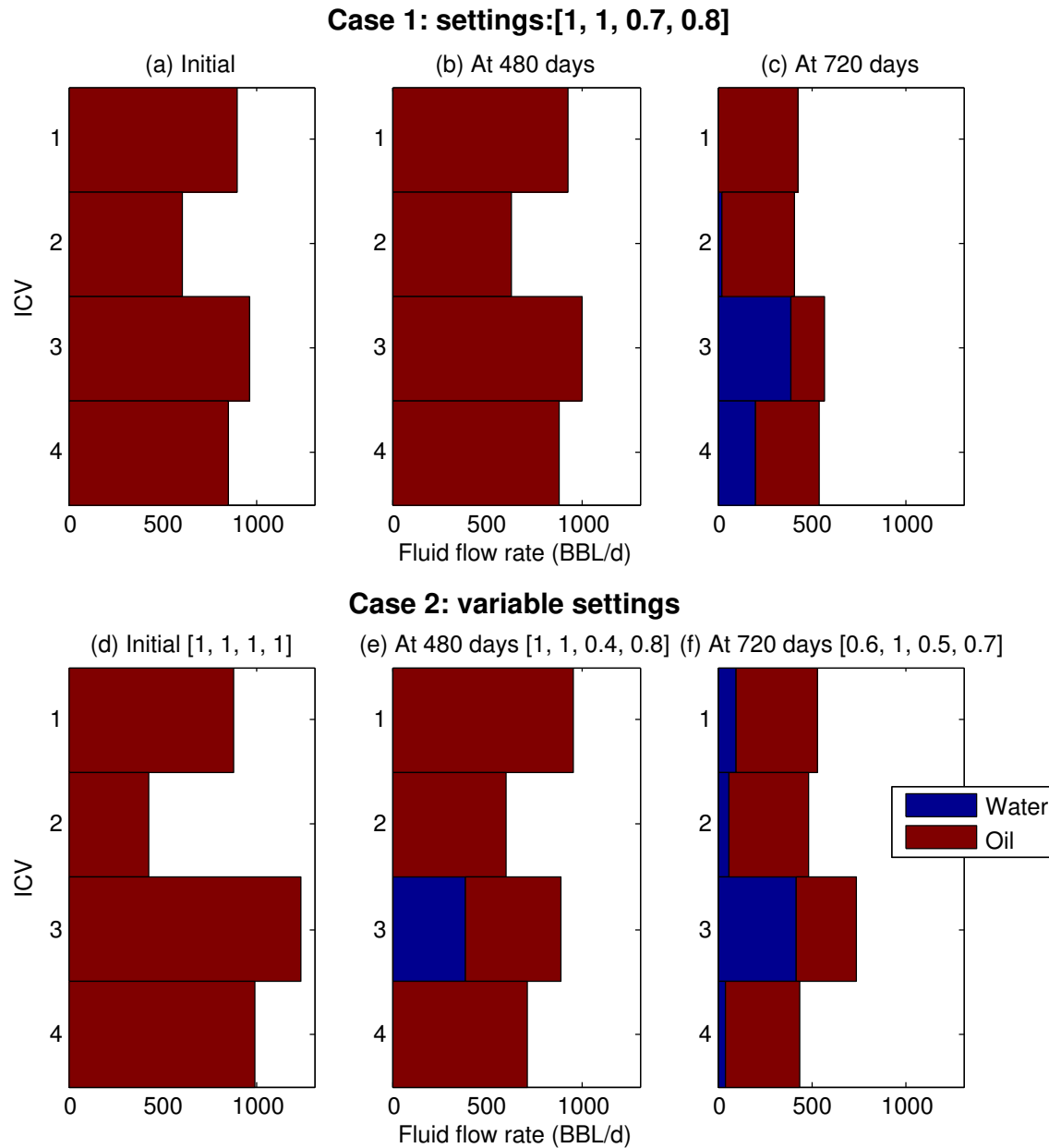


Figure 4.10: Flow contributions from each production zone for Case 1 at three different time steps, (a) the first time step, (b) after 480 days, and (c) after 720 days. The same is shown for Case 2 in (d), (e), and (f).

4.4 Application in History Matching

History matching is a heuristic procedure that involves modifying model parameters such that the model output matches a set of observations. History matching is an ill-conditioned inverse problem as we are trying to estimate a large unknown permeability field by matching few measurements. This commonly results in nonunique solutions, which requires looking at several realizations to reduce uncertainty (Caers, 2003). Increasing the number of measurements provided by distributed measurements would logically reduce the ill-posedness of the problem. In the example described in this section, we tested history matching with the ensemble Kalman filter. The history matching procedure was first performed to find the reservoir permeability field using surface production rate data. Then, the procedure was repeated to include downhole production data that one would obtain from DAS using the analysis in Chapter 2. This allowed us to quantify the gain of using downhole measurements for such applications.

4.4.1 Describing the Kalman Filter

The Ensemble Kalman Filter (EnKF) is a recursive filter, which is suitable for problems with a large number of variables in a dynamic state-space processes. EnKF is a variation of the original Kalman filter, where the covariance matrix is replaced by an ensemble covariance for computational efficiency. By and large, the EnKF is a Monte Carlo implementation of the Bayesian update problem. For each analysis cycle (simulation time step or when new data becomes available), the probability density function of the state of the modeled system (the prior) is subjected to a modified Bayesian update (called the Kalman gain). This update (the posterior) takes into account the prior probability density function and the data likelihood (Evensen, 2009).

For this application, we followed the EnKF implementation described in detail by Duru (2011) and Kitanidis (2012). The procedure starts by defining a linear

correlation between the state of the system and observations as:

$$y = Hx + w, \quad (4.6)$$

where x represents the state of the system and y contains the set of observations. H is called the observation matrix such that Hx would return the value of data in the absence of error. The stochastic white-noise in the data is represented by w , which has zero mean and a covariance matrix R (R is an estimate of error in the data). When a new set of data is available, the new state of the system \hat{x} , is updated as:

$$\hat{x} = x + K(y - Hx), \quad (4.7)$$

where K is the Kalman gain given by:

$$K = QH^T(HQH^T + R)^{-1}, \quad (4.8)$$

and Q is the covariance of the state-variables calculated by:

$$Q = \frac{[x - E(x)][x - E(x)]^T}{N - 1}. \quad (4.9)$$

$E(x)$ here is the mean state-variable of the ensemble and N is the number of members in the ensemble. After each assimilation step, the output of different members of the ensemble is brought closer to the true model as shown in Figure 4.11.

The EnKF procedure was applied to a 30×30 two-dimensional channelized model (Figure 4.12a), which we will refer to as the true model. A single smart oil producer is completed in the middle of the reservoir with four production segments. The well is produced through an aquifer drive mechanism acting on the northern and southern boundaries of the reservoir. Oil and water production data were collected from the four segments each 20 days for 400 days. Three data assimilation cases were investigated. For the Base Case, only the surface oil and water production data were used to update the models at each time step. This should represent current history matching techniques when using the EnKF. For Case 1, downhole temperature data

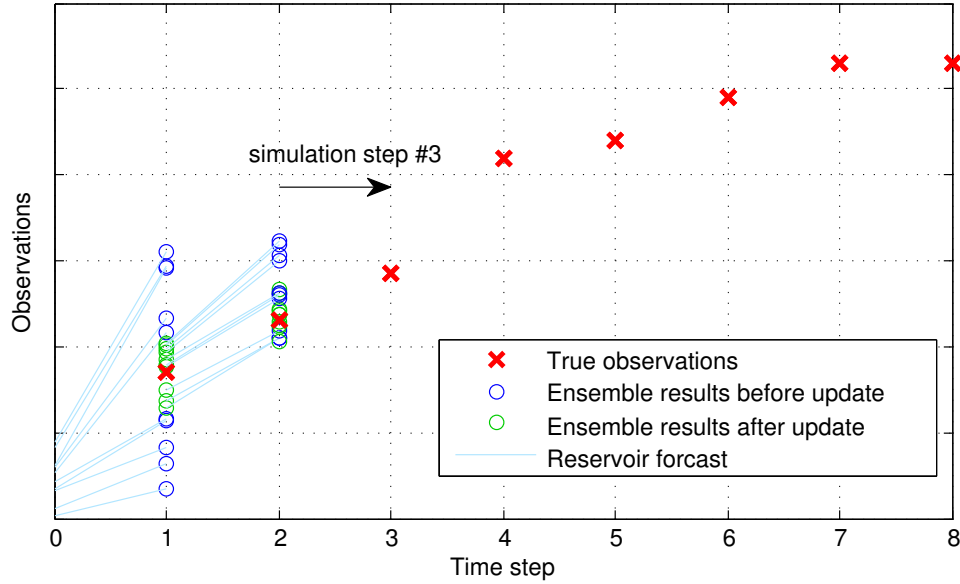


Figure 4.11: Illustrating the effect applying the Kalman update after each simulation step. The ensemble results are brought closer to true observations after each update.

for each segment were added as additional observations. In Case 2, the observations included downhole oil and water production data (from DAS data) from each segment. The procedure is summarized in the following steps:

1. Use a forward model to collect production observations from the true model.
2. Create the ensemble by generating several realizations that honor the geology of the true model. Here, 50 unconditional realizations were created with the Single Normal Equation Simulation (SNESIM) algorithm described in Strebelle (2002).
3. Advance each member of the ensemble to the time of the first true model measurement. Obtain a measurement at this time from all members and fill the prior state vector for that assimilation step. The dynamic state and observation vector, y , of the k^{th} realization in the ensemble is described by:

$$x^k = [\ln(k_1), \dots, \ln(k_N), p_1, \dots, p_N, S_{o1}, \dots, S_{oN}, q_o, q_w],$$

$$y^k = [q_o, q_w],$$

where x contains N (number of grid blocks in model) of each dynamic model parameter including permeability, pressure, saturation, in addition to the oil and water production rates. For Case 1 and 2, temperature and downhole flow data for each well segment are added accordingly.

4. Compute the mean of the state vector for all realizations and the Kalman gain using Equation (4.8).
5. Update the ensemble state vectors using Equation (4.7).
6. Move to the next simulation step and repeat steps 3-5 using the new set of observations.

4.4.2 History Matching Results

Due to the stochastic nature of SNESIM, the mean permeability field of the ensemble became almost homogeneous concealing most features of the true model (Figure 4.12b). After going through 20 assimilation steps over 400 days, the final updated permeability fields for the three cases are illustrated in Figures 4.12c to 4.12e. In all cases, features of the northern part of the reservoir were represented more accurately because there was a direct path connecting the water from the aquifer to the well. There was no such connection in the southern part of the reservoir.

When surface measurements were used as observations in the Base Case, low and high permeability regions started to appear in the reservoir model. Their distribution, however, did not match the true model accurately. Including DTS measurements as part of the EnKF, did not seem to improve the match between the true and history-matched permeability. This might be due to the subtle temperature variation within the different segments as there is no geothermal gradient (horizontal well in a two-dimensional model) or gas production in the reservoir. When downhole flow information (from DAS) was considered, however, there was noticeable improvement in the permeability field match. Some of the channels that match the true model started to appear (indicated by red circles in the true model in Figure 4.12a and the model for this case in Figure 4.12e).

Instead of visual inspection of the permeability fields, another evaluation metric can be obtained by comparing the production profiles of each history-matched case. Figure 4.13 compares the oil and water production performance for the three history-matched cases in addition to the prior unmatched case for all realizations. We note that there is very high variation in oil and water production for the prior realizations as shown in Figures 4.13a and 4.13e. When surface production and DTS measurements are included in the history matching procedure, the production variation is lowered but average production for all realizations is still far from the true production profile (Figures 4.13b, 4.13c, 4.13f, and 4.13g). Improvement obtained by including downhole measurements in Case 2 is demonstrated again by the narrower spread in both oil and water production as shown in Figures 4.13d and 4.13h.

The root mean square error (RMSE), plotted in Figure 4.14, reflects errors associated with each case and is given by:

$$RMSE = \sqrt{\frac{\sum_{i=1}^M \sum_{j=1}^N (q_t^{i,j} - q_m^{i,j})^2}{NM}}, \quad (4.10)$$

where q_t is the true oil or water production rate and q_m is the modeled rate. N and M are the numbers of realization and simulation time steps, respectively. In general, errors were reduced as more data were considered in the history matching process. This is because the problem becomes less ill-posed with a larger observation set. The water production for Case 1 (when DTS was added) was an exception to that rule. This observation is consistent with the work of Duru (2011), which concluded that although the addition of temperature in history matching improves porosity prediction, it has an adverse effect in matching permeability. The implementation of EnKF in this case was relatively straight forward but involved Gaussian assumptions regarding prior models. This can be resolved by the use of geological parameterization techniques in conjunction with EnKF to history match complex geological models (Vo and Durlofsky, 2016).

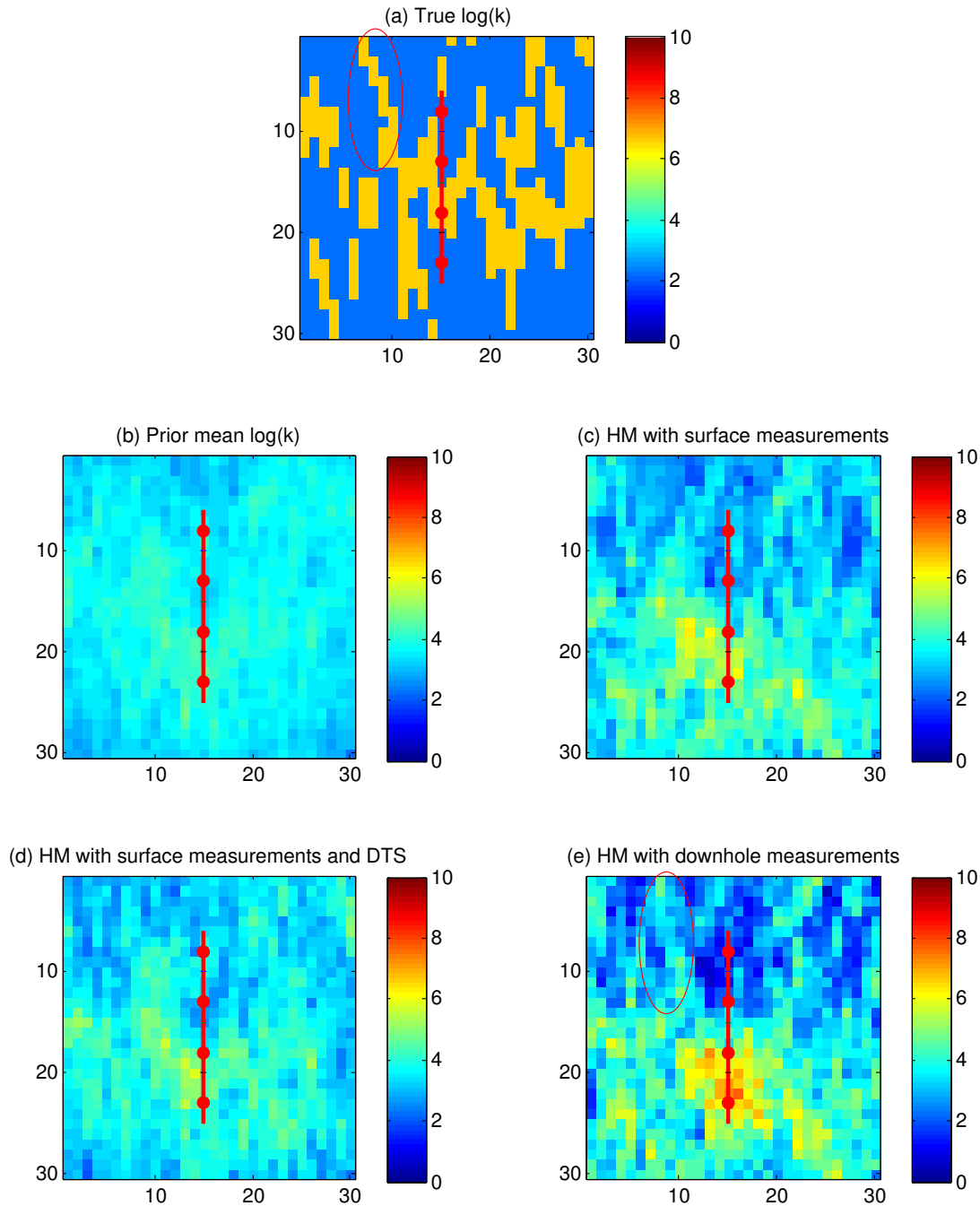


Figure 4.12: (a) The true model permeability logarithm. The prior mean of permeability logarithm is shown in (b). The final history-matched permeability field for the three methods are shown in (c), (d), and (e).

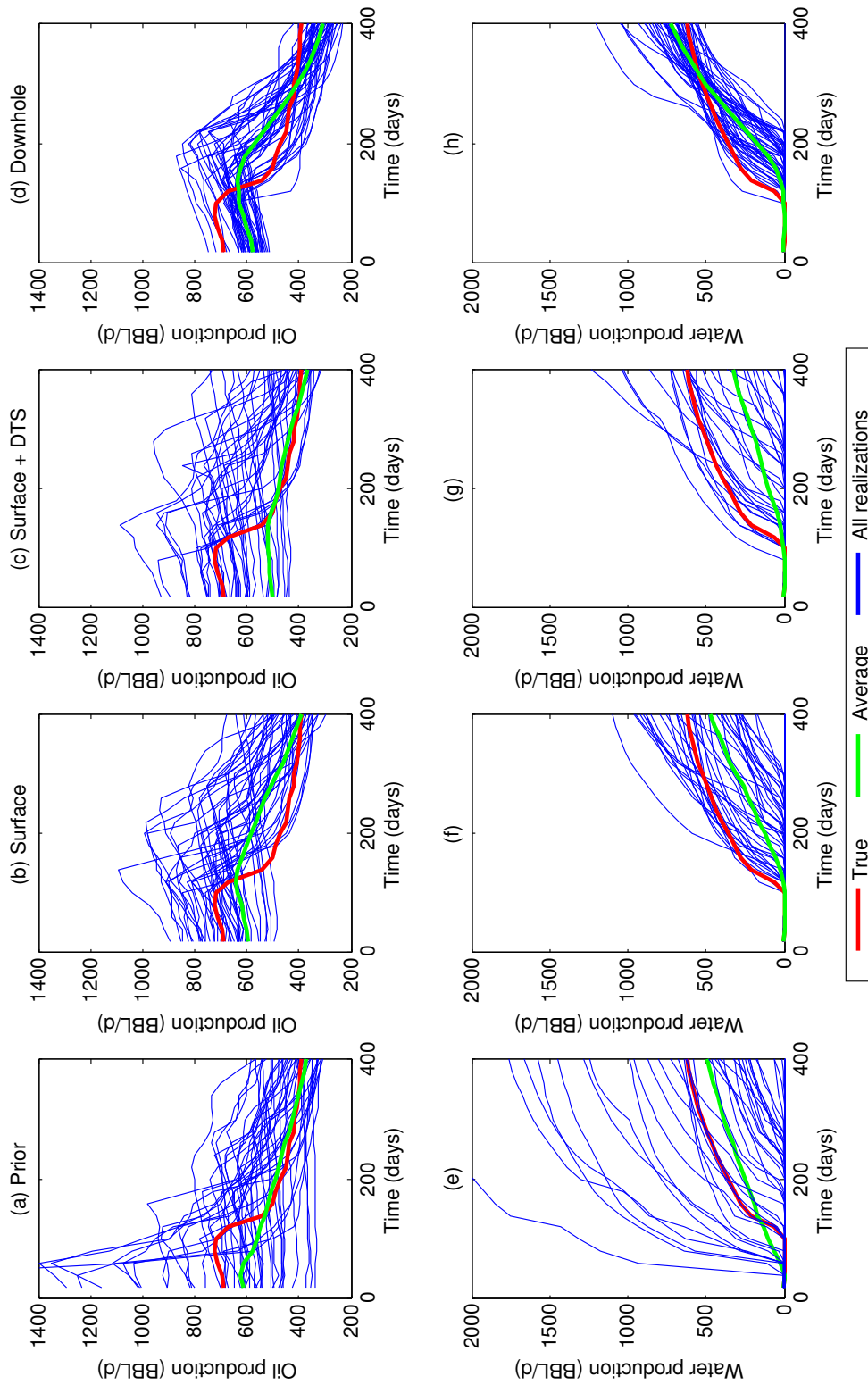


Figure 4.13: Oil (a through d) and water (e through h) production rates for all realizations for the prior models and the three history matching cases. The true production rate is shown in red, while the average production rate from each case is plotted in green.

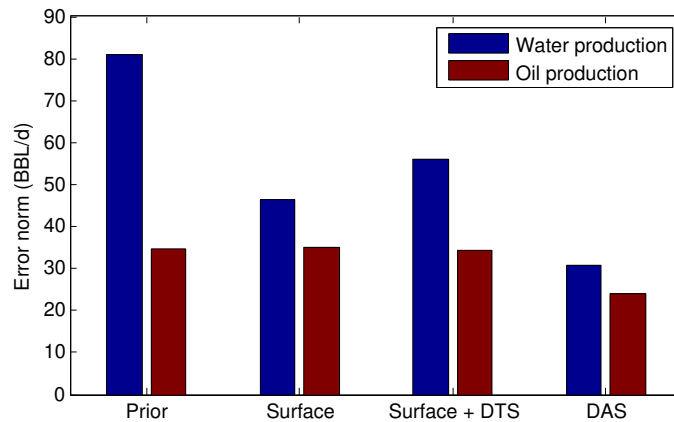


Figure 4.14: The root mean square error in oil and water production rate after history matching using three different types of measurements.

4.5 Improving Optimization by Proxy Construction with Downhole Measurements

In the previous sections, we have established that downhole measurements can be used to improve a reservoir model history match. It was also concluded that smart wells can be an efficient tool in production optimization. The optimization example, however, was performed under the assumption that available reservoir models were representative of the true reservoir. In the following example, we combine both aspects by first using flow rate measurements to history match a representative realization or a proxy of the reservoir. This step would reduce uncertainty in the reservoir model and bring it closer to the true model. Then, the history-matched model was used for production optimization. At the end, a comparison between production optima from the true model and the history-matched models is presented. History matching was performed first by only using conventional surface measurements before repeating the process with downhole measurements that are made possible by DAS and DTS.

For this example, a more complex and heterogeneous model, represented by the SPE 9 Model (GeoQuest, 2013), was used as the true model. The true model is used to provide measurements against which proxy simulation models are matched.

Table 4.4: Reservoir and fluid parameters for the SPE 9 Model.

Property	Value
Grid size	$24 \times 25 \times 15$
Grid cell dimension	300 ft \times 300 ft \times 20 ft
Average porosity	12.6%
Average permeability	108 md
Initial pressure (p_i) at datum	3,000 psi at 9,035 ft
ρ_o and ρ_w at p_i	45 and 63 lb/ft ³
μ_o and μ_w at p_i	1.18 and 0.96 cp
S_{or} and S_{wi}	0.12 and 0.20

Properties of the true reservoir are listed in Table 4.4 and the model is shown in Figure 4.15. There are two horizontal injectors injecting water into the bottom and middle layers and two trilateral producers in the model. A high permeability channel connects one of the injection wells to lateral 1 of producer 1 and lateral 3 of producer 2. Each lateral in the producer is controlled by an ICV that can assume six positions. The model was run for the first three years with all valves fully-open to introduce two-phase flow at the producer.

The concept of this example is based on the notion that the reservoir behavior can be sufficiently understood when several observation samples are collected. By changing the well controls in each sample, the relationship between ICV controls (proxy model inputs) and well production (proxy model outputs) is established as shown in Figure 4.16. The overall procedure followed for this application is based on the work of Aitokhuehi (2004) and is summarized as:

1. Specify an initial proxy model to evaluate different flow scenarios. This model can be a geologic realization of the true model or a statistical proxy based on flow measurements of the true model.
2. Apply the optimization algorithm to said models to obtain valve settings that

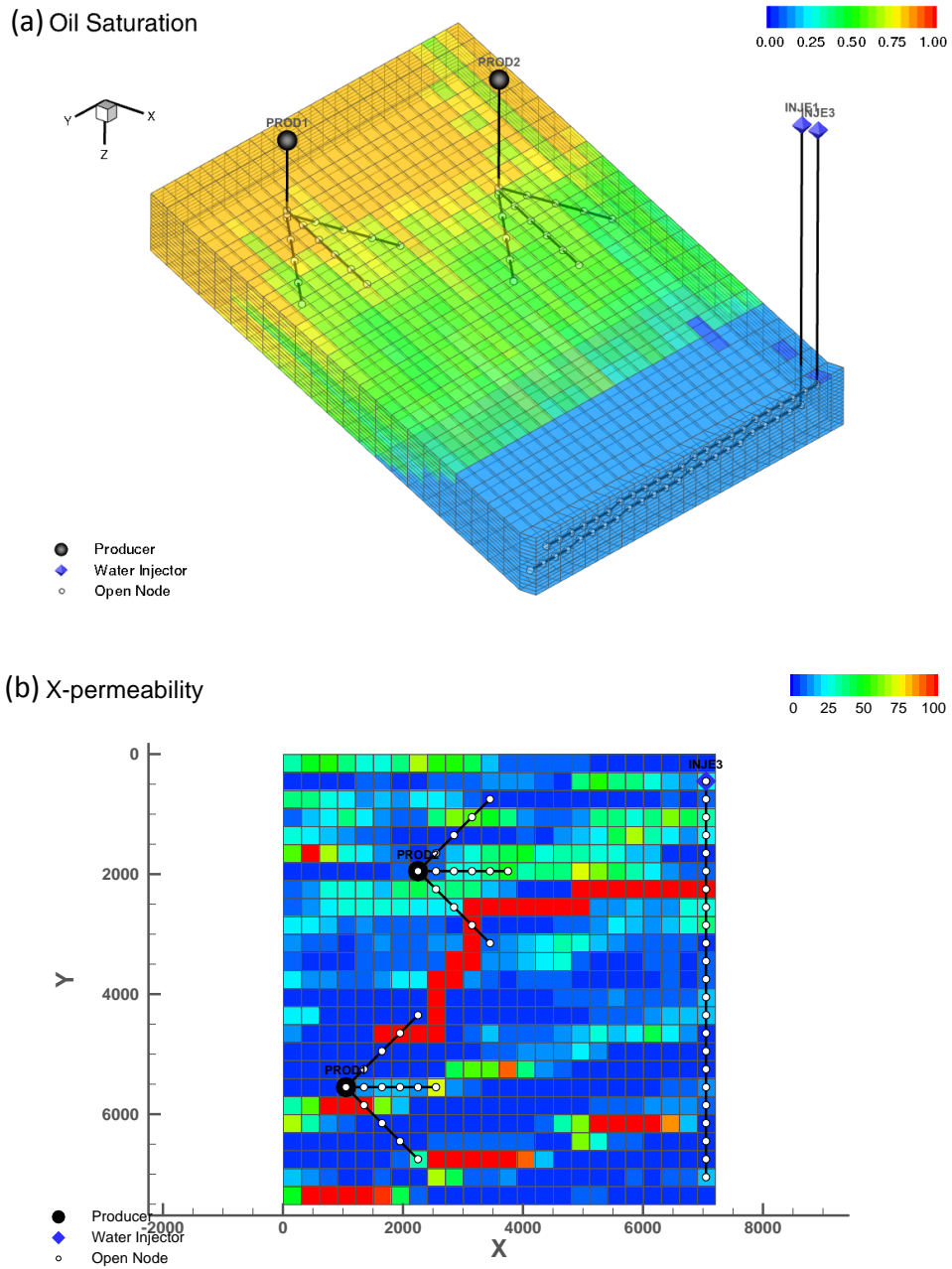


Figure 4.15: The multilateral well configuration shown with (a) the initial oil saturation and (b) the permeability distribution.

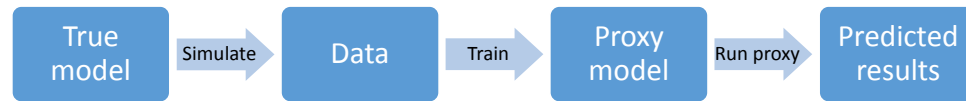


Figure 4.16: Steps of constructing a proxy model based on true model data.

optimize the objective function.

3. Apply this optimal valve settings to the same wells in the true model. In real applications, this would be the subsurface reservoir. The true model is assumed to be unknown throughout the optimization.
4. Collect production data from the true model with the optimum valve setting values.
5. Update and history match proxy models with data obtained from the true model.
6. Repeat steps 2-5 periodically until a good match between the proxy and the true model is achieved.

Two methods were used to construct proxy models that depict the true model. For the methods to be used for decision-making purposes regularly with reasonable amount of confidence, selected methods have to satisfy two main criteria (Artun, 2016). First, the proxy model should be updated easily when new data are available. Second, the method should provide sufficiently accurate results that are representative of the actual system. The first method is purely data-driven using Artificial Neural Networks (ANN) with no regard to the underlying flow physics. The second method considered a reduced-physics representation of the true model. Uncertainty is reduced in this method by minimizing the mismatch between the output of the true model and that of the reduced-physics model. While the first approach is very fast to implement, the second provides a more accurate, long-term representation of the true model.

4.5.1 Method 1: Using Artificial Neural Networks

ANNs are information-processing systems that have certain performance characteristics in common with biological neural networks. ANNs consist an input and output

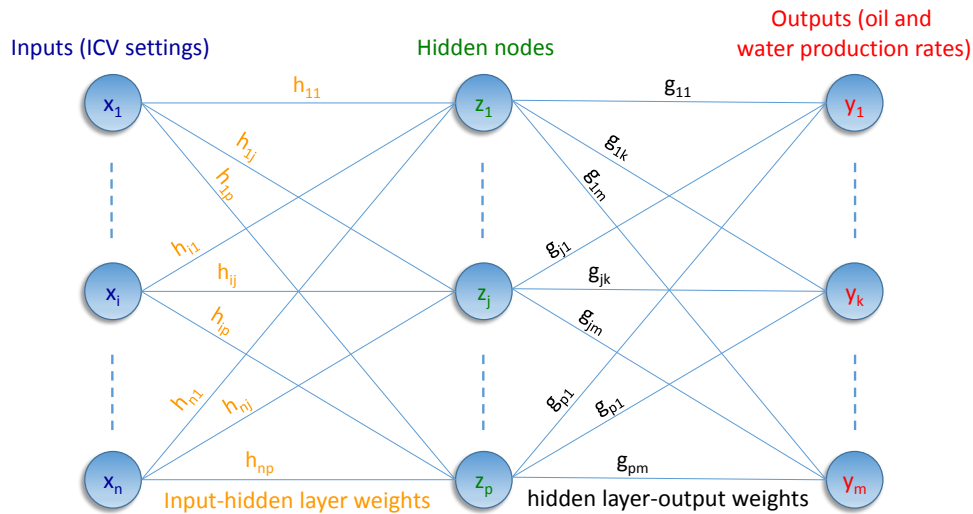


Figure 4.17: Artificial neural network structure. n , m , and p refer to the number of inputs, outputs and hidden nodes, respectively. Indexed x , y , z 's refer to a specific node in the input, output or the hidden layer. h represent weights between the input and the hidden layers, while g represent weights between the hidden the output layers.

layer, and one or several hidden layers (Figure 4.17). The hidden layer contains a transfer function (usually nonlinear functions like sigmoid or logistic functions for complex problems) between the input and output. A set of adaptive weights link each input in the network to each transfer function in the hidden layer (node). Another set of weights are multiplied by the links between transfer functions and the output. These weights are tuned by a learning algorithm and are capable of approximating nonlinear functions of the input (Mohagheh, 2000).

Using such a technique was considered because it depends completely on the feedback of the well (production measurements). It avoids the problems associated with model-based control strategies that often use uncertain reservoir model predictions (Ijioma and Jackson, 2014). The overall goal is to train the network such that it can respond correctly to input patterns that are used for training. Then, the trained network should be able to reasonably generalize responses to similar input patterns (Fausett, 1994).

The built-in toolbox in MATLAB R2013b was used to perform this exercise (MathWorks, 2013). The overall procedure for the method is summarized in these steps:

1. Select a number of ICV settings for the six valves, $X^k = [X_{ICV1}, \dots, X_{ICV6}]$. The samples were selected such that the input range is covered for all ICVs. Each ICV was assumed to take six positions from 0 (fully closed) to 1 (fully open).
2. Obtain production measurements from the true model, $F(X^1)$.
3. Fit an artificial neural network that correlates input to output.
4. Repeat steps 1-3 until mismatch between true model and ANN results is minimized.
5. Use ANN to evaluate performance of untested ICV setting combinations.

To fit the ANN for this particular application, we used the rules of thumb in designing ANN suggested by Heaton (2008). One hidden layer with variable neuron size was used. The number of neurons in the layers was varied to optimize the fit depending on the number of ICV setting combinations (the network input). A backpropagation algorithm based on a recursive scaled conjugate-gradient method was used to fit the network. Weights linking the different elements in the three layers are adjusted such that total squared error of the output is minimized when compared to measurements. For each network fitting run, 75% of the samples were used to fit the network. To avoid overfitting, 15% of input points were used for validation (network convergence is declared when error in validation set is minimized). The remaining 10% of input points were used for testing.

Several ANN cases were trained using an increasing number of samples (ICV combinations) from 10 to 100. Each case was run once by using surface flow rates to train the ANN, and another time using downhole flow rates (20 proxy models in total). To evaluate errors consistently, the RMSE for each case was calculated on a 'per well, per phase, per sample' basis. The results are shown in Figure 4.18. The general trend in the plot shows that the model predictability improves as more samples are used to train it. On average, using downhole flow rates reduces the match error by more than 50%. An example of the ANN proxy output compared to the true model

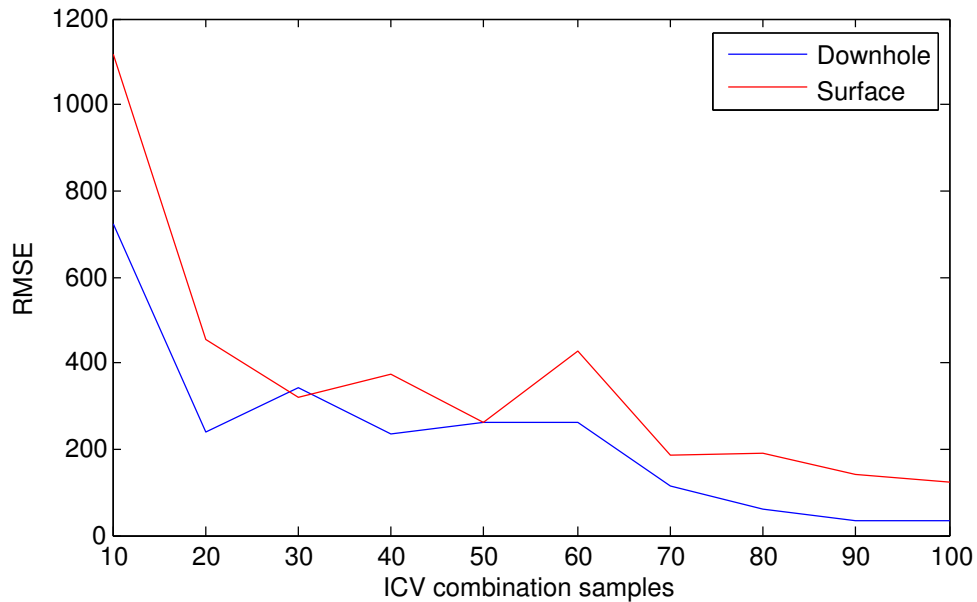


Figure 4.18: Root mean square error after fitting the neural network with downhole (blue) and surface (red) measurements using different ICV control samples.

output is shown in Figure 4.19. The four plots show the model regression for a small (10 ICV combinations) and a big (80 ICV combinations) sample size when surface and downhole flow rates were used to train the model. Production data from the true model were reproduced almost exactly by the ANN proxy when 80 observations samples were used to train and validate the model.

To take this analysis one step further, we used each of the 20 constructed proxy models to optimize the field production. The new optimization process is similar to that shown in Figure 4.3 but the GA algorithm is applied on the proxy model instead of the true model. Running flow simulations was only needed to evaluate the true optimum and to train proxy models. Otherwise, fast optimization using the proxy was performed. This makes such an optimization technique very cheap computationally. One drawback of this method, however, is that flow predictions are only accurate for the current reservoir conditions (reservoir pressure and saturation). As such, the chosen objective function here is the undiscounted net cash flow, CF , from the first

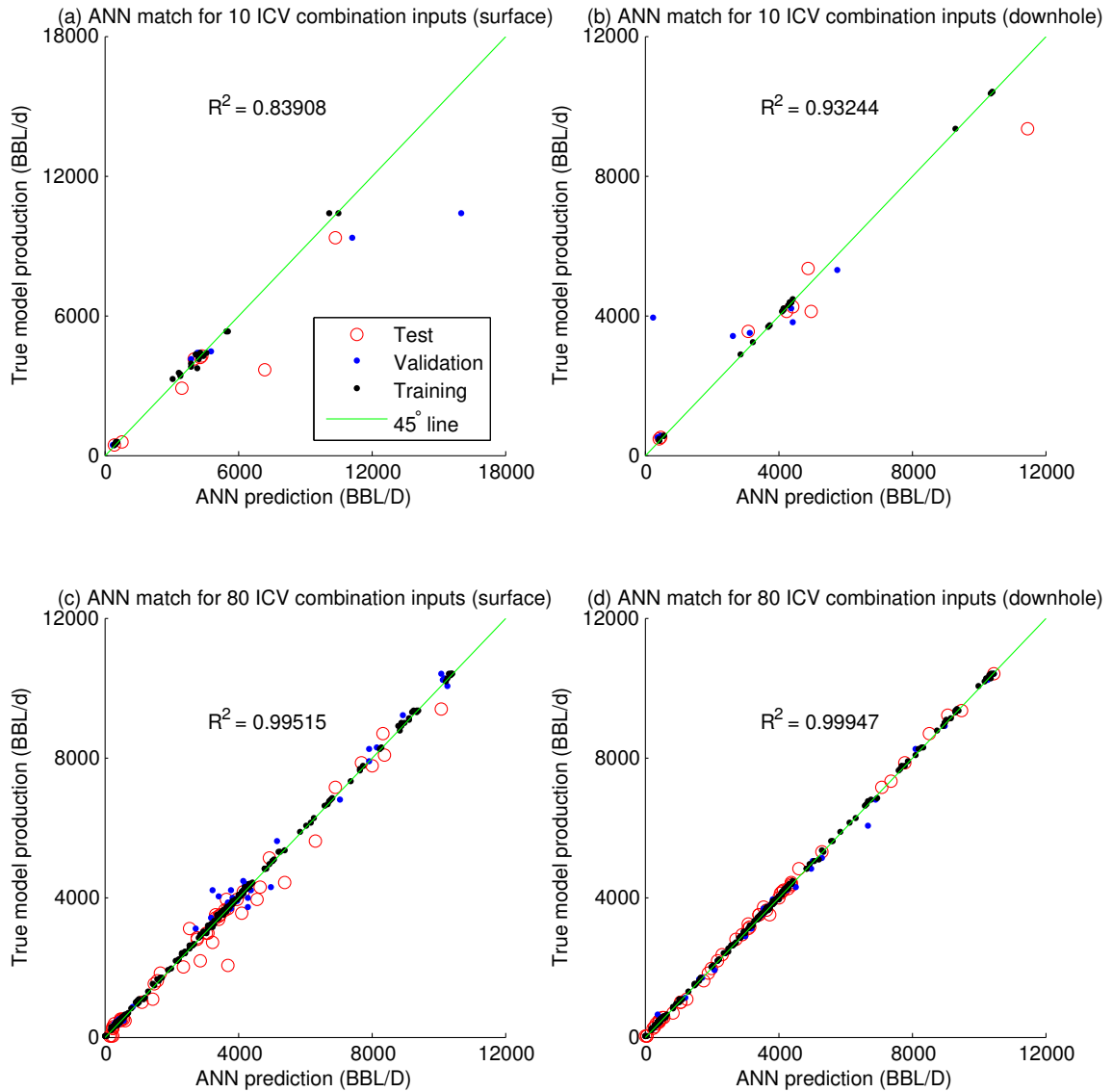


Figure 4.19: ANN regression results comparing the fit when surface measurements (left) are used opposed to downhole measurements (right). Plots to the bottom show the effect of increasing the number of ICV combination samples.

month of production given by:

$$CF = (Q_o c_o - Q_w c_{wp} - I_w c_{wi}) 30 \frac{\text{days}}{\text{month}}, \quad (4.11)$$

where Q and I are the cumulative production and injection during the month for each phase and c is the revenue/cost per barrel for that phase. Oil price (c_o) is assumed to be \$50/BBL and water production (c_{wp}) and injection cost (c_{wi}) are assumed to be \$5/BBL.

Optimization on the true model revealed that optimal ICV settings to produce the first month is [1, 1, 1, 1, 1, 0] for the six valves. Remember that the last lateral intersected a high permeability channel and was thus shut in by the optimizer. Optimization on each proxy model returned a different optimal answer. The exact true answer was only captured in two cases: when 90 and 100 downhole production samples were used to train the proxy. In all other cases, the resulting cash flow was suboptimal as illustrated in Figure 4.20. With the exception of one case, using downhole measurements always improved the problem solution. On average, using downhole measurement to solve the problem improved the first month cash flow by 6.7%, which is equivalent to about half a million dollars.

These results reflect the strength of smart completions and distributed downhole measurements. Regularly operating ICVs to obtain more production samples and using downhole flow rates would lead to increased potential revenues. The limitation of this method, however, is that proxy models are static and cannot be used to replace the simulator for large time steps. This issue was addressed with the next method.

4.5.2 Method 2: History Matching a Reduced-Physics Model

For the previous method to work efficiently, proxy models have to be updated at each production period. For instance, if 90 production samples were required to build an accurate proxy, it is expected that a stable flow rate is acquired for 90 different ICV combinations before an optimal ICV combination can be determined. Doing this on a regular basis would present a big operational burden. To address this issue, the next

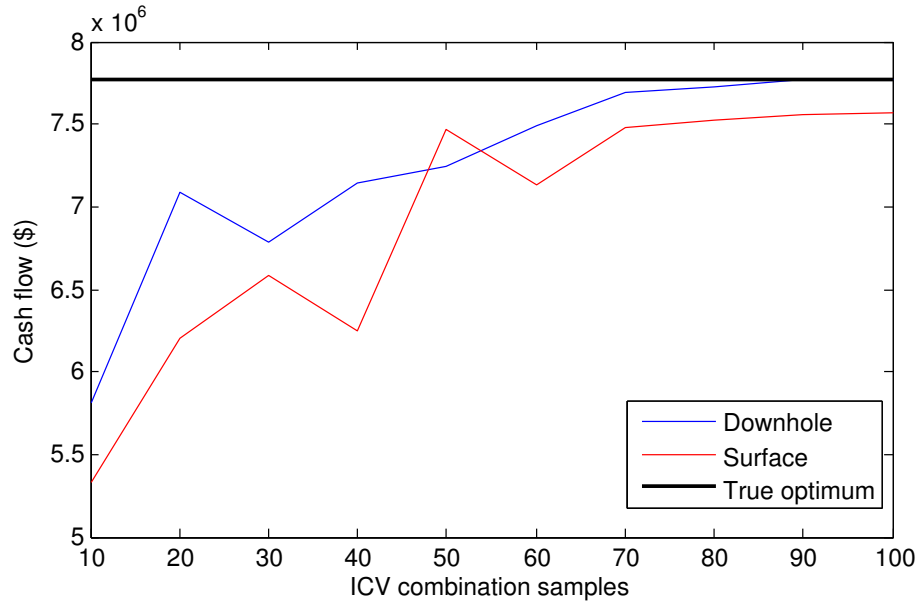


Figure 4.20: Cash flow results when the ANN proxy is used for optimization. The ANN trained with Downhole measurements (blue) generally show a better result than that trained with surface measurements (red).

method follows a procedure similar to that of the previous section but incorporates some of the physics of the true model.

This method is based on the work of Wilson and Durlofsky (2013). Initially, an upscaled realization of the reservoir is constructed. As the upscaled model would be updated regularly with flow measurements, a simple permeability power-averaging was performed according to the following equation (Durlofsky, 2005):

$$k_c = \left(\frac{1}{V_b} \int_{V_b} k_f dV \right)^\omega, \quad (4.12)$$

where V_b is the bulk volume of the coarse model. k_c and k_f represent the coarse and fine model permeabilities, respectively. The power averaging coefficient, ω , varies between -1 and 1 to represent the two extreme cases of harmonic and arithmetic means. Porosity was upscaled with an arithmetic average to conserve the pore volume. The original SPE 9 Model was reduced from $24 \times 25 \times 15$ to $12 \times 12 \times 5$. An illustration

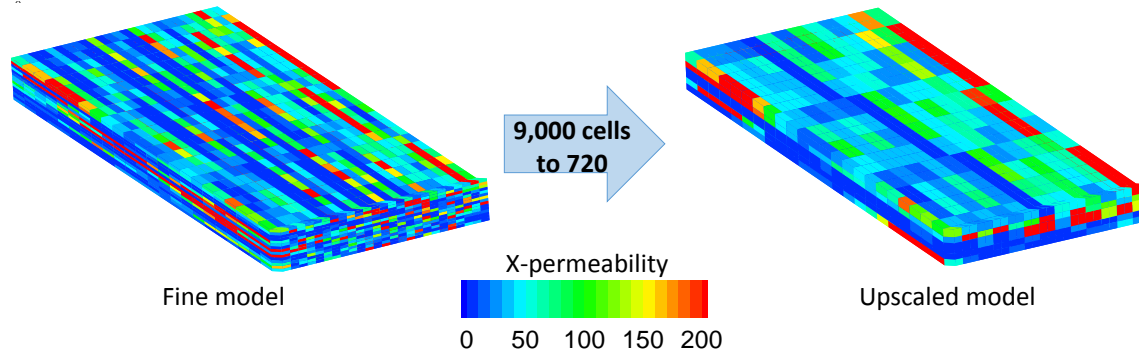


Figure 4.21: Permeability distribution of the fine and coarse model.

of the fine and upscaled models is shown in Figure 4.21.

After a number of measurements were obtained from the true model, two main properties in the upscaled model were history matched. The first property is ω in Equation (4.12). Because the upscaling procedure only considered absolute permeability, the second history-matched property is related to the relative permeability coefficients. The upscaled two-phase relative permeability curve was adjusted by optimization as dictated by LET-type correlations (Lomeland et al., 2005). These correlations were selected in favor of other models to give more flexibility in adjusting the curvature of k_{rw} and k_{ro} because the original relative permeability curves were S-shaped (Figure 4.22). Note that the fine and coarse relative permeability curves are quite different as the objective is to match production from the two models and not their permeability. The LET-type approximation is described by three curvature parameters L, E, and T as:

$$k_{rw} = \frac{k_{rw}^o(S_{wn})^{L_w}}{(S_{wn})^{L_w} + E_w(1 - S_{wn})^{T_w}}, \quad (4.13)$$

and

$$k_{ro} = \frac{(1 - S_{wn})^{L_o}}{(1 - S_{wn})^{L_o} + E_o(S_{wn})^{T_o}}, \quad (4.14)$$

where k_{rw} and k_{ro} are the water and oil relative permeability and k_{rw}^o is the water relative permeability value at the maximum water saturation value. S_{wn} is the

normalized water saturation given by:

$$S_{wn} = \frac{S_w - S_{wi}}{1 - S_{wi} - S_{or}}, \quad (4.15)$$

where S_{wi} is the irreducible water saturation and S_{or} is the residual oil saturation. The history matching process involves adjusting nine parameters in Equations 4.13 - 4.15, including L_w , L_o , E_w , E_o , T_w , T_o , k_{rw}^o , S_{wi} , and S_{or} . In addition, ω , from Equation (4.12) is optimized to minimize the upscaled model mismatch with the true model. We found that adjusting the upscaled relative permeability curves compensates for neglected physics effects inherited by the simple effective permeability upscaling. This resulted in close agreement between simulation results from the fine and coarse models. Table 4.5 describes the boundaries used for each optimization parameter.

For both the fine and coarse models, the well index is calculated with the default method in ECLIPSE using the Peaceman formulation as (GeoQuest, 2013):

$$WI = \frac{c\sqrt{k_x k_y} \Delta z}{\ln(r_o/r_{well}) + S}, \quad (4.16)$$

where c is a conversion factor, k_x and k_y are directional permeabilities, Δz is the thickness of the current grid block, r_{well} is the wellbore radius, and S is the skin factor. r_o is the effective well-block radius given by:

$$r_o = 0.28 \frac{\left(\frac{k_y}{k_x}\right)^{1/2} \Delta x^2 + \left(\frac{k_x}{k_y}\right)^{1/2} \Delta y^2}{\left(\frac{k_y}{k_x}\right)^{1/4} + \left(\frac{k_x}{k_y}\right)^{1/4}}. \quad (4.17)$$

Despite the inaccuracy expected from using the default well index, there is a consistency by using the same model for the fine and coarse models. Using a more accurate well index approach such as the semianalytical method might alleviate this issue (Shu, 2005).

The overall iterative procedure for this method is described by the following steps:

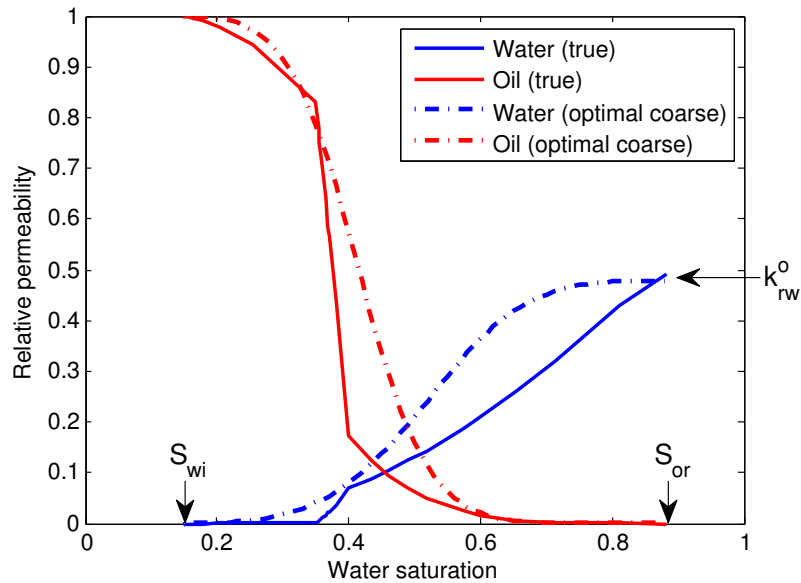


Figure 4.22: Oil and water relative permeability curves. Solid lines represent the fine model and dashed lines are relative permeability curves in the upscaled model that achieved the best match with the fine model.

Table 4.5: Upper and lower search bounds to construct absolute permeability and relative permeability curves for the coarse model. Listed optimum values correspond to solutions for fitting with ten ICV setting samples.

Parameter	Lower bound	Upper bound	Optimum value
L_w	1	6	2.1
L_o	1	6	5.4
E_w	0.2	4	1.7
E_o	0.2	4	0.74
T_w	1	6	2.8
T_o	1	6	2.1
k_{rw}^o	0.3	0.8	0.48
S_{wi}	0.05	0.4	0.15
S_{or}	0.05	0.4	0.12
ω	-1	1	-0.32

1. Obtain an upscaled realization that honors the true model geology.
2. Randomly select settings for all six ICVs, $X^1 = [X_{ICV1}, \dots, X_{ICV6}]$. Each ICV was assumed to take six positions from 0 (fully closed) to 1 (fully open).
3. Obtain production measurements from the true model, $F(X^1)$.
4. Adjust permeability parameters to minimize error between true and coarse models.
5. Repeat steps 2-4 until mismatch between true and upscaled models is minimized.
6. Use upscaled model to evaluate performance of untested ICV setting combinations.

During history matching, the mismatch between true measurements and model results were minimized using the genetic algorithm described earlier. The objective function is the L-2 norm of the difference between oil and water production rate from all laterals and all ICV setting combinations according to the definition in Equation (4.10). Again, the performance of this method correlated with the number of measurements used to history match the upscaled model. In Figure 4.23, the mismatch is plotted as a function of the number of samples when downhole and surface measurements were used to update the upscaled model. We note that relying on the initial upscaled model without any history matching (zero samples used) returns about double the error compared to using only five measurements to history match it. For this case, we stopped at 15 samples as no significant improvement in the model match was observed after this sample size. At 15 ICV combination samples, the error in history matching a reduced-physics model was almost equivalent to the error when 80 measurements were used to train an ANN model.

The next step was to use the history-matched reduced-physics model for production optimization in a procedure similar to that of the previous section. Because models were calibrated to match production from the true model, it was expected that they would yield optimum solutions that are close to the true optimum. Because the updated upscaled models tend to follow the behavior of the fine model in the long term, the objective function to be maximized is the NPV for three years of production

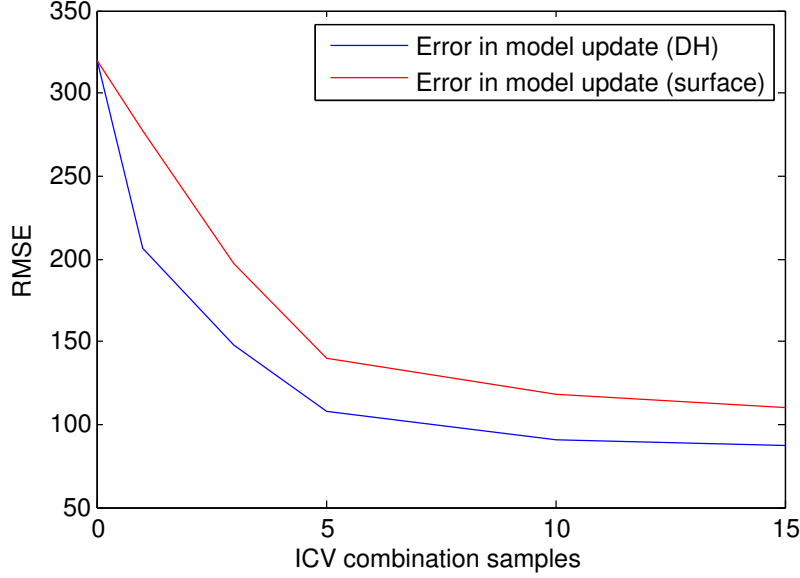


Figure 4.23: Root mean square error after updating the coarse model with down-hole (blue) and surface (red) measurements using different ICV control samples.

given by:

$$NPV = \sum_{j=1}^{N_{well}} \left[C_d^j + \sum_{k=1}^{N_t} \left[\frac{\Delta t^k}{(1+r)^k} (c_o q_o^{j,k} - c_{pw} q_{pw}^{j,k} - c_{iw} q_{iw}^{j,k}) \right] \right], \quad (4.18)$$

where q_o , q_{pw} , and q_{iw} , refer to the oil production rate, and water production and injection rates. The rest of the economic variables are explained and listed in Table 4.6. Note that we used a monthly discount rate, r , in this case and a simulation time step of one month, which is why $(1+r)$ is raised to the power k .

To discuss the results, we will refer to the upscaled model that is history-matched with surface measurements as Case 1. Case 2 will refer to the match where downhole measurements were used. In addition, optimization was performed on the initial upscaled model with no history matching (Base Case). All optimization cases were repeated three times to ensure consistency and repeatability from this stochastic GA method. Final optimum solutions from each case in addition to the optimum from

Table 4.6: Economic parameters used to calculate the NPV for this example.

Parameter	Description	Value
N_{well}	Number of wells	4
N_t	Simulation steps	36
C_d	Well drilling cost	\$10MM for producers, \$5MM for injector
Δt_k	Time step size	30 days
r	Discount rate	1%/month
c_o	Oil revenue	\$40/BBL
c_{pw}	Water production cost	\$5/BBL
c_{iw}	Water injection cost	\$5/BBL

the true model are shown in Table 4.7. It is observed that Case 2 yields a solution that either matches the true solution or that is different by one setting for all ICVs. Both history-matched cases were able to capture the effect of the high permeability channel connecting the injector to lateral 3 in producer 2 by restricting that lateral. This was not the case for the Base Case, which was not history-matched.

Figure 4.24 shows the NPV of the optimum solution for each case. Although the NPV of Case 1 was the highest (red bars), this result is misleading as it compares the performance of the optimum solution in different models (upscaled vs. true). Instead, the optimum solution given by each method is applied on the true model (blue bars) to reference all cases to the same model. The gap between the blue and red bars might be indicative of the uncertainty associated with each history-matched model as these models still carry some errors as previously shown in Figure 4.23. The NPV of the optimum solution from Case 2 was within 1% of the true case optimum while the NPV of Case 1 was lower by about 5%. From these results, it is evident that history matching a model after upscaling it improves the optimization outcome for the model studied. This is in line with the conclusions of Aitokhuehi (2004). Further, using downhole measurements to update the model appears to be more beneficial for this process.

Figure 4.25 compares production performance of solutions from the three cases when applied on the true model. Case 2 solutions closely matched both oil and water production. The solution suggested by optimizing Case 1 accelerated some of the oil production but also produced considerably more water. The production profiles from the Base Case do not follow the trend of other cases. Initial production was hindered by higher water production due to relaxing the water-producing lateral.

Table 4.7: Optimum valve settings from the true model compared to solutions provided by the reduced-physics models. Results for the base upscaled model are shown in addition to results for matching using surface and downhole measurements. Bold valve setting values signify exact match with the true model and underlined values indicate a difference of one position compared with the true optimum.

Well	True	Upscaled (no HM)	Upscaled (surface)	Upscaled (downhole)
Prod1, Lat1	0.8	<u>0.6</u>	<u>1.0</u>	<u>0.6</u>
Lat2	0.6	1.0	1.0	<u>0.8</u>
Lat3	1.0	1.0	1.0	1.0
Prod2, Lat1	0.6	<u>0.8</u>	1.0	0.6
Lat2	1.0	1.0	1.0	1.0
Lat3	0.0	0.6	0.0	<u>0.2</u>

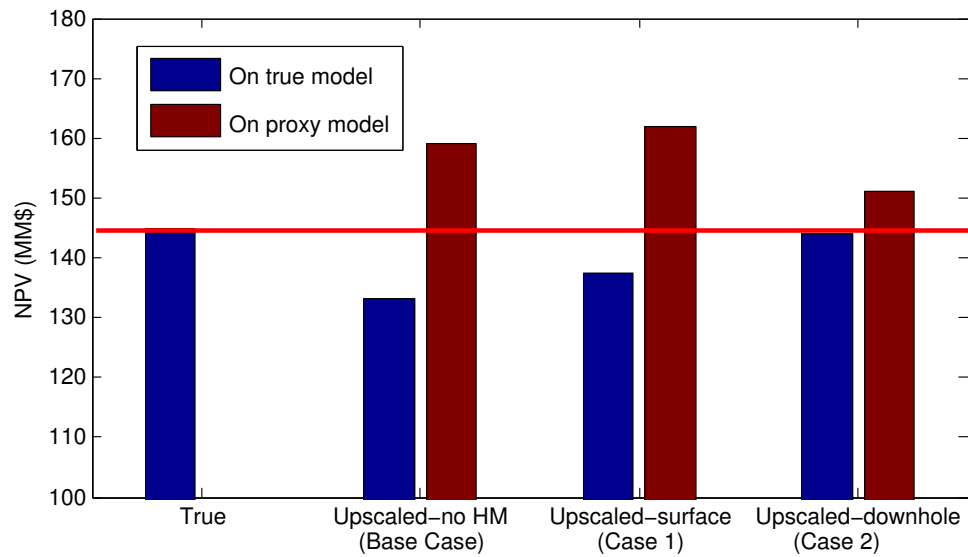


Figure 4.24: NPV of the three optimization cases on the upscaled model as compared to optimum NPV results of the true model.

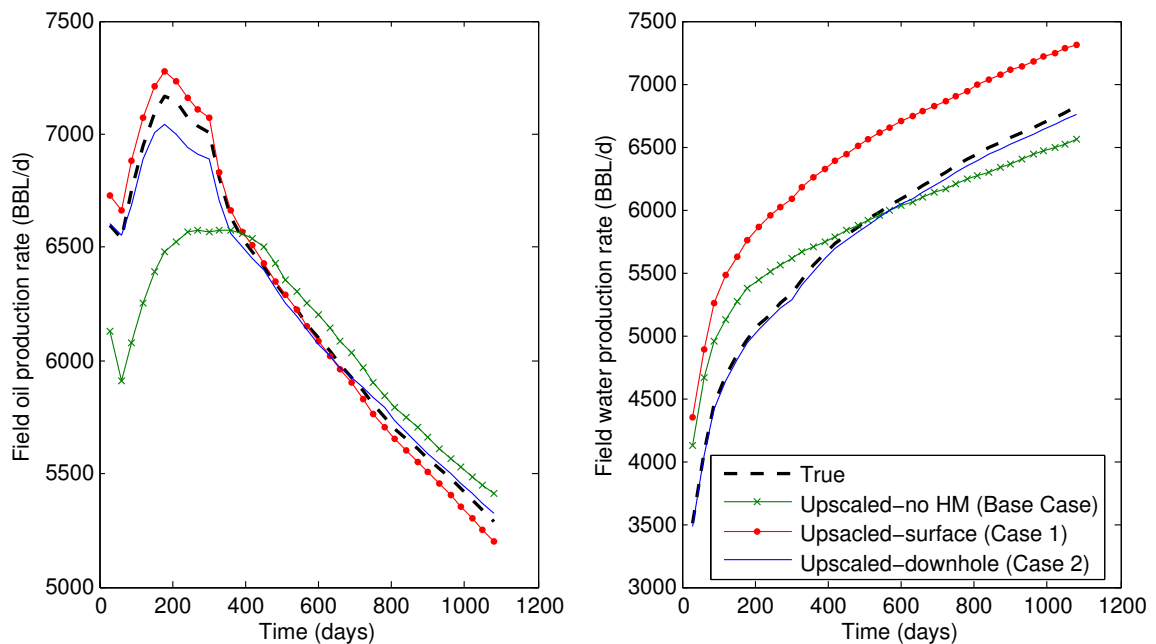


Figure 4.25: Total field oil (left) and water (right) production rates for the true model and the three optimization cases.

4.6 Concluding Remarks

In the work described in this chapter, we tested a range of different applications to evaluate the utilization of DAS and DTS in production optimization. In each of these applications, optimal solutions were found when surface flow rates and downhole flow rates were used for optimization. Comparing solutions from the two methodologies allowed us to ascertain improvements gained by using DAS and downhole measurements as opposed to using regular surface readings. The results revealed that using downhole measurements obtained better solutions in most cases. Other examples showed a similar conclusion when downhole flow rates were used to history match uncertain realizations of a reservoir model. While downhole temperature did not improve the history match for the tested case, adding downhole flow rates clearly did.

In the most basic case, downhole flow rate measurements can be used in a fully reactive approach by restricting any well segment that starts to produce water. A more advanced reservoir management approach, however, is to use a defensive production optimization approach. This was shown in Section 4.5.2 where production was optimized on an upscaled model with reduced physics that was updated with flow measurement. Using a statistical model (such as ANN) for optimization, would provide middle ground between the two approaches. Such a model can be used when the data are available but solutions are needed under tight time constraints. Both these methods are open for further improvement. For example, a more advanced upscaling scheme can be used to represent the reduced-physics models.

Chapter 5

Conclusions and Recommendations for Future Work

This work investigated a systematic inflow profiling procedure utilizing distributed acoustic and temperature measurements. With the capability to determine the phase fractions and velocity of incoming flow in a smart well, it is possible to adjust the smart well controls to enhance production. To take full advantage of the functionality of smart completions, a production optimization approach was integrated with the monitoring and control aspects of these wells. By applying the profiling and optimization modules in tandem, the smart well controls can be modified frequently according to the current production conditions. This profiling and optimization workflow addresses many of the current inadequacies in operating smart wells.

The profiling approach involves using two methods to solve the two-phase incoming flow from different segments of a smart well that is completed with inflow control valves. The first method employs several signal processing techniques to convert distributed acoustic measurements to a phase fraction and a total flow rate calculation. The process starts by transforming the data to a different domain to obtain the speed of sound within the fluid medium based on its functionality with the signal's frequency and wavenumber. Then, the fluid phase fractions are determined by incorporating thermodynamic fluid mixing rules for the speed of sound. Additionally, the Doppler

Shift equations are used to calculate the fluid velocity for that particular section. The second method depends on obtaining the temperature and pressure change between the reservoir and the wellbore as fluids are produced through the valves. These differentials are used to calculate the fluid's Joule-Thomson coefficient. Once this coefficient is determined, equations of state are solved to obtain the two-phase fluid fractions.

When both methods are implemented separately, only two variables can be solved, which limits the methods' application in three-phase flow. It is possible to approximate the three-phase flow problem by lumping oil and water as a single phase. A more accurate approach, however, is to combine information from both methods. For that purpose, we showed solutions of the system of nonlinear equations involving equations of the speed of sound (DAS data) and the Joule-Thomson effect (DTS data).

The last part of this research was to apply the developed inflow profiling methodologies in different history matching and flow optimization settings. Studied cases included using downhole measurements to history match the permeability field of a channelized reservoir model. In addition, we presented different examples to demonstrate the importance of regularly modifying ICV settings during the production lifetime of a well. Lastly, other examples focused on using downhole measurements to build proxies to estimate well production in lieu of the full-physics field reservoir model.

5.1 Conclusions

These methodologies were applied to different scenarios. When available, the profiling algorithm was tested on real production data sets. Otherwise, synthetic cases emulating typical smart field environments were tested. The key findings of applying these procedures include:

- When analyzing production data from a real single-phase oil well, the DAS inflow profiling algorithm was able to determine production flow rate from each

smart zone. The total rate from all zones matched the flow rate given by the surface flow meter. By calculating flow rates associated with different ICV settings, the relative contribution of each zone was understood.

- In the two-phase flow well, results were highly dependent on the flow regime due to the underlying assumptions in the equations. The velocity calculation was inaccurate due to high noise in the downgoing (against the flow) speed of sound signal. The exception to this was when a slug flow regime was present. In this case, the flow velocity was estimated as oil slugs showed pockets of lower speed of sound values moving up the tubing with time. Fluid phase fractions were calculated for regions where a homogeneous flow regime exists and a match was achieved with surface flow meters.
- The DTS phase fraction model was applied successfully in a two-phase flow simulated scenario. Phase fractions resulting from calculating the Joule-Thomson coefficient in the bottom production interval matched simulation results with 5%.
- Further three-phase simulations with varying gas holdup and water cut values were generated. When the phase fractions were resolved using the DAS and DAS equations successively, high errors resulted from the assumption of lumping the oil and water as a single liquid phase. This issue was resolved when the system of nonlinear equations was solved simultaneously by employing least squares regression.
- When a Kalman filter was used to history match an ensemble of realizations using production rates, downhole values improved the match compared to surface values. The average error in water production was almost halved and average error in oil production was reduced by about 50%.
- Studied examples revealed that optimizing production controls with DAS and DTS calculated rates (as opposed to surface flow rates) lead to enhanced reservoir sweep and improved project economics. Moreover, using downhole flow rates lead to more accurate reservoir proxies, which can be used for faster reservoir management decisions.

- There was a trade-off between the feedback-based (ANN proxy) and the model-based (history matching an upscaled model) control optimization approach. The first method presented a very fast optimization option but was only accurate for short time production scenarios. On the other hand, the second option obtained solutions that conform to long-term production strategies, albeit being much slower to run. The choice of these techniques should depend on the objective at hand.

5.2 Future Work

This research represented an initial effort to utilize distributed acoustic and temperature measurements for downhole flow profiling. With the potential benefits of downhole measurements shown in this work, we present some suggestions to further extend this application in the future.

- Conduct laboratory experiments of DAS/DTS measurements under controlled flow conditions. All examples and data sets analyzed by our algorithm were either real field production data or synthetic data. For the real data, we had no control over the input and the production scenario. Running experiments of this nature would enable us to establish a correlation between flow rates and the acoustic/temperature response. With a design of experiment approach, the sensitivity of flow rate to each input parameter could be understood better.
- Test the suggested DTS configuration to capture the Joule-Thomson coefficient in the field. The use of the Joule-Thomson effect to deduce phase fractions based on thermal expansion was implemented theoretically in this work. To check if the equations hold under different thermal conduction and heat transfer effects, this should be tested in a field or experimental setting. This could be performed by simultaneously monitoring the wellbore and the reservoir sandface temperatures as the fluid is produced.
- Use in-situ phase fractions to calibrate multiphase drift-flux models. The results of this study estimated in-situ phase fractions and the total fluid velocity.

Implementation of a drift-flux or another mechanistic model is needed to estimate individual phase velocities. One methodology to achieve this is discussed in the the work of Shi, Holmes, Durlafsky, Aziz, Diaz, Alkaya and Oddie (2005) for two-phase flow and Shi, Holmes, Diaz, Durlafsky and Aziz (2005) for three-phase flow. The model can also be used to complement DAS measurements in intervals where DAS measurements fail to provide an accurate reading as was the case in the two-phase flow example. The two main parameters in such models (the profile parameter and drift velocity) depend on the gas phase fraction. If these parameters are calibrated using measurements where DAS data are accurate, the model can be used to obtain velocities and phase fractions in other regions of the well.

- Conduct further research to improve the profiling performance under different flow regimes. Recent work from Finfer et al. (2015) suggested that using DAS to analyze vortex shedding instead of using it to calculate speeds of sound improves its performance in bubbly and stratified flow regimes. The development of specific profiling equations for different flow regimes presents a useful research opportunity.
- Investigate the application of distributed downhole measurements in data mining. These approaches were successfully applied for pressure data from permanent downhole gauges (Liu, 2013). The abundance of DAS and DTS data, which are distributed in time and space, makes the use of data mining ideal to extract patterns from the data.
- Apply the optimization workflow in a continuous, closed-loop fashion. Figure 5.1 shows a suggested procedure to use the data to update reservoir models, then to optimize production. The individual components were explained in previous examples. We also demonstrated the successive application of history matching and production optimization using downhole data. Most of these methods, however, work best when updated regularly to reflect current reservoir conditions. Ultimately, it is desired to show this in a real field.
- Examine performing the optimization work flow with gradient-based techniques. Although not detrimental to the purpose of this study, extensive simulation

times might deter performing meaningful optimization studies in a real field setting. One way to address this issue is by reducing the number of required objective function evaluations with a gradient-based optimizer.

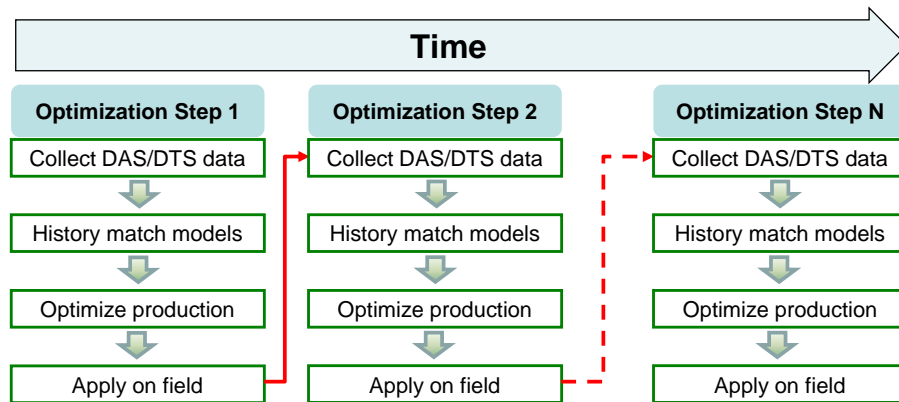


Figure 5.1: Procedure of real-time model update and valve setting optimization with the help of distributed downhole measurements.

Appendix A

The Integral Image Value Algorithm

Implementation of this algorithm was based on the work of Viola and Jones (2001). The technique starts by defining a number of slope lines that range from the lowest to the highest expected speed of sound value and that pass through the origin of the f - k plot. The integral value, I , through each line is defined using the Randon transform as:

$$I^k = \frac{1}{L} \sum_{i=0}^{N_x} \sum_{j=0}^{N_t} \ell^{ijk} F^{ijk}, \quad (\text{A.1})$$

where F^{ijk} represent the Fourier coefficient for the i^{th} wavenumber, the j^{th} frequency, and the k^{th} slope value and L is the total slope line length. The length of the slope line in each grid cell, ℓ , is calculated by geometrically tracking the line intersection points with the frequency and wavenumber grid lines as shown in Figure A.1 as described by the following procedure:

1. Each slope line makes an angle $\theta = \text{atan}(\text{slope})$ with the f - k plain
2. Each line starts at the origin: $[x, y]_{in}^{(i=0, j=0)} = [0, 0]$

3. The length of the slope line within the first cell is given by:

$$\ell^{(i=0,j=0)} = \min \left\{ \frac{\Delta k}{\cos\theta}, \frac{\Delta f}{\sin\theta} \right\}$$

4. Calculate the position that the line exits the cell based on the line length as:

$$[x, y]_{out}^{(i=0,j=0)} = \begin{cases} [\Delta k, \ell^{(i=0,j=0)} \sin\theta] & \text{if line exits at the y-axis} \\ [\ell^{(i=0,j=0)} \cos\theta, \Delta f] & \text{if line exits at the x-axis} \end{cases}$$

5. Move to the next cell with $[x, y]_{in}^{new} = [x, y]_{out}^{(i=0,j=0)}$ where *new* contains *i* and *j* indices of the next cell that the line hits.
6. Repeat steps 1-5 until the end of the slope line. The generalized equations for slope line length within the cell and axis intersection points are:

$$\ell^{(i,j)} = \min \left\{ \frac{x_{in}^{(i,j)} - x_{out}^{(i,j)}}{\cos\theta}, \frac{y_{in}^{(i,j)} - y_{out}^{(i,j)}}{\sin\theta} \right\}, \quad (\text{A.2})$$

and

$$[x, y]_{out}^{new} = [x, y]_{in}^{new} + [\ell^{(i,j)} \cos\theta, \ell^{(i,j)} \sin\theta]. \quad (\text{A.3})$$

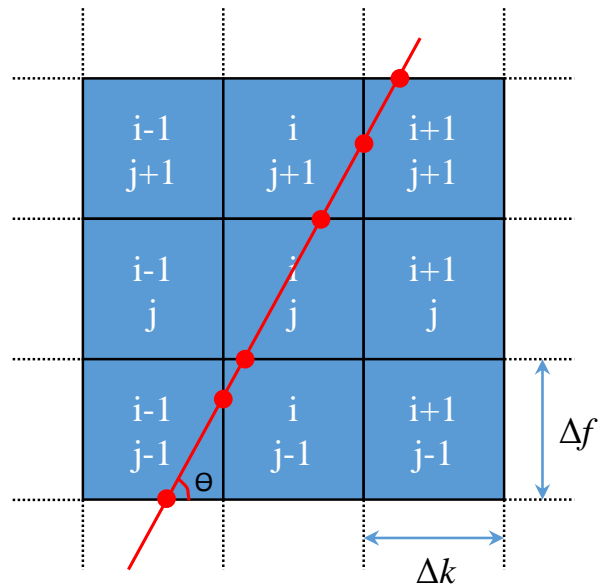


Figure A.1: Example of a frequency-wavenumber grid and the resulting intersection points when a slope line is drawn on the image. The integral value method calculates the slope line length in each cell by determining the intersection points.

Appendix B

Coupled Reservoir/Wellbore Thermal Model

In Chapter 3, we showed that Joule-Thomson thermal cooling or heating can be used to distinguish the type of produced fluid. To generalize that procedure, the heat flux from the production stream below the current inflow point need to be considered. Moreover, gravitational effects of inclined wells should be included. In this section, a coupled reservoir/wellbore thermal model to account for these scenarios, based on the work of Hasan et al. (2009), is presented. The general energy balance equation for a production well (Figure B.1) is:

$$-Q = w_1 \left(\frac{dH}{dz} - g \cdot \sin\theta + v_m \frac{dv_m}{dz} \right) + w_2 c_p \frac{T_{well} T_{sf}}{dz}, \quad (\text{B.1})$$

where Q is the heat flow rate per unit length of the wellbore, w is the mass flow rate and other parameters are as defined in the figure. The left-hand side of the equation can be expressed as:

$$Q = -L_R c_p w (T_{well} - T_G), \quad (\text{B.2})$$

where T_G is the geothermal temperature at the current depth. L_R is a relaxation length parameter that depends on the fluid/formation thermal properties and the

overall heat transfer coefficient, U_t . For onshore wells, it is given by:

$$L_R = \frac{2\pi}{c_p w} \left(\frac{r_{to} U_t k_e}{k_e + (r_{to} U_t T_D)} \right), \quad (\text{B.3})$$

where r_{to} is the outer tubing radius, and k_e is the thermal conductivity of earth. This parameter a function of the dimensionless temperature, T_D , given by (Hasan and Kabir, 2002)

$$T_D = \frac{2\pi k_e}{Q} (T_{well} - T_G). \quad (\text{B.4})$$

The enthalpy in Equation (B.1) is expressed in terms of measurable parameters as:

$$dH = c_p dT - C_{JT} c_p dP. \quad (\text{B.5})$$

In relation with our developed inflow profiling procedure, we suggest the following steps to solve for in-situ phase fractions using temperature at any location of the well:

1. Collect DTS data from the wellbore and the reservoir.
2. Estimate mixture flow rate and velocity with the method discussed in Section 2.4 and assume phase fractions.
3. Calculate mixture properties including the density and heat capacity.
4. Calculate the resulting wellbore temperature profile using the model presented in this section.
5. Solve as a least squares problem to find the temperature profile that best matches measured DTS.

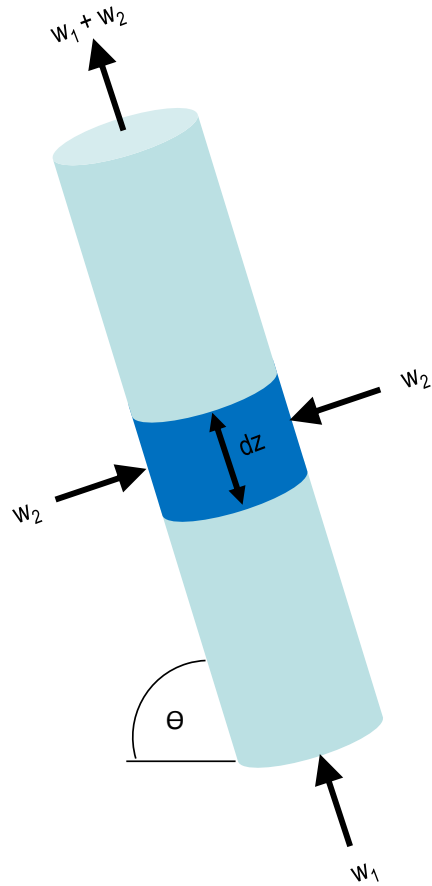


Figure B.1: Schematic of a deviated wellbore with fluid influx upstream of the current producing perforation.

Nomenclature

Abbreviations

ANN	Artificial Neural Network
BHP	Bottom Hole Pressure
DAS	Distributed Acoustic Sensing
DTS	Distributed Temperature Sensing
EnKF	Ensemble Kalman Filter
EoS	Equation of State
FFT	Fast Fourier Transform
GA	Genetic Algorithm
GPS	General Pattern Search
ICV	Inflow Control Valve
MRC	Maximum Reservoir Contact
NPV	Net Present Value
OTDR	Optical Time-Domain Reflectometer
PLT	Production Logging Tool
RMSE	Root Mean Square Error
SNESIM	Single Normal Equation Simulation
SNR	Signal-to-Noise Ratio
SONAR	Sound Navigation and Ranging
VSP	Vertical Seismic Profiling

Greek Symbols

α	Phase volume fraction
β	Thermal expansion coefficient
η	Crossover blending coefficient
λ	Wavelength
μ	Viscosity
Ω	Search space domain
ω	Permeability power averaging coefficient
ρ	Density
σ	Standard deviation, interfacial tension
ξ	Transformation variable

Superscripts

c	Component
i, j, k	Index
T	Transpose

Subscripts

b	Bulk
BH	Bottom hole
c	Coarse, constriction, characteristic
D	Dimensionless
d	Downgoing, drilling, drift
e	Entry, earth
f	Fluid, fine, friction
G	Geothermal
g	Gas
H	Hydrostatic
i	Injection, initial
l	Liquid
m	Mixture, model

<i>max</i>	Maximum
<i>n</i>	Normalized
<i>o</i>	Oil
<i>obs</i>	Observation
<i>opt</i>	Optimum
<i>p</i>	Phase, production, pipe
<i>r</i>	Relative, residual
<i>res</i>	Reservoir
<i>s</i>	Superficial
<i>sf</i>	Sandface
<i>std</i>	Standard
<i>t</i>	Total, true
<i>to</i>	Tubing outside
<i>u</i>	Upgoing
<i>vap</i>	Vaporization
<i>w</i>	Water
<i>well</i>	Well

Variables

<i>A</i>	Area, molar Helmholtz free energy
<i>a</i>	Acoustic amplitude
<i>B</i>	Formation volume factor
<i>c</i>	Speed of sound, cost
<i>C₀</i>	Profile parameter for drift-flux model
<i>C_e</i>	Conductive energy flow rate
<i>c_p</i>	Heat capacity
<i>C_r</i>	Optimization problem constraints
<i>C_v</i>	Valve geometry flow coefficient
<i>C_{JT}</i>	Joule-Thomson coefficient
<i>CF</i>	Cash flow
<i>d</i>	Diameter

E	Young's modulus, expected value
e	Internal energy
F	Fourier coefficients
f	Frequency, fanning friction factor
F_e	Convective enthalpy flow rate
g	Gravitational acceleration
GVF	Gas Volume Fraction
H	Enthalpy, observation matrix
I	Injection rate, integral value
K	Modulus of elasticity, Kalman gain
k	Permeability, thermal conductivity, angular wavenumber
K_D	Drag coefficient
K_u	Critical Kutateladze number
L	Length
L_R	Relaxation parameter
M	Molecular weight, mobility
N	Number of variables
n	Fluid amount in moles
p	Pressure
PI	Productivity Index
Q	Heat, cumulative oil production, covariance of the state variables
q	Flowrate
R	Residual, the gas constant, data error estimation
r	Radius, discount rate
r_o	Effective well-block radius
S	Saturation, skin factor, entropy
T	Temperature
t	Time, thickness
T_w	Transmissibility factor
U	Heat-transfer coefficient
UB and LB	Optimization parameters upper and lower bounds

V	Volume
v	Velocity
$\tilde{\nu}$	Wavenumber
w	Mass rate, stochastic white noise
WC	Water Cut
WI	Well Index
x	Phase mass fraction, distance, system state variables
y	Mole fraction, observations
Z	Gas compressibility factor
z	Depth

Bibliography

- Abukhamsin, A. (2009), *Optimization of Well Design and Location in a Real Field*, Master's thesis, Department of Energy Resources Engineering, Stanford University, Stanford, California.
- Aitokhuehi, I. (2004), *Real-Time Optimization of Smart Wells*, Master's thesis, Department of Energy Resources Engineering, Stanford University, Stanford, California.
- Al-Arnaout, I., Al-Buali, H., Al-Mubarak, S., Al-Driweesh, S., Zareef, M. and Johansen, E. (2008), 'Optimizing Production in Maximum Reservoir Contact Wells with Intelligent Completions and Optical Downhole Monitoring System', paper SPE 118033 presented at the Abu Dhabi International Petroleum Exhibition and Conference, Abu Dhabi, UAE, 3-6 November.
- Alghareeb, Z., Horne, R., Yuen, B. and Shenawi, S. (2009), 'Proactive Optimization of Oil Recovery in Multilateral Wells Using Real Time Production Data', paper SPE 124999 presented at the Annual Technical Conference and Exhibition, New Orleans, Louisiana, 4-7 October.
- Allanic, C., Frangeul, J., Liebeck, M., Carbonnier, B., Naldrett, G., Farhadiroushan, M. and Clarke, A. (2013), 'Distributed Acoustic Sensing for ESP Understanding and Surveillance', paper SPE 167501 presented at the Middle East Intelligent Energy Conference and Exhibition, Dubai, UAE, 28-30 October.

- Alyan, E., Al-Mutairi, S., Al-Subaie, F., Ünalms, Ö. and Leslie, P. (2014), ‘Production Optimizaation of Maximum Reservoir Contact Well, Part III: Field Tests with Acoustic-Tolerant Multiphase Flowmeter’, paper IPTC 17511 presented at the International Petroleum Technology Conference, Doha, Qatar, 20-22 January.
- Artun, E. (2016), ‘Characterizing Reservoir Connectivity and Forecasting Waterflood Performance Using Data-Driven and Reduced-Physics Models’, paper SPE 180488 presented at the Western Regional Meeting, Anchorage, Alaska, 23-26 May.
- Bakku, S., Wills, P. and Fehler, M. (2014), ‘Monitoring Hydraulic Fracturing Using Distributed Acoustic Sensing in a Treatment Well’, Proceedings of the Society of Exploration Geophysicists Annual Meeting, Denver, Colorado, 26-31 October, pp. 5003–5008.
- Batzle, M. and Wang, Z. (1992), ‘Seismic Properties of Pore Fluids’, *Geophysics*, **Vol. 57**(11), pp. 1396 – 1408.
- Becker, M., Cole, M., Ciervo, C., Coleman, T. and Mondanos, M. (2016), ‘Measuring Hydraulic Connection in Fractured Bedrock with Periodic Hydraulic Tests and Distributed Acoustic Sensing’, Proceedings of the 41st Workshop on Geothermal Reservoir Engineering, Stanford, California, 22-24 February, pp. 372–382.
- Bhattacharya, S. and Rao, N. (2011), ‘Reservoir Management a Key to Rejuvenation of Mature Fields’, Article #20104 presented at GEO-India, New Delhi, India, 12-14 January.
- Bohning, J., Mirsa, T. and Choudhury, M. (1998), ‘The Raman Effect’, *The Indian Association for the Cultivation of Science* (October), pp. 3–6.
- Boone, K., Crickmore, R., Werdeg, Z., Laing, C. and Shell, M. (2015), ‘Monitoring Hydraulic Fracturing Operations Using Fiber-Optic Distributed Acoustic Sensing’, paper SPE 178648 presented at the Unconventional Resources Technology Conference, San Antonio, Texas, 20-22 July.

- Boone, K., Ridge, A., Crickmore, R. and Onen, D. (2014), 'Detecting Leaks in Abandoned Gas Wells with Fibre-Optic Distributed Acoustic Sensing', paper IPTC 17530 presented at the International Petroleum Technology Conference, Doha, Qatar, 20-22 January.
- Born, M. and Wolf, E. (1999), *Principles of Optics*, 7th Edition, Cambridge University Press.
- Bukhamsin, A. and Horne, R. (2014), 'Using Distributed Acoustic Sensors to Optimize Production in Intelligent Wells', paper SPE 170679 presented at the Annual Technical Conference and Exhibition, Amsterdam, The Netherlands, 27-29 October.
- Bukhamsin, A. and Horne, R. (2016), 'Cointerpretation of Distributed Acoustic and Temperature Sensing for Improved Smart Well Inflow Profiling', paper SPE 180465 presented at the Western Regional Meeting, Anchorage, Alaska, 23-26 May.
- Caers, J. (2003), 'History Matching Under Training-Image-Based Geological Model Constraints', *SPE Journal* (September), pp. 218–226.
- Carnegie, A., Roberts, N. and Clyne, I. (1998), 'Application of New Generation Technology to Horizontal Well Production Logging - Examples from the North West Shelf of Australia', paper SPE 50178 presented at the Asia Pacific Oil & Gas Conference and Exhibition, Perth, Australia, 12-14 October.
- Chace, D., Wang, J., Mirzwinski, R., Maxit, J. and Trcka, D. (2000), 'Applications of a New Multiple Sensor Production Logging System for Horizontal and Highly-Deviated Multiphase Producers', paper SPE 63141 presented at the Annual Technical Conference and Exhibition, Dallas, Texas, 1-4 October.
- Chaudhuri, A., Osterhoudt, C. and Sinha, D. (2012), 'An Algorithm for Determining Volume Fractions in Two-Phase Liquid Flows by Measuring Sound Speed', *Journal of Fluids Engineering*, **Vol. 134**(October).

- Chen, N. (1979), ‘An Explicit Equation for Friction Factor in Pipe’, *Industrial & Engineering Chemistry Fundamentals*, **Vol. 18**(3), pp. 296–297.
- Dean, E. (1979), *Atmospheric Effects on the Speed of Sound*, Technical report, Atmospheric Sciences Laboratory, White Sands Missile Range, New Mexico.
- Denney, D. (2012), ‘Distributed Acoustic Sensing for Hydraulic Fracturing Monitoring and Diagnostics’, *Journal of Petroleum Technology* (March), pp. 68–74.
- Durlofsky, L. (2005), ‘Upscaling and Gridding of Fine Scale Geological Models for Flow Simulation’, paper presented at the 8th International Forum on Reservoir Simulation, Stresa, Italy, June 20-24.
- Duru, O. (2011), ‘Reservoir Analysis and Parameter Estimation Constrained to Temperature, Pressure and Flowrate Histories’, *SPE Reservoir Evaluation & Engineering* (August).
- Duru, O. and Horne, R. (2008), ‘Modeling Reservoir Temperature Transients and Matching to Permanent Downhole Gauge Data for Reservoir Parameter Estimation’, paper SPE 115791 presented at the Annual Technical Conference and Exhibition, Denver, Colorado, 21-24 September.
- Enright, R. (1955), ‘Sleuth for Down-Hole Leaks’, *Oil & Gas Journal* (February), pp. 78–79.
- Evensen, G. (2009), *Data Assimilation: The Ensemble Kalman Filter*, 2nd Editio, Springer.
- Fausett, L. (1994), *Fundamentals of Neural Networks: Architectures, Algorithms And Applications*, 1st Editio, Prentice-Hall.
- Finfer, D., Parker, T., Mahue, V., Amir, M., Farhadiroushan, M. and Shatalin, S. (2015), ‘Non-intrusive Multiple Zone Distributed Acoustic Sensor Flow Metering’, paper SPE 174916 presented at the Annual Technical Conference and Exhibition, Houston, Texas, 28-30 September.

- Foucault, H., Poilleux, D., Djurisic, A., Slikas, M., Strand, J. and Silva, R. (2004), 'A Successful Experience for Fiber Optic and Water Shut off on Horizontal Wells with Slotted Liner Completion in an Extra Heavy Oil Field', paper SPE 89405 presented at the Improved Oil Recovery Symposium, Tulsa, Oklahoma, 17-21 April.
- Furniss, J., Schouten, J., Bottomley, W. and Taylor, H. (2014), 'Reservoir Characterisation Using Distributed Temperature Sensing in CSG Development: Application in the Surat Basin, Queensland, Australia', paper SPE 171537 presented at the Asia Pacific Oil & Gas Conference and Exhibition, Adelaide, Australia, 14-16 October.
- GeoQuest (2013), *ECLIPSE Technical Description*, Ver. 2013., Schlumberger.
- Gysling, D. and Loose, D. (2004), 'SONAR Gets into Flow: New Type of Meters for Chemical Industry', *Chemical Manufacturing* (January).
- Hasan, A. and Kabir, C. (2002), *Fluid Flow and Heat Transfer in Wellbores*, Society of Petroleum Engineers.
- Hasan, A., Kabir, C. and Wang, X. (2009), 'A Robust Steady-State Model for Flowing-Fluid Temperature in Complex Wells', *SPE Production & Operations* (May), pp. 269–276.
- Heaton, J. (2008), *Introduction to Neural Networks for Java*, 2nd Edition, Heaton Research.
- Holland, J. (1992), 'Genetic Algorithms', *Scientific American* (July), pp. 66–72.
- Horn, M., Plathey, D. and Ibrahim, O. (1998), 'Multilateral Horizontal Well Increases Liquids Recovery in the Gulf of Thailand', *SPE Drilling & Completion* (June), pp. 78–87.
- Ijioma, A. and Jackson, M. (2014), 'Closed-Loop Feedback Control of Smart Wells for Production Optimization Using Downhole Measurements of Self-Potential', paper SPE 170768 presented at the Annual Technical Conference and Exhibition, Amsterdam, The Netherlands, 27-29 October.

- In't Panhuis, P., den Boer, H., van der Horst, J., Paleja, R., Randell, D., Joinson, D., McIvor, P., Green, K. and Bartlett, R. (2014), 'Flow Monitoring and Production Profiling Using DAS', paper SPE 170917 presented at the SPE Annual Technical Conference and Exhibition, Amsterdam, The Netherlands, 27-29 October.
- Isebor, O. (2009), *Constrained Production Optimization with an Emphasis on Derivative-Free Methods*, Master's thesis, Department of Energy Resources Engineering, Stanford University, Stanford, California.
- Johannessen, K., Drakeley, B. and Farhadiroushan, M. (2012), 'Distributed Acoustic Sensing - A New Way of Listening to Your Well/Reservoir', paper SPE 149602 presented at the Intelligent Energy International Conference and Exhibition, Utrecht, The Netherlands, 27-29 March, Utrecht.
- Johansen, E., Ünalmsis, Ö. and Lievois, J. (2011), 'Wet-Gas Flowmeter', Patent number US 7,938,023 B2.
- Kabir, C., Hasan, A., Jordan, D. and Wang, X. (1996), 'A Wellbore/Reservoir Simulator for Testing Gas Wells in High-Temperature Reservoirs', *SPE Formation Evaluation*, **Vol. 11**(June), pp. 128–134.
- Kashikar, S. (2012), 'Quantitative Wellbore and Reservoir Characterization Using Distributed Acoustic Sensing', Proceedings of Distributed Fiber-Optic Monitoring for Well, Reservoir, and Field Management Workshop, Palos Verdes, California, 1-3 August.
- Kitanidis, P. (2012), *Course Notes on Stochastic Inverse Modeling and Data Assimilation Methods*, Department of Civil and Environmental Engineering, Stanford University.
- Koelman, J., Lopez, J. and Potters, H. (2011), 'Fiber Optic Technology for Reservoir Surveillance', paper IPTC 14629 presented at the International Petroleum Technology Conference, Bangkok, Thailand, 7-9 February.

Lemmon, E., McLinden, M. and Friend, D. (2016), 'Thermodynamics Research Center Database', National Institute of Standards and Technology, (retrieved February 2nd, 2016).

URL: <http://webbook.nist.gov/chemistry/fluid/>

Levy, M., Bass, H. and Stern, R. (2001), *Modern Acoustical Techniques for the Measurement of Mechanical Properties*, 1st Edition, Academic Press.

Li, Z. (2010), *Interpreting Horizontal Well Flow Profiles and Optimizing Well Performance by Downhole Temperature and Pressure Data*, PhD dissertation, Petroleum Engineering Department, Texas A&M University, College Station, Texas.

Li, Z. and Zhu, D. (2010), 'Optimization of Production with ICV by Using Temperature Data Feedback in Horizontal Wells', paper SPE 135156 presented at the Annual Technical Conference and Exhibition, Florence, Italy, 19-22 September.

Liu, Y. (2013), *Interpreting Pressure and Flow Rate Data from Permanent Downhole Gauges Using Data Mining Approaches*, PhD dissertation, Department of Energy Resources Engineering, Stanford University, Stanford, California.

Lomeland, F., Ebeltoft, E. and Thomas, W. (2005), 'A New Versatile Relative Permeability Correlation', paper SCA 2005-32 presented at the International Symposium of the Society of Core Analysts, Toronto, Canada, 21-25 August.

MacPhail, W., Lisoway, B. and Banks, K. (2012), 'Fiber Optic Distributed Acoustic Sensing of Multiple Fractures in a Horizontal Well', paper SPE 152422 presented at the Hydraulic Fracturing Technology Conference, The Woodlands, Texas, 6-8 February.

Martinez, R., Hill, A. and Zhu, D. (2014), 'Diagnosis of Fracture Flow Conditions with Acoustic Sensing', paper SPE 168601 presented at the Hydraulic Fracturing Technology Conference, The Woodlands, Texas, 4-6 February.

Mateeva, A., Mestayer, J., Cox, B., Kiyashchenko, D., Wills, P., Lopez, J., Grandi, S., Hornman, K., Lumens, P., Franzen, A., Hill, D. and Roy, J. (2012), 'Advances

- in Distributed Acoustic Sensing (DAS) for VSP', Proceedings of the Society of Exploration Geophysicists Annual Meeting, Las Vegas, Nevada, 4-9 November, pp. 1-5.
- MathWorks (2013), *MATLAB Software*, R2013b.
- Mavko, G. and Mukerji, T. (1998), 'Bounds of Low-Frequency Seismic Velocities in Partially Saturated Rocks', *Geophysics*, **Vol. 63**(May-June), pp. 918-924.
- Mckinley, R., Bower, F. and Rumble, R. (1972), 'The Structure and Interpretation of Noise From Behind Cemented Casing', paper SPE 3999 presented at the AIME Annual Fall Meeting, San Antonio, Texas, 8-11 October.
- Mestayer, J., Cox, B., Wills, P., Kiyashchenko, D., Lopez, J., Costello, M., Bourne, S., Ugueto, G., Lupton, R., Solano, G., Hill, D. and Lewis, A. (2011), 'Field Trials of Distributed Acoustic Sensing for Geophysical Monitoring', Proceedings of the Society of Exploration Geophysicists Annual Meeting, San Antonio, Texas, 18-23 September, pp. 4253-4257.
- Mitchell, M. (1996), *An Introduction to Genetic Algorithms*, The MIT Press, Cambridge.
- Mohaghegh, S. (2000), 'Virtual-Intelligence Applications in Petroleum Engineering: Part 1- Artificial Neural Networks', *SPE Distinguished Author Series* (September), pp. 64-72.
- Molenaar, M., Fidan, E. and Hill, D. (2012), 'Real-Time Downhole Monitoring of Hydraulic Fracturing Treatments Using Fibre Optic Distributed Temperature and Acoustic Sensing', paper SPE 152981 presented at the European Unconventional Resources Conference and Exhibition, Vienna, Austria, 20-22 March.
- Molenaar, M., Hill, D., Webster, P., Fidan, E. and Birch, B. (2011), 'First Downhole Application of Distributed Acoustic Sensing (DAS) for Hydraulic Fracturing Monitoring and Diagnostics', paper SPE 140561 presented at the Hydraulic Fracturing Technology Conference and Exhibition, The Woodlands, Texas, 24-26 January.

- Mubarak, S., Dawood, N. and Salamy, S. (2009), ‘Lessons Learned from 100 Intelligent Wells Equipped with Multiple Downhole Valves’, paper SPE 126089 presented at the Saudi Arabia Section Technical Symposium and Exhibition, Al-Khobar, Saudi Arabia, 9-11 May.
- Muradov, K. and Davies, D. (2012), ‘Application of Distributed Temperature Measurements to Estimate Zonal Flow Rate and Pressure’, paper IPTC 15215 presented at the International Petroleum Technology Conference, Bangkok, Thailand, 7-9 February.
- Nizkous, I., Gerritsen, S., Kiyashchenko, D. and Joinson, D. (2015), ‘Distributed Acoustic Sensing (DAS) VSP for Imaging and Velocity Model Building’, paper IPTC 18483 presented at the International Petroleum Technology Conference, Doha, Qatar, 6-9 December.
- Onwunali, J. (2006), *Optimization of Nonconventional Well Placement Using Genetic Algorithms and Statistical Proxy*, Master’s thesis, Department of Petroleum Engineering, Stanford University, Stanford, California.
- Osgood, B. (2007), *Course Notes on The Fourier Transform*, Department of Electrical Engineering, Stanford University, Stanford, California.
- Ouyang, L. and Belanger, D. (2006), ‘Flow Profiling by Distributed Temperature Sensor (DTS) System - Expectation and Reality’, *SPE Production & Operations* (May), pp. 269–281.
- Paleja, R., Mustafina, D., In’t Panhuis, P., Park, T., Randell, D., van der Horst, J. and Crickmore, R. (2015), ‘Velocity Tracking for Flow Monitoring and Production Profiling Using Distributed Acoustic Sensing’, paper SPE 174823 presented at the Annual Technical Conference and Exhibition, Houston, Texas, 28-30 September.
- Pan, Y. and Horne, R. (1998), ‘Improved Methods for Multivariate Optimization of Field Development Scheduling and Well Placement Design’, *Journal of Petroleum Technology* (December).

- Paulsson, B., Toko, J., Thornburg, J., Slopko, F. and He, R. (2014), 'Development and Test of a 300C Fiber Optic Borehole Seismic System', Proceedings of the 39th Workshop on Geothermal Reservoir Engineering, Stanford, California, 24-26 February.
- Perry, R. and Green, D. (1984), *Perry's Chemical Engineers' Handbook*, 6th Edition, McGraw Hill.
- Pinzon, I., Davies, J., Mammadkhan, F. and Brown, G. (2007), 'Monitoring Production From Gravel-Packed Sand-Screen Completions on BP's Azeri Field Wells Using Permanently Installed Distributed Temperature Sensors', paper SPE 110064 presented at the Annual Technical Conference and Exhibition, Anaheim, California, 11-14 November.
- Poletto, F., Finfer, D., Corubolo, P. and Farina, B. (2014), 'Dual Seismic Fields From Distributed Acoustic Sensors', Proceedings of the Society of Exploration Geophysicists Annual Meeting, Denver, Colorado, 26-31 October, pp. 1899–1903.
- Radcliffe, N. (1991), 'Formal Analysis and Random Respectful Recombination', Proceedings of the 4th International Conference on Genetic Algorithms, San Mateo, California, pp. 222–229.
- Rahman, M. (2011), *Applications of Fourier Transforms to Generalized Functions*, WIT Press, Halifax, Canada.
- Raman, C. (1928), 'A New Radiation', *Indian Journal of Physics*, **Vol. 2**, pp. 387–398.
- Ramey, H. (1962), 'Wellbore Heat Transmission', *Journal of Petroleum Technology* (April), pp. 427–435.
- Rigot, V. (2003), *New Well Optimization in Mature Fields*, Master's thesis, Department of Energy Resources Engineering, Stanford University, Stanford, California.
- Rosen, J. and Gothard, L. (2010), *Encyclopedia of Physical Science*, 1st Edition, Facts On File Inc.

- Roy, B. (2002), *Fundamentals of Classical and Statistical Thermodynamics*, John Wiley & Sons.
- Saleri, N., Salamy, S., Mubarak, H., Sadler, R., Dossary, A. and Muraikhi, A. (2003), 'SHAYBAH-220 : A Maximum Reservoir Contact (MRC) Well and Its Implications for Developing Tight Facies Reservoirs', paper SPE 81487 presented at the Middle East Oil Show and Conference, Manama, Bahrain, 5-8 April.
- Shi, H., Holmes, J., Diaz, L., Durlofsky, L. and Aziz, K. (2005), 'Drift-Flux Parameters for Three-Phase Steady-State Flow in Wellbores', *SPE Journal* (June), pp. 130–137.
- Shi, H., Holmes, J., Durlofsky, L., Aziz, K., Diaz, L., Alkaya, B. and Oddie, G. (2005), 'Drift-Flux Modeling of Two-Phase Flow in Wellbores', *SPE Journal* (March), pp. 24–33.
- Shirangi, M. and Durlofsky, L. (2015), 'Closed-Loop Field Development Under Uncertainty by Use of Optimization With Sample Validation', *SPE Journal* (October), pp. 908–922.
- Shu, J. (2005), *Comparison of various techniques for computing well index*, Master's thesis, Department of Petroleum Engineering, Stanford University, Stanford, California.
- Siebenaler, S., Krishnan, V., Lumens, P., Gesoff, G. and Salmatanis, N. (2015), 'Evaluation of Distributed Acoustic Sensing Leak Detection Technology for Offshore Pipelines', Proceedings of the 25th International Ocean and Polar Engineering Conference, Kona, Hawaii, 21-26 June, pp. 374–381.
- Silva, M., Muradov, K. and Davies, D. (2012), 'Review, Analysis and Comparison of Intelligent Well Monitoring Systems', paper SPE 150195 presented at the Intelligent Energy International Conference and Exhibition, Utrecht, The Netherlands, 27-29 March.

- Strebelle, S. (2002), ‘Conditional Simulation of Complex Geological Structures Using Multiple-Point Statistics’, *Mathematical Geology*, **Vol. 34**(1), pp. 1–21.
- Su, H. and Oliver, D. (2010), ‘Smart-Well Production Optimization Using an Ensemble-Based Method’, *SPE Reservoir Evaluation & Engineering* (December), pp. 884–892.
- Sui, W., Zhu, D., Hill, A. and Ehlig-Economides, C. (2008), ‘Determining Multilayer Formation Properties From Transient Temperature and Pressure Measurements’, paper SPE 116270 presented at the Annual Technical Conference and Exhibition, Denver, Colorado, 21-24 September.
- Tabatabaei, M., Tan, X., Hill, A. and Zhu, D. (2011), ‘Well Performance Diagnosis with Temperature Profile Measurements’, paper SPE 147448 presented at the Annual Technical Conference and Exhibition, 30 October-2 November, Denver, Colorado.
- Taylor, R. and Russell, R. (1997), ‘Drilling and Completing Multilateral Horizontal Wells in the Middle East’, paper SPE 38759 presented at the Annual Technical Conference and Exhibition, San Antonio, Texas, 5-8 October.
- Temizel, C., Purwar, S., Urrutia, K. and Abdullayev, A. (2015), ‘Real-Time Optimization of Waterflood Performance Through Coupling Key Performance Indicators in Intelligent Fields’, paper SPE 173402 presented at the Digital Energy Conference and Exhibition, The Woodlands, Texas, 3-5 March.
- Temizel, C., Purwar, S., Urrutia, K., Abdullayev, A., Adnan, F., Agarwal, A., Garcia, A. and Gorucu, S. (2014), ‘Optimization of Well Placement in Real-Time Production Optimization of Intelligent Fields with Use of Local and Global Methods’, paper SPE 170675 presented at the Annual Technical Conference and Exhibition, Amsterdam, The Netherlands, 27-29 October.
- Thodi, P., Paulin, M., Forster, L., Burke, J. and Lanan, G. (2014), ‘Arctic Pipeline Leak Detection using Fiber Optic Cable Distributed Sensing Systems’, paper OTC

- 24589 presented at the Arctic Technology Conference, Houston, Texas, 10-12 February.
- Turner, R. (2012), 'Smart Wells - A Key Enabler for Oilfield Developments in Brunei', paper IPTC 15329 presented at the International Petroleum Technology Conference, Bangkok, Thailand, 7-9 February.
- Ugueto, G., Ehiwario, M., Grae, A., Molenaar, M., McCoy, K., Huckabee, P. and Barree, B. (2014), 'Application of Integrated Advanced Diagnostics and Modeling to Improve Hydraulic Fracture Stimulation Analysis and Optimization', paper SPE 168603 presented at the Hydraulic Fracturing Technology Conference, The Woodlands, Texas, 4-6 February.
- Ünalmsis, Ö., Johansen, E. and Perry, L. (2010), 'Evolution in Optical Downhole Multiphase Flow Measurement: Experience Translates into Enhanced Design', paper SPE 126741 presented at the Intelligent Energy International Conference and Exhibition, Utrecht, The Netherlands, 23-25 March.
- Ünalmsis, Ö. and Trehan, S. (2012), 'In-Well, Optical, Strain-Based Flow Measurement Technology and Its Applications', paper SPE 154422 presented at the EAGE Annual Conference & Exhibition, Copenhagen, Denmark, 4-7 June.
- Ünalmsis, Ö. and Trehan, S. (2013), 'Downhole Multiphase Flow Measurement in Horizontal Wellbores', paper SPE 164854 presented at the EAGE Annual Conference & Exhibition, London, The United Kingdom, 10-13 June.
- Viola, P. and Jones, M. (2001), 'Robust Real-time Object Detection', *International Journal of Computer Vision* (February), pp. 5-22.
- Vo, H. and Durlofsky, L. (2016), 'Regularized Kernel PCA for the Efficient Parameterization of Complex Geological Models', *Journal of Computational Physics*, **Vol. 322**, pp. 859-881.
- Wang, X., Lee, J., Thigpen, B., Vachon, G., Poland, S. and Norton, D. (2008), 'Modeling Flow Profile Using Distributed Temperature Sensor (DTS) System', paper

- SPE 111790 presented at the Intelligent Energy Conference and Exhibition, Amsterdam, The Netherlands, 25-27 February.
- Wang, Z. (2012), *The Uses of Distributed Temperature Survey (DTS) Data*, PhD dissertation, Department of Energy Resources Engineering, Stanford University, Stanford, California.
- Webster, P., Wall, J., Perkins, C. and Molenaar, M. (2013), 'Micro-Seismic Detection Using Distributed Acoustic Sensing', Proceedings of the Society of Exploration Geophysicists Annual Meeting, Houston, Texas, 22-27 September, pp. 2459–2463.
- Weinstein, E., Steele, K., Agarwal, A. and Glass, J. (2016), 'Large Acoustic Data Array Project', The MIT Computer Science and Artificial Intelligence Laboratory (CSAIL), (retrieved February 5th, 2016).
URL: <http://groups.csail.mit.edu/cag/mic-array/>
- Wilson, K. and Durlinsky, L. (2013), 'Optimization of Shale Gas Field Development Using Direct Search Techniques and Reduced-Physics Models', *Journal of Petroleum Science and Engineering*, **Vol. 108**, pp. 304–315.
- Wood, A. (1941), *A Textbook of Sound*, The Macmillan Company, New York.
- Xiao, J. (2013), 'Personal e-mail communication. EXPEC Advanced Research Center, Saudi Aramco', Personal e-mail communication. EXPEC Advanced Research Center, Saudi Aramco.
- Xiao, J., Farhadiroushan, M., Clarke, A., Abdalmohsen, R., Alyan, E., Parker, T., Shawash, J. and Milne, H. (2014), 'Intelligent Distributed Acoustic Sensing for In-well Monitoring', paper SPE 172197 presented at the Saudi Arabia Section Annual Technical Symposium and Exhibition, Al-Khobar, Saudi Arabia, 21-24 April.
- Xiao, J., Farhadiroushan, M., Clarke, A., Jacob, S., AlMulhem, A., Milne, H., Shawash, J. and Parker, T. (2015), 'Dynamic Water Injection Profiling in Intelligent Wells Using Distributed Acoustic Sensor with Multimode Optical Fibers',

- paper SPE 174865 presented at the Annual Technical Conference and Exhibition, Houston, Texas, 28-30 September.
- Yeten, B. (2003), *Optimum Deployment of Nonconventional Wells*, PhD dissertation, Department of Petroleum Engineering, Stanford University, Stanford, California.
- Yoshioka, K. (2007), *Detection of Water or Gas Entry into Horizontal Wells by Using Permanent Downhole Monitoring Systems*, PhD dissertation, Petroleum Engineering Department, Texas A&M University, College Station, Texas.
- Zhan, G., Kommedal, J. and Nahm, J. (2015), 'VSP Field Trials of Distributed Acoustic Sensing in Trinidad and Gulf of Mexico', Proceedings of the Society of Exploration Geophysicists Annual Meeting, New Orleans, Louisiana, 18-23 October, pp. 5539–5543.